TU Clausthal

Realisation of the Unit Watt in Airborne Sound

Doctoral Thesis

to be awarded the degree
Doctor of Engineering (Dr.-Ing.)

submitted by
Katharina Völkel
from Königs Wusterhausen

approved by the
Faculty of Mathematics/Computer Science
and Mechanical Engineering,
Clausthal University of Technology

Date of oral examination
29 July 2020

Dean and Chairperson of the Board of Examiners
Prof. Dr.-Ing. Volker Wesling

Supervising tutor
Prof. Dr.-Ing. Stefanie Retka

Reviewer
Prof. Dr.-Ing. Sabine C. Langer
Prof. Dr.-Ing. Gunther Brenner

DOI 10.21268/20201124-1

To perseverance . . .
and to you, mom and dad, for everything you are and do for me

Acknowledgements

It's been a long time coming! But here we are now, finally, and I would like to extend my sincere gratitude to a few of the people, who have helped me see this work through. First of all, Professor Stefanie Retka, who never revoked her pledge to be the first examiner of my thesis and supported its completion every step of the way.

Secondly, I would like to thank all the members of the Applied Acoustics working group at PTB Braunschweig for their input to this project, the on and off topic discussions as well as the amicable work atmosphere. To name just two, I would like to thank Professor Werner Scholl and Dr. Volker Wittstock for giving me the chance to embark on this journey, for supervising and guiding large parts of this work and for providing genuine words of wisdom when the ship veered off track. The passion for all things related to acoustics that Prof. Scholl and Dr. Wittstock radiate is truly inspirational!

I would also like to thank Professor Renzo Arina for supervising my three month visit to the Politecnico di Torino. Dr. Claudio Guglielmone of INRIM has to be mentioned in regards to this scholarship and rewarding experience, as well. Just as much, the further colleagues of the partner institutes that participated in the EMRP sound power project cannot go without a thank you. They challenged new thoughts and ideas and opened the doors to their institutes for a visit.

Furthermore, I wish to thank Professor Sabine Langer for giving me the chance and providing the professional framework to finish my thesis. Without this, I am sure that my research would have ended without a deserving finish. And that would have been a real shame! By the same token, I am grateful for the support of my colleagues at the Institute of Acoustics at TU Braunschweig. The story of this thesis would not be complete without the lessons learned from and with them.

On the personal side of things I cannot emphasize my family's role strongly enough - the purry one's just as much as the not so purry one's. In not so unimportant particularity, my partner in crime, Bart, has added a level of happiness and comfort to my life that is hard to express even on a dB scale. The strength and calamity I gain from our relationship has helped

me sail the rougher waters of the thesis completion process. A stupid joke here and there surely helped as well.

I cannot go without praising my parents, though! I still do not quite understand how they managed to keep the lack-of-progress nagging at a perceived 10% and be incredibly supportive for the remaining 90%. Through the thesis process and beyond they have taught me to dream big, love fully, be strong, fierce and independent. This work is dedicated to them and the examples they set for me and my brothers.

Wolfenbüttel, November 2020 Katharina Völkel

Contents

List of Symbols

Latin Symbols - Upper Case

Symbol	Description	Unit of Measure
A	Equivalent absorption area of a room	m^2
B	Bending stiffness	$\mathrm{N\,mm}^2$
$B_0 l$	Transformer constant of the electrodynamic shaker with B_0 denoting a conversion factor and l the wire length of the moving coil	$\mathrm{N\,A}^{-1}$
C	Difference in sound velocity levels between piston and baffle	dB
D	Directivity measure	dB
E	Eigenmode number (equivalent to n)	[1]
F_{sh}	Force at shaker exit	N
G	Discrete representation of PDF G_Y	dB
G_Y	Approximation of PDF g_Y based on knowledge gained from Monte Carlo simulations	dB
H_1	Struve function of the first kind and order	[1]
I	Sound intensity	$\mathrm{W\,m}^{-2}$
J_1	Bessel function of the first kind and order	[1]
J_γ	Bessel function of the first kind and order γ	[1]
K	Subscripted correction term for sound power determination	dB
C_x	Finite number that represents the limit of Eq. 5.2.40	dB
L_Δ	Sound power level difference (equivalent to ΔL_{W})	dB

Symbol	Description	Unit of Measure
L_{el}	Electrical inductance	H
L_I	Sound intensity level	dB
L_p	Sound pressure level	dB
L_S	Level description of the enveloping surface	dB
L_v	Sound velocity level (re. 1 m/s unless denoted otherwise)	dB
L_{W}	Sound power level (re. 1 pW unless denoted otherwise)	dB
M	Total number of measurement points; number of Monte Carlo simulation runs	[1]
M_{of}	Modal overlap factor	[1]
M_{p}	Number of measurement points on the piston surface	[1]
N	Number of points used for the discretised Rayleigh integral	[1]
N_x	Number of points per radius (equivalent to n_r)	[1]
P	Sound power	W
R	Radius of hemispherical surface used for sound pressure and intensity measurements	m
R^2	Coefficient of determination	[1]
R_{el}	Resistance in electric circuit	Ω
R_{i}	Inner resistance of the electrical circuit inside the power amplifier	Ω
$\underline{R}$	Mechanical resistance of the piston (complex valued)	$\mathrm{g\,s^{-1}}$
S	Surface area	$\mathrm{m^2}$
T	Oscillation period	s
T_{rev}	Reverberation time	s
U_0	Input voltage into the power amplifier	V

Symbol	Description	Unit of Measure
U	Expanded uncertainty	dB
V	Room volume	m^3
V_p	Volume of air behind the piston	m^3
X	Difference in sound velocities between piston and baffle; number of points remaining after signal to noise filtration	$\mathrm{m\,s}^{-1}$; [1]
Z	Impedance	Ω
Z_p	Mechanical impedance of the piston	$\mathrm{g\,s}^{-1}$

Latin Symbols - Lower Case

Symbol	Description	Unit of Measure
$a_{\max}$	Maximum accelereation of the piston	$\mathrm{m\,s^{-2}}$
c	Speed of sound in air	$\mathrm{m\,s^{-1}}$
d	Distance	m
d_{ij}	Linear distance between the i-th and j-th measurement point	m
d_{P}	Thickness of piston - complete height	m
d_{S}	Distance of single probe from the source	m
f	Frequency	Hz
f_M	Cut-off frequency for given modal overlap factor	Hz
f_{S}	Schroeder cut-off frequency	Hz
g_Y	True PDF for output quantity Y (here: sound power levels)	dB
h_{sh}	Frictional admittance of the shaker's moving coil	$\mathrm{s\,kg^{-1}}$
i	Electric current; imaginary unit; counter	A; [1]; [1]
k	Wave number; factor to calculate expanded uncertainties, U	$\mathrm{m^{-1}}$; [1]
$l_{\max}$	Largest side length of the primary source	m
m	Mass	kg
m_{P}	Mass of piston	kg
m_{sh}	Mass of the shaker's moving coil	kg
n	Eigenmode number (equivalent to E)	[1]
n_{air}	Compliance of the air volume between shaker and piston	$\mathrm{m\,N^{-1}}$
n_r	Number of points per radius (equivalent to N_x)	[1]

Symbol	Description	Unit of Measure
n_{sh}	Mechanical compliance of shaker's moving coil	$\mathrm{m\,N^{-1}}$
p	Sound pressure; coverage probability	Pa; [1]
$\hat{q}$	Amplitude of the sound energy flux	$\mathrm{m^3\,s^{-1}}$
r	Radius of piston	m
r_{Wedges}	Reflection coefficient of wedges in hemi-anechoic room	[1]
t	Time	s
u_{E}	Input voltage at the shaker entrance	V
u_{sh}	Input voltage into the transformer unit of the shaker	V
$\mathrm{u}(y)$	Standard deviation of mean y in PDF g_Y	dB
$\mathrm{u}(\tilde{y})$	Standard deviation of mean $\tilde{y}$ in PDF G_Y	dB
v	Sound velocity	$\mathrm{m\,s^{-1}}$
v_{max}	Maximum movement velocity of the piston	$\mathrm{m\,s^{-1}}$
v_{sh}	Movement velocity of the shaker's moving coil	$\mathrm{m\,s^{-1}}$
$\hat{w}_E$	Amplitude constant of Eigenmode oscillation	[1]
x	Ratio of total number of measurement points, M, to number of points on the piston surface, M_{p}	[1]
x_{max}	Maximum displacement of the piston	m
x_r	Variable describing the radial distance from the piston centre ($x_r \leq r$)	m
y	Mean of PDF g_Y	dB
$\tilde{y}$	Mean of PDF G_Y	dB

Greek Symbols - Upper Case

Symbol	Description	Unit of Measure
ΔR	Distance between two measurement points	m
Δ	Linear difference	[1]
ΔL_v	Difference of sound velocity levels	dB
ΔL_{W}	Sound power level difference (equivalent to L_{Δ})	dB
Γ	Directivity factor	[1]
Ω_0	Factor describing volume into which sound is emitted - valued at 2π for hemispheres and 4π for full spheres	rad

Greek Symbols - Lower Case

Symbol	Description	Unit of Measure
α	Angle with respect to $x-y$ plane	rad
α_{abs}	Absorption coefficient	[1]
β	Polar angle in the x-y plane	rad
θ	Phase shift between sound pressure and velocity	rad
θ_{sai}	Angle between real and imaginary part of the specific acoustic impedance	rad
κ_E	Solution to Eq. A.0.1, corresponding to Eigenmodes	[1]
λ	Wavelength	m
ν	Poisson's ratio	[1]
ρ	Density	$\mathrm{kg\,m^{-3}}$
ρ_0	Density of air	$\mathrm{kg\,m^{-3}}$
ϕ	Phase angle	rad
ω	Angular frequency	Hz

Subscripts

a Airborne sound, analytical calculation
baffle Regards parts of the baffle surface only
bending Non-uniform motion of piston surface
eff Root mean square value
K Structure-borne sound
max Maximum value
min Minimum value
n Normal component
P Piston
piston Regards piston surface only
Rayl. Discretised Rayleigh integral
rigid Uniform motion of piston surface
sai Specific acoustic impedance
simpl. Simplified
total Result after considering both piston and baffle

Abbreviations

BAuA Bundesanstalt für Arbeitsschutz und Arbeitsmedizin
EMRP European Metrology Research Programme
GUM Guide to the expression of uncertainty in measurement
INRIM Instituto Nazionale di Ricerca Metrologica
LNE Laboratoire National de Métrologie et d'Essais
PDF Probability density function
PTB Physikalisch Technische Bundesanstalt (Braunschweig)
RMS Root mean square
SP Sveriges Tekniska Forskningsinstitut
SNR Signal to noise ratio
Tübitak The Scientific and Technological Research Council of Turkey

Abstract

The central quantity in regulations concerning acoustics is the sound power emitted by a sound source. Building up from the current state of the art of sound power determination, this work will show that there is potential to build a metrological traceability chain for this measurand. Firstly, the lack thereof will be discussed and the problems that arise from this situation will be detailed (Chp. 2). This will argue the need for a proper traceability chain including a primary, secondary and transfer standards.

This work will focus on the level of the primary standard, which provides a foundation to the desired traceability chain. The task requires a significant shift in measurement protocol used. All currently standardised procedures require measurements in the sound field - while also sampling the sound field quantities sound pressure or intensity. The newly introduced procedure places the measurement equipment outside of the sound field and measures the motion of the primary standard's surface directly. The measurement protocols and environments as well as the used physical realisations of primary sources will be described (Chp. 3). Certainly, other types or designs of primary standards are possible. The structural as well as material choices for the realisations described in this work are based on analytical and numerical studies on the characteristics of the chosen circular piston design. They will be described in detail (Chp. 4).

Besides radiation characteristics, the design choices for the primary standards used are obviously governed by the suitability to the measurement method. This methodology builds on the Rayleigh integral in its discretised form. By measuring surface velocities as well as phase relations at pre-defined points of the measurement surface, the emitted sound power is calculated. The boundary condition that is imposed by this choice of measurement method is that of the need of a planar radiator which has to be embedded into the floor of the measurement environments. The discretised Rayleigh integral method is a validated methods so that the main question of interest for this work is whether its convergence can be guaranteed and, if so, how many sampling points are required to approximate this convergent value with a pre-set level of uncertainty. Both of these aspects will be discussed (Chp. 5).

With the theoretical framework in place, measurement data will be evaluated. As expected, these introduce a new aspects into the uncertainty calculations: noise. The evaluation of the uncertainties associated with calculated sound power levels is a central topic determining the usability of the described primary standards. Based on Monte Carlo simulations, strategies to determine uncertainties will be developed. They focus on the aspects of filtration of noisy data and usability of measurement surfaces - piston versus baffle. It will be shown that in terms of precision, the proposed discretised Rayleigh integral method has the potential to yield satisfactory results (Chp. 6).

In terms of accuracy, however, shortcomings of the tested primary standards will be reported. Differences in sound power levels between the ones obtained from the discretised Rayleigh integral and those gathered using standardised methods will be shown and explanations attempted (Chp. 7). The results open the window for further studies particularly on the design of primary standards. However, the suitability and validity of the proposed measurement method to form the basis of a traceability chain for the measurand sound power in air will result from this work.

Zusammenfassung

Die zentrale Größe akustischer Normgebung ist die von einer Quelle abgestrahlte Schallleistung. Ausgehend vom derzeitigen Stand der Wissenschaft in der Schallleistungsmessung wird diese Arbeit aufzeigen, dass die Erstellung einer metrologisch gültigen Kalibrierkette für diese Größe realistisch ist. Dazu wird zunächst deren Fehlen diskutiert, woraus der Bedarf an einer gültigen Kalibrierkette mit Primär- und Sekundärnormalen sowie Transferstandards ersichtlich wird (Kap. 2).

Diese Arbeit befasst sich mit der Kalibrierstufe des Primärnormals, welches das Fundament einer zu bestimmenden Kalibrierkette bildet und schlägt eine signifikante Veränderung der Messprotokollarien vor. Alle derzeit genormten Verfahren erfordern Messungen im Schallfeld - bei gleichzeitiger Messung der Schallfeldgrößen Druck oder Intensität. Das in dieser Arbeit vorgestellte Verfahren positioniert die Messgeräte außerhalb des Schallfelds und misst die Oberflächenschwingung der Primärquelle direkt. Das Messprotokoll, Räumlichkeiten sowie verwendete physische Realisierungen der Primärquellen werden vorgestellt (Kap. 3).

Grundsätzlich bestehen auch andere Möglichkeiten, Primärquellen zu konzeptionieren. Numerische und analytische Berechnungen zu den erwartbaren Eigenschaften von kreisförmigen Kolbenstrahlern verschiedener Dimensionen führten zur Wahl der hier vorgestellten Primärquellen. Diese Berechnungen werden detailliert beschrieben (Kap. 4).

Des Weiteren ist die Eignung der Quellen in Bezug auf die Messmethode von entscheidender Bedeutung. Diese basiert auf dem Rayleigh Integral in diskretisierter Form. Durch die Messung von Oberflächenschnellen und dazugehöriger Phasenlagen an definierten Messpunkten werden hierüber Schallleistungen errechnet. Die Gültigkeit der Methode basiert auf der Annahme ebener Strahler, für welche die Anwendung des diskretisierten Rayleigh Integrals validiert ist. Damit ist die entscheidende Frage für diese Arbeit, ob eine Konvergenz garantiert werden kann. In einem solchen Falle ist die Frage der notwendigen Anzahl an Messpunkten von Interesse. Beide Aspekte werden in dieser Arbeit diskutiert (Kap. 5).

Aufbauend auf diesen Grundlagen werden im weiteren Verlauf der Arbeit

Messdaten analysiert. Diese erweitern vorangegangene Diskussionen zur Unsicherheit um den Aspekt des Rauschens. Die Bewertung der Unsicherheiten berechneter Schallleistungen ist ein zentrales Thema, welches die Nutzbarkeit der beschriebenen Primärquellen maßgeblich beeinflusst. Basierend auf Monte-Carlo Simulationen werden Strategien zur Unsicherheitsquantifizierung erarbeitet, die sich insbesondere auf die Aspekte der Datenbereinigung verrauschter Messergebnisse sowie die Nutzbarkeit unterschiedlicher Messoberflächen - Kolben und Bodenplatte - konzentrieren. Es wird gezeigt, dass das diskretisierte Rayleigh Integral in Betrachtung seiner Genauigkeit zufriedenstellende Ergebnisse liefert (Kap. 6).

In Hinblick auf die Exaktheit der Ergebnisse werden allerdings Schwachstellen der genutzten Primärquellen sichtbar. Unterschiede zwischen den Schallleistungen aus mittels diskretisiertem Rayleigh Integral und genormten Methoden erhaltenen Werte werden gezeigt und Erklärungsversuche angestrengt (Kap. 7). Die Ergebnisse beschreiben mögliche Richtungen zukünftiger Forschung insbesondere für das Thema des Designs von Primärquellen. Gleichwohl wird die grundsätzliche Eignung und Gültigkeit der vorgestellten Messmethode als Basis einer Kalibrierkette für die Größe Schallleistung in Luft als Ergebnis dieser Arbeit herausgestellt.

1 | Introduction and Aim of Work

The total amount of sound energy emitted by a source describes the sound power of said source. Thus, sound power determination is a major component in the assessment of the radiation strength of a sound source. In contrast to sound pressure or intensity, sound power is independent of the distance to the source and usually considered to be independent of the acoustic environment as well [41]. However, a metrological traceability chain for sound power is non-existent at the moment. Though various standardised methods of sound power determination exist, these do not rely on a primary standard and the denoted uncertainties are best estimates (e.g. [21][22][23]). This leads to the conundrum that manufacturers are required to label their products with the respective emitted sound power, but that - depending on the standardised method used to determine this sound power - level differences in the range of 2 dB are not unusual [41].

Another problematic aspect of currently standardised sound power determination methods is their lower frequency limit, which is at 100 Hz. Sound sources which emit noise at lower frequencies exist - large wind turbines being the most common example [31]. Generally, the number of noise sources emitting low frequency noise (especially around 50 Hz) is expected to rise in the coming years as a result of a transformation of the energy system especially in Germany [9]. Yet, no standardised measurement method for their sound power output exists.

While some procedures are documented for measurements at as low as 8 Hz, their connection to standardised methods is difficult and the accuracy questionable [14]. Noise pollution has been linked to health risks such as sleep disturbance, stress and cardiovascular disease [45]. As such, correct quantification of low frequency noise is not only necessary for regulatory purposes but also to protect our quality of life.

To combat both the traceability as well as the lower frequency limit problem of current sound power determinations, a joint research project funded by the European Metrology Research Programme (EMRP) was started in 2013. Three different scientific work packages were to be executed within the consortium of institutes from Italy (INRIM, Politecnico di Torino), Sweden (SP), France (LNE), Turkey (Tübitak) and Germany

(PTB, BAuA). These three work packages dealt with the realisation of the unit Watt in airborne sound, its dissemination by transfer standards and the application in machinery noise, respectively.

The author was employed at PTB and her tasks lay in the first work package - the realisation of the unit Watt in airborne sound for the frequency range from 20 Hz to 20 kHz. Consequently, this work will focus on that part. The main topics to be elaborated concern the design of the primary source (Chp. 4), the discretisation needed for accurate sound power determinations (Chp. 5) and a determination of the associated uncertainty by scientifically accepted methods (Chp. 6). The current state of the art of sound power determination is elaborated first in order to clarify the context and need for this work (Chp. 2). To aid understanding, the utilised measurement environments and different primary sources are described in detail (Chp. 3).

Given the integrated nature of this work in the framework of the EMRP project, references to results from the work on the dissemination of the unit will be drawn (Chp. 7). These will be taken from a parallel dissertation, which focused on the second work package of the project [5]. The main results from the entire EMRP project were presented in a structured session at Internoise 2016. The interested reader is hence referred to the literature for more information on the justification for the need of a realisation of the unit Watt in airborne sound ([1][2][42]), an overview over the different primary standards that were developed at all partner institutes ([27]), numerical studies that were performed on them ([3][39]), work on the dissemination of the unit ([4][6][7]), as well as a compact description of the main achievements of the project ([13]).

2 | Current Knowledge

In order to make the distinction between the newly proposed Rayleigh-integral-method and currently standardised methods more clear, an overview over currently accepted measurement protocols will be given in this chapter. The guiding principle will be a description of the physics underlying sound power determination in reference to the engineering reality of measurement approximations. For this, the focus will first be placed on methods involving enveloping surfaces. In a second step also volume methods will be elaborated.

2.1 Determination of Sound Power

Several different methods of sound power determination exist. A guideline to the use of the appropriate method for the measurement set-up and frequency spectrum in use as well as resolution desired is given in ISO 3740 [21]. In the context of this work however, the importance lay less in the specific measurement procedures themselves but rather in the physics underlying them. Here the following measurement set-up was considered: A sound source is run inside a room, where the sound source is placed on or in the floor of the room. The source diameter is small compared to the smallest side length of the room and the source placement in the room is central or approximately central. When run, the sound source emits sound waves into the room and its sound power, P, is to be determined. Classical measurement procedures that are standardised by ISO require measurements within the sound field. This naturally puts a strain on the minimum frequency that is measurable. Considering that at a frequency of 100 Hz, the wavelength of sound in air is approximately 3.4 m, it becomes evident that room size is the main factor in determining a lower frequency limit.

In which manner the sound power of a source is determined in a specific setting depends on the room environment in which the source is run. This can be visualised as follows: When the source is started, sound waves travel only outbound from the source (Fig. 2.1.1a). As soon as the sound waves hit the room walls the absorptive/reflective properties of these room walls determine whether sound waves are reflected or not. Sound power determinations with small uncertainties can only be achieved in

two types of measurement rooms - (hemi-)anechoic or reverberation chambers. Anechoic rooms are characterised by having only non-reflective walls. Hemi-anechoic rooms have a fully reflecting floor surface with all other walls being absorbent. In reverberation chambers all walls are reflective.

Irrespective of the measurement environment, close to the source's surface sound pressure and sound velocity are not in phase. This leads to sound power having a real and imaginary component, which signifies that an active and a reactive component are its constituents. This area is called near field. With increasing distance from the source, the phase shift between velocity and pressure decreases until it is non-existent. At this point the far field begins. In the far field then, a direct relationship between sound pressure, $\tilde{p}$, and sound velocity, $\tilde{v}$ exists (Eq. 2.1.1). Tilde notation indicates root mean square (RMS) values. The exact distance from the source where near field and far field meet, cannot be named [34].

$$\tilde{p} = \rho_0 c \tilde{v} \tag{2.1.1}$$

In ideal (hemi-)anechoic rooms only sound waves that are unidirectional - outbound from the source - exist. Once they hit the room walls, these sound waves are completely absorbed. There are no reflections (Fig. 2.1.1b). The opposite is then true for reverberation rooms. Sound waves that are emitted by the source are completely reflected once they hit the room walls. A reverberation room thus "fills up" with sound waves. In any measurement point then, there are sound waves from all directions in equal strength (Fig. 2.1.1c). Any real room situates itself somewhere between these two extreme cases. The most common methods for sound power determination are the enveloping surface method - measuring either sound pressure or sound intensity - as well as the volume measurement method, focusing on sound pressure [34].

2.1.1 Enveloping surface methods

In general sound power, P, is given as surface integral of the sound intensity, I, that passes through a measurement surface which envelops the source under test (Fig. 2.1.2). In theory measurement surfaces should achieve perpendicularity of the sound velocity, v, to the measurement surface. In real measurements it is not always possible to discern the shape of the sound field from the shape of the sound source. Hence, cuboid,

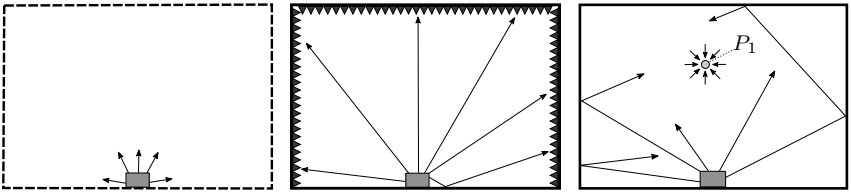

(a) Initial sound wave emission when the sound source is started. The grey rectangle depicts the sound source, arrows the emitted sound waves.

(b) Equilibrium of sound emission in a hemi-free field. The triangles on the room walls depict the material absorbing incoming sound waves.

(c) Equilibrium of sound emission in a reverberation chamber. At point P_1, sound wave immission is omnidirectional of equal strength.

Figure 2.1.1: Schematic of sound emission in ideal rooms.

hemispherical or similar measurement surfaces are usually chosen [34].

Having defined a measurement surface and measuring the sound intensity directly is the first option for sound power determination. This method is called sound intensity method. The sound intensity is given by the temporal average of the product of sound pressure and velocity (Eq. 2.1.2). Usually, the pressure gradient dp/dr is measured instead of the sound velocity, $\vec{v}(t)$, though, as this omits the more complicated phase measurements. From Euler's Equation (Eq. 2.1.3), the sound velocity can be calculated using the pressure gradient (Eq. 2.1.4) [34].

$$\vec{I} = \overline{p(t)\vec{v}(t)} \tag{2.1.2}$$

$$-\frac{\mathrm{d}p}{\mathrm{d}r} = \rho_0 \frac{\mathrm{d}v_\mathrm{n}}{\mathrm{d}t} \tag{2.1.3}$$

$$v_\mathrm{n}(t) = -\frac{1}{\rho_0}\int \frac{\mathrm{d}p}{\mathrm{d}r}\mathrm{d}t \tag{2.1.4}$$

In measurement protocols, the pressure gradient is approximated by performing two pressure measurements, $p_\mathrm{A}(t)$ and $p_\mathrm{B}(t)$, where the distance between the two measurement locations, ΔR, is much smaller than the wavelength of the emitted sound waves in air, λ_a ($\Delta R \ll \lambda_\mathrm{a}$). The microphones can either be facing each other or parallel for these measurements. The normal component of sound velocity is thus approximated (Eq. 2.1.5)

and the normal component of sound intensity calculated (Eq. 2.1.6). Integrating the normal component of the sound intensity over the entire measurement surface yields the sound power output according to the Gaussian integral theorem (Eq. 2.1.7). The sound power can also be expressed as sound power level by conversion to the [dB]-scale (Eq. 2.1.8) [34].

$$v_{\mathrm{n}}(t) \approx -\frac{1}{\rho_0} \int \frac{p_{\mathrm{B}}(t) - p_{\mathrm{A}}(t)}{\Delta R} \mathrm{d}t \tag{2.1.5}$$

$$I_{\mathrm{n}} = \frac{1}{2\rho_0 \Delta R T} \int_0^T \left\{ [p_{\mathrm{A}}(t) + p_{\mathrm{B}}(t)] \int_0^t [p_{\mathrm{B}}(\tau) - p_{\mathrm{A}}(\tau)] \mathrm{d}\tau \right\} \mathrm{d}t \tag{2.1.6}$$

$$P = \int \vec{I} \, \mathrm{d}\vec{S} = \int I_{\mathrm{n}} \, \mathrm{d}S \tag{2.1.7}$$

$$L_{\mathrm{W}} = L_{I,\mathrm{n}} + L_S \tag{2.1.8}$$

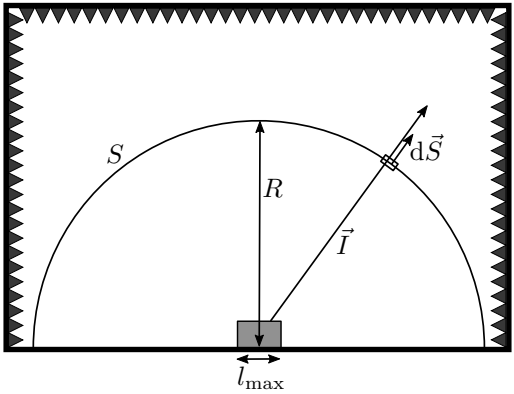

Figure 2.1.2: Sound power determination in a hemi-anechoic room for a small sized source ($l_{\max} < \lambda_{\mathrm{a}}$). $R > 2l_{\max}$ denotes the radius of the measurement area S, λ_{a} the wavelength of the emitted sound waves, $\vec{I}$ the sound intensity vector and $\mathrm{d}\vec{S}$ the normal component of the surface element $\mathrm{d}S$.

In (hemi-)anechoic rooms, where free field conditions apply, it is also possible to determine sound power using the so called free field method. This method relies on the approximation of sound intensity through sound pressure, which is only valid in free fields and in the far field of the source.

In such conditions, the intensity contour integral (Eq. 2.1.9) can be replaced by a contour integral over sound pressure (Eq. 2.1.10) because the far-field condition applies (Eq. 2.1.1).

For measurements, the same surface as before can be utilised and the sound power determined using sound pressure measurements with the largest possible discretisation on the surface. From the measured sound pressure, $\tilde{p}$, or sound pressure level values, L_p, the sound power, P (Eq. 2.1.10), or sound power level, L_W, can be calculated (Eq. 2.1.11). Here $\overline{L_p}$ denotes the temporal and spatial mean sound pressure level, S denotes the measurement surface and S_0 a reference surface of 1 m^2 [34].

$$P = \oint \vec{I} \mathrm{d}\vec{S} \tag{2.1.9}$$

$$P = \oint \frac{\tilde{p}^2}{\rho_0 c} \mathrm{d}S \tag{2.1.10}$$

$$L_\mathrm{W} = \overline{L_p} + 10 \log \frac{S}{S_0} = \overline{L_p} + L_S \quad [\mathrm{dB}] \tag{2.1.11}$$

2.1.1.1 Problems with the Enveloping Surface Method

Firstly, the free field method involving sound pressure measurements is considered. One contributor to uncertainty is the near-field effect. This effect has two parts: the impedance effect and the angle effect. For sinusoidal quantities in the far field of the sound source, the RMS values of sound velocity, $\tilde{v}$, and sound pressure, $\tilde{p}$, can be used to replace the square of the RMS sound pressure, $\tilde{p}^2$: (Eq. 2.1.12) simplifies to (Eq. 2.1.1) as pressure and velocity are of equal phase and hence $\cos(\tilde{p}, \tilde{v}) = 1$. This is often called impedance effect. As this approximation is only valid in the far field of the sound source, its accuracy increases with increasing distance from the sound source. Studies using real sound sources have shown that this impedance effect is less than 1 dB at a distance of 1 m from the surface of the sound source [19].

$$\tilde{p}\tilde{v} \cos(\tilde{p}, \tilde{v}) = \frac{1}{\rho_0 c} \tilde{p}^2 \tag{2.1.12}$$

Second, the angle effect is based on the assumption that the used meas-

urement surface is perpendicular to the sound intensity emitted by the sound source in all points. This assumption allows the replacement of the sound intensity vector (Eq. 2.1.9) by sound pressure (Eq. 2.1.10) - a scalar. This in turn allows for the determination of sound power using pressure microphones.

However, for real sources the determination of such measurement surfaces is very complicated and requires in-depth preliminary studies on the structure of the sound field emitted by the source. The error that results from measurement surfaces that are not perpendicular to the sound intensity vector is hence called angle error. The larger the radius of the measurement surface is, the smaller the angle error becomes [34].

Thirdly, the most obvious effect is the sampling effect. As described previously, sound power is given as surface integral over the sound intensity emitted by the sound source (Eq. 2.1.9). In real set-ups it is practically impossible to measure the sound intensity continuously over the measurement surface. For this reason, simplifying assumptions are made that allow for the transition from the integral to the discretised form of sound power (Eq. 2.1.11). In simplified form, the sound power, P, is thus given as sum over the individually recorded squared RMS values of sound pressure, $\tilde{p}_i^2$, each with associated surface area, S_i (Eq. 2.1.13) [34].

The magnitude of the sampling effect is difficult to quantify as it is highly individual to each sound source. It is dependent on the amount of scattering of the sound pressure on the measurement surface. In general, a larger number of sampling points will decrease the sampling effect as the directivity of sound emission with its associated scattering in sound pressure is captured more accurately. In reality, this gain in accuracy has to be balanced with the increased amount of time needed to realise measurements on a larger number of points.

$$P = \frac{1}{\rho_0 c} \sum_{i=1}^{n} \tilde{p}_i^2 S_i \tag{2.1.13}$$

Lastly, a set of corrections has to be applied that accounts for the experimental environment. The first of these corrections is the environmental correction, K_2. It is necessitated by imperfections in the sound field

provided by the free field room. In real rooms two counteracting requirements have to be balanced. On the one hand, one should try to maximise the distance to room walls to avoid recording any remaining reflections that occur despite the absorbing material. On the other hand, the distance from the sound source also has to be maximised so as to keep the near-field and angle error minimal. Hence, measurements in real rooms always occur in imperfect sound fields. The amount of imperfection is described by the aforementioned environmental correction, K_2 [34].

The next correction term approximates inaccuracies that are due to background noise. These can be caused by air turbulences around the measurement microphones, by reflections or by secondary sound sources. One critical point is the introduction of the measurement equipment into the measurement environment. Even if the equipment is kept small in size or diameter in comparison with the investigated wavelength, it should be noted that reflections do occur on its surfaces. These reflections can influence results, especially if they occur close to the measurement microphones. To correct for any background noise, the correction term K_1 is calculated. The last correction term accounts for different meteorological conditions that are encountered during measurements and is denoted as K_0. As it is typically very small, it is only used in precision measurements [34].

To calculate sound power levels including all correction terms requires the mean sound pressure levels, $\overline{L_p}$, on the measurement surface, S, referenced to the measurement surface $S_0 = 1\ \mathrm{m}^2$ and subtracting the environmental correction, K_2, the background noise correction, K_1, as well as the correction for meteorological conditions, K_0 (Eq. 2.1.14). However, this representation does not account for the near-field, the angle and the sampling error [34].

Even with all correction terms applied, the measurement uncertainty of this as well as other standardised methods is not known. Instead it is estimated from round robin tests. The lowest measurement uncertainty associated with any sound power estimation is given as 0.5 dB in ISO 3745 where the scientific validation of this number is unknown [22].

$$L_\mathrm{W} = \overline{L_p} + 10\log(S/S_0) - K_1 - K_2 - K_0 \tag{2.1.14}$$

Considering the sound intensity method, the same sources of uncertainty could be considered. The near-field effect does not occur in this method, though, as it measures the vectorial quantity intensity and not the scalar quantity pressure. This means that measurements can be performed much closer to the surface of the sound source. This is also advantageous in terms of reduction of the influence of background noise. Also, the angle effect is irrelevant for this method as only the normal component carries power through the surface. The sampling effect, however, occurs in equal form as in the free field method. Undersampling of the sound field leads to an equivalent sampling effect as encountered during pressure measurements.

The influence of background noise on the results of the intensity method is much smaller than in the free field method. One reason for this is that in the intensity method a vector with directionality is measured. Hence, once the intensity is integrated over the entire measurement surface, any noise signal that enters and exits the surface is eliminated. The second reason is that the temporal average of the instantaneous sound intensity of noise sources vanishes in every measurement position. This effect can for instance be exploited close to sound hard surfaces of a sound source [34].

2.1.2 Volume measurement method

So far, the discussed measurement methods were applicable to (hemi-) anechoic environments only. Accurate sound power measurements can, however, also be performed in reverberation chambers (Fig. 2.1.1c). If a sound source, whose sound emission is temporally stable is run inside such a reverberation room, an equilibrium state between sound power emitted by the sound source and sound power absorbed by the room is eventually reached. This allows for sound power determination from sound pressure measurements using the spatial mean of the square of the RMS sound pressure, $\overline{\tilde{p}^2}$, and the equivalent absorption area of the room, A (Eq. 2.1.15). The corresponding sound power level determination uses the spatial and energetic mean of the sound pressure level, $\overline{L_p}$, and the reference value for the equivalent absorption area of the room of $A_0 = 4$ m^2 (Eq. 2.1.16) [34].

$$P = \frac{1}{4}\frac{\overline{\tilde{p}^2}}{\rho_0 c}A \tag{2.1.15}$$

$$L_{\mathrm{W}} = \overline{L_p} + 10\log\frac{A}{A_0} \qquad [\mathrm{dB}] \tag{2.1.16}$$

This method is dependent on the assumption that sound emission is temporally stable. As in-stationary sources are not considered in this work, their specific requirements are not dealt with here.

2.1.2.1 Problems with the Volume Measurement Method

Similar to the free field methods, there are non-standard sources of error that need to be considered for the volume measurement method. The quality of the diffuse sound field is of central importance. This quality is largely determined by the modal overlap between adjacent eigenmodes. The more eigenmodes overlap, the more even the energy distribution is within frequency bands. The modal overlap factor, M_{of}, describes this overlap. It is calculated as ratio of 3 dB modal bandwith, $\Delta f_{3\mathrm{dB}}$, to average frequency spacing between mode frequencies, Δf (Eq. 2.1.17). Larger values of M_{of} correspond to larger overlap.

Given a desired modal overlap factor, a cut-off frequency, f_M, can be calculated using the reverberation time, T_{rev}, the room volume, V, as well as the speed of sound in air, c (Eq. 2.1.18). This cut-off frequency defines the lower frequency limit associated with the chosen value of M_{of}. It is common to use $M_{\mathrm{of}} = 3$ which refers to the Schroeder cut-off frequency, f_{S}. It defines the lower frequency limit from which on a given sound field can be considered diffuse (Eq. 2.1.19 - valid in air) [15].

$$M_{\mathrm{of}} = \frac{\Delta f_{3\mathrm{dB}}}{\Delta f} \tag{2.1.17}$$

$$f_M = \sqrt{\frac{M_{\mathrm{of}} T_{\mathrm{rev}} c^3}{8.8\pi V}} \tag{2.1.18}$$

$$f_{\mathrm{S}} = 2000\sqrt{\frac{T_{\mathrm{rev}}}{V}} \tag{2.1.19}$$

Optimising the diffuse field that is provided by the reverberation room can

be a very time-consuming task. Walls should be primed or painted. Resonance absorbers can be installed to increase the accuracy of measurements in lower frequency ranges. Furthermore, the specific acoustic impedance is dependent on the position of the source within the measurement room. Hence, differences in determined sound power levels of up to 20 dB can result from different positions of the sound source in the measurement room.

Similar to the free field method, the number of measurement positions also plays a role in the accuracy of the determined sound power level. Measurements can either be taken at discrete positions or along a microphone path. If discrete positions are used, the distance between measurement points has to be at least half of the airborne sound wavelength of the frequency measured. The same distance has to be respected when moving the sound source itself. No measurements should be taken within a distance from room walls or the sound source itself of one quarter of the airborne sound wavelength, $\lambda/4$. In this area the energy density is increased due to interferences between incident and reflected sound rays. The correction term K_{01} accounts for this increase in energy density.

Other correction terms used in the determination of sound power correspond to their free-field method equivalents. Specifically, the background noise correction, K_1, and the correction for meteorological conditions, K_0, are utilised as well. Finally, using the measurement results on the spatial average of the sound power level, $\overline{L_p}$, the equivalent absorption area of the measurement room, A, the reference value to the equivalent absorption area, $A_0 = 4\mathrm{m}^2$, and the correction terms, the sound power level can then be determined with an accuracy that is comparable to that of the free-field methods (Eq. 2.1.20) [34].

$$L_\mathrm{W} = \overline{L_p} + 10\log\frac{A}{A_0} + K_{01} - K_1 - K_0 \tag{2.1.20}$$

2.2 Traceability of the Measurand Sound Power

All of the previously described measurement methods suffer major limitations. Firstly, the frequency range that is measurable is limited by room size. The larger the room size, the lower the minimum frequency

measurable. This is simply due to the fact that the wavelength increases with decreasing frequency. However, the size of the room being built is rarely dependent on the minimum frequency that is to be achieved, but rather on the more practical issues of space and funds available.

Secondly, all methods discussed place the measurement equipment within the sound field. The distortion that is caused by this, is not easily quantifiable and even if it is kept to a minimum, placing probes within the measurement medium is not scientifically correct in the strictest sense. Thirdly, and most importantly, there is no metrological traceability of the measurand sound power. Metrological traceability describes a chain of calibrations that relates the measurement result of an end-user product to the International System of Units (Fig. 2.2.1). The International System of Units (SI) relying only on the seven base quantities length, mass, time, electric current, thermodynamic temperature, amount of substance, and luminous intensity stands at the top of the traceability pyramid and is represented by the Bureau International des Poids et Mesures (BIPM). National primary standards are developed and housed at National Metrology Institutes (NMIs). These are realisations of derived quantities, such as sound power, whose constituents are more than one base unit. The national primary standards are referenced to the base quantities by means of calibrations which yield a measurement result including its uncertainty. In this way, the accuracy of a measurement result using the national primary standard can be related to the International System of Units [26][46].

Each level down the traceability pyramid progresses in the same way. Test samples are measured using the same derived unit as the previous level and are referenced to it by means of calibration measurements. In this way, the measurement uncertainty propagates through all levels of the traceability pyramid, ensuring that even the lowest level end-user product can be traced to the International System of Units. This ensures comparability between similar products within their given accuracy levels as all products are based on the same seven base quantities [46].

It should be obvious that metrological traceability is a key component in the scientific field. However, in sound power measurements it does not exist. There is no primary standard for sound power. As described previously, measurements are obtained using pressure or intensity probes.

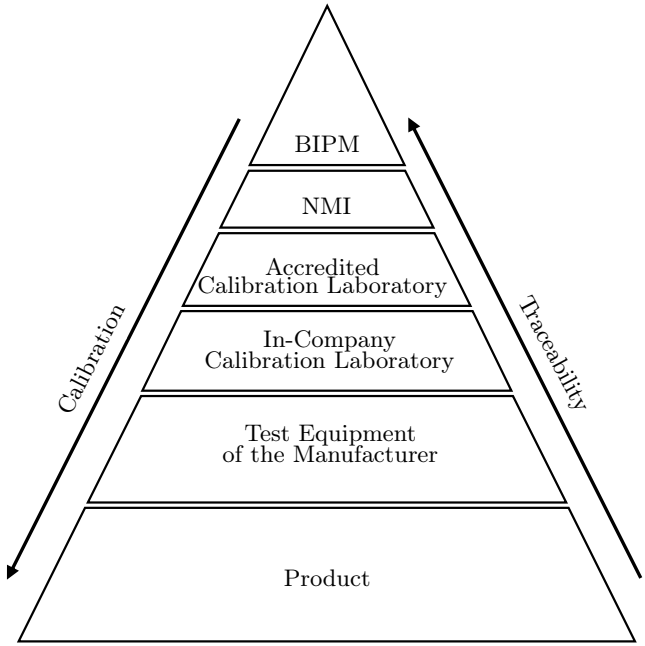

Figure 2.2.1: The metrological traceability pyramid (adapted from [46]).

Even if these probes themselves are calibrated and traceable, they cannot ensure traceability of the unit Watt as they do not measure Watt. Using measurement equipment of one derived unit to establish traceability of another derived unit is simply not possible [26].

There exist so called reference sound sources which undergo a "calibration" procedure. However, this "calibration" is not a scientifically correct calibration against SI units but rather a measurement under specified conditions which has to yield results within a known range. The accuracy of these reference sound sources is established in round robin tests and the sources themselves have to follow guidelines on spectral behaviour and directivity. Hence, they are restricted on the type of noise that they emit [23].

This lack of traceability leads to the dilemma that measured sound power levels may vary depending on the measurement standard obeyed (Fig.

2.2.2). Establishing traceability of the unit Watt in airborne sound would thus be an essential improvement in sound power determination.

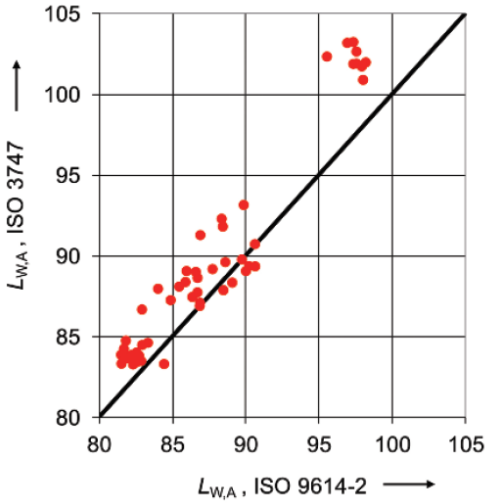

Figure 2.2.2: A-weighted sound power levels measured in round robin tests on different machines by different teams (from [40]). Perfect correspondence between standards would have led to all dots being located on the diagonal.

2.3 Realisation of the Unit Watt without Measurements in the Sound Field

From the previous discussion it follows that establishing a primary standard for the unit Watt in airborne sound had to assure two main objectives: moving the measurement equipment out of the sound field and measuring SI units directly and henceforth deriving the unit Watt. Such a measurement set-up was found using an embedded oscillating solid body and measuring its surface's movement with a laser-scanning vibrometer (Fig. 2.3.1).

Specifically, the technical realisation consisted of a piston that was attached to an electrodynamic vibration exciter. This apparatus was lowered into

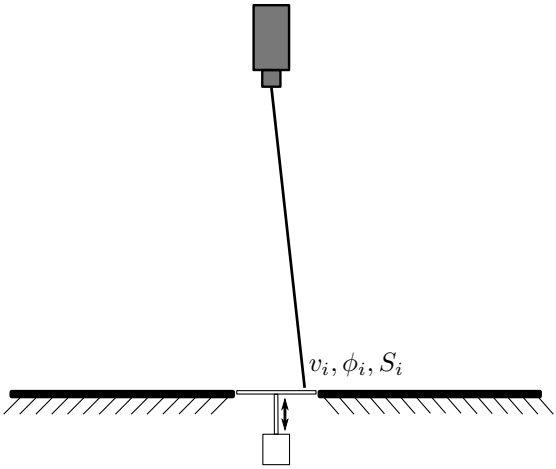

Figure 2.3.1: Schematic of the measurement set-up. Oscillating piston with measured quantities movement velocity, phase angle and surface area.

a hole in the floor of a hemi-anechoic room such that the piston surface and floor of the room were in the same plane, keeping the gap between piston and floor and any elevation differences between the two surfaces as minimal as possible. The vibration velocity of the piston was measured by a laser scanning vibrometer, whose laser was pointing through a hole in the roof of the hemi-anechoic room. The laser moved along a pre-set path of individual measurement points across the piston's surface and, for each point i, measured the quantities peak velocity, v_i, corresponding phase in relation to input current, ϕ_i, as well as x- and y-coordinate in a pre-defined reference grid. The coordinates allowed for a calculation of the area S_i that the measurement point represented.

The sound power output of this device could then be calculated using the discretised Rayleigh's integral, with the notation used as follows (Eq. 2.3.1)[16][18].

- k - wave number
- ρ_0 - density of air
- c - speed of sound in air

- $\tilde{v}_i$ - movement velocity (RMS value) of i-th point
- ϕ_i - associated phase angle (in relation to input current) of i-th point
- S_i - surface area represented by i-th point
- d_{ij} - linear distance between i-th and j-th point

$$P_{\text{Rayleigh}} = \sum_{i=1}^{N} \frac{\rho_0 c}{2\pi} k^2 \tilde{v}_i^2 S_i^2 + \\ + 2 \sum_{i=1}^{N} \sum_{j=i+1}^{N} \frac{\rho_0 c}{2\pi} k^2 \tilde{v}_i \tilde{v}_j S_i S_j \frac{\sin(kd_{ij})}{kd_{ij}} \cos(\phi_i - \phi_j) \tag{2.3.1}$$

The laser-scanning vibrometer itself was calibrated by the manufacturer assuring traceability to the SI units. Hence, this set-up conformed to the objectives that had to be fulfilled in order to assure traceability to the SI units: Measurements outside the sound field as well as all parameters being traceable themselves. In theory, there are no restrictions on the velocity distribution on the piston's surface and there is no requirement of linearity between input voltage to the vibration exciter and vibration velocity. An uncertainty level of 0.5 dB for the realisation of the unit Watt thus seemed realistic [43].

2.3.1 Reasoning for the proposed method

The proposed method of traceable sound power determination is by no means unique. For example, volume flow sources such as the one described in [4] could have been chosen to reach the same goal. However, the distinct characteristic of the Rayleigh integral is that it relies on oscillation measurements. Modern measurement equipment such as laser-scanning vibrometers are able to sample the corresponding quantities velocity and phase very accurately. In fact, the uncertainty in their measurement results is negligible. Paired with the independent sampling of a large number of data points, the proposed method based on the discretised Rayleigh integral promised to be very robust and fairly easy to implement. For this reason, the method was chosen. In the future, a choice of alternative measurement methods could, however, also be possible.

2.3.2 Acknowledgement of outside help and description of author's contribution

In order to give a comprehensible and complete report on the investigated primary sound sources, certain topics are elaborated in this work even though they do not form direct part of the author's work. Instead, these were contributed as input from colleagues. The topics in question are measurements and design of physical realisations of the primary standards (Chp. 3). While the author gave ideas on desired discretisations and input voltage for measurements, these were carried out by colleagues of the Applied Acoustics working group at PTB Braunschweig. This included decisions on input signals and set-up of equipment.

Furthermore, the first six physical realisations of primary standards had already been developed when the author joined said working group. Her work gave input to the seventh and eighth primary source described in later parts of this work (Sec. 3.3). To be specific, the author conducted analytical calculations on the influence of major design parameters such as piston radius and mass as well as expected emission characteristics (Chp. 4). However, the author neither built nor conceptualised the explicit design of those sound sources. Both of these assignments required task specific experience, which was afforded by the most qualified members of the working group.

Besides the design input, the author's contribution, thus, began at the stage after data acquisition. The most important aspects of her work were the demonstration of the convergence of the discretised Rayleigh integral including a determination of minimally required discretisation sizes (Chp. 5) as well as the establishment of a procedure to enumerate the uncertainty associated with sound power levels returned by the discretised Rayleigh integral (Chp. 6). In applying the developed strategies to measurement data, the quality of current primary standards and applied experimental methods were evaluated by the author (Chp. 7 - 8).

As the author's contribution is in large parts of general validity, it is independent of the specific physical realisations of primary standards investigated and could have been presented in this manner. However, a large number of results was developed on the basis of measurement data. Most importantly, this work was designed to support ongoing, active research rather than produce textbook results. As such, it would have been hardly

understandable, if the author had just elaborated on her own contributions without placing them in reference to the instrumentation and methods used to derive and apply them. For this reason, pertinent topics that were outside the scope of the author's work are included in this work.

3 | Measurements

In later chapters measurement data will be evaluated. In order to make their origin transparent and understandable, this chapter is devoted to the thorough documentation of applied procedures. This includes descriptions of the utilised measurement environments, protocols and physical realisations of primary standards. Furthermore, the thought process guiding the evolution of primary standards is documented.

For clarity, it should be reiterated that the physical sound sources and measurement data were input to the author's work that was contributed by colleagues of the Applied Acoustics working group at PTB Braunschweig.

3.1 Measurement Environments

The two measurement environments used were a hemi-anechoic and a reverberation room. Their general characteristics were described previously (Sec. 2.1), so that here the focus will be on the description of the physical rooms, which were used for measurements.

3.1.1 Hemi-anechoic room

The primary measurement environment was PTB's hemi-anechoic room. Its characteristic is that is has a fully reflective floor surface while all other room walls absorb incoming sound waves (Sec. 2.1). With the sound absorbing wedges installed in the room, it has a length of 6.5 m, a width of 6.25 m and a height of 4.65 m. The remaining room volume is approximately 184 m^3 with a cavity for the primary sound source in the floor which is slightly off centre (Fig. 3.1.1). Due to spatial restrictions, one corner of the room is not rectangular.

In the ceiling of this hemi-anechoic room, a hole was constructed. It was situated vertically above the cavity of the sound source. The laser-scanning vibrometer was placed on the outside of the hemi-anechoic room ceiling such that its laser was pointing through the ceiling hole directly onto the surface of the primary sound source.

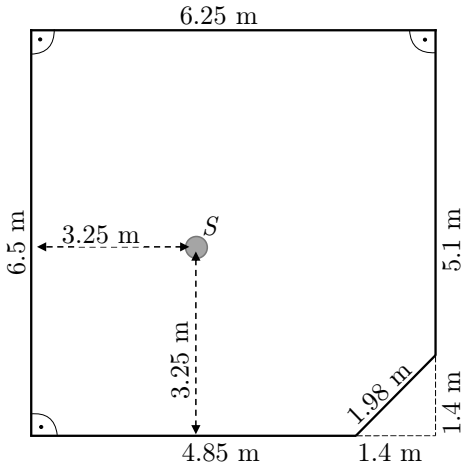

Figure 3.1.1: Constructional drawing of PTB's hemianechoic chamber. Room height with installed sound absorbing wedges is 4.65 m. Each wedge has a length of 0.8 m. S denotes the position of the sound source.

3.1.1.1 Absorption measurements in Kundt's tube

PTB's hemi-anechoic room is qualified for sound power measurements using sound pressure methods from 100 Hz on. This refers to the within-sound-field measurements of the sound pressure methods (as discussed in Sec. 2.1). The lower limit is established by the absorptive properties of the wedges that are installed along the room walls. In a hemi-anechoic environment only direct sound emission from the source is desired. This means that all reflections from room walls have to be absorbed by the wedges. For very low frequencies this is not possible due to the long wavelengths of the impinging waves. Hence, the frequency dependent absorption coefficients of the wedges determine the "cut-on" frequency from which on they are able to absorb incoming sound waves.

To characterise and verify the performance of PTB's insulating wedges from 100 Hz on, measurements were performed in a Kundt's tube. To do so, four wedges were removed from the walls of the hemianechoic room and divided into two sets of two wedges each. Both sets of wedges were measured with both horizontal and vertical installation of the wedges in

the Kundt's tube (Fig. 3.1.2). A repeat measurement for the second set of wedges was performed, where the wedges were aligned horizontally and flipped between measurements.

(a) Sound absorbing wedges from PTB's hemianechoic room. The length of each wedge is 0.8 m.

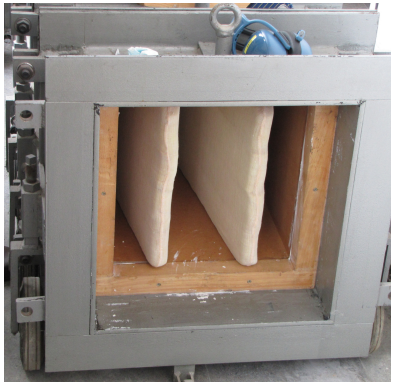

(b) Installed set of 2 wedges in Kundt's tube.

Figure 3.1.2: Pictures from absorption measurements of sound absorbing wedges in Kundt's tube.

In total, the following six experiments were performed, where for each measurement the frequency dependent impedance, Z_{Wedges}, with both real and imaginary component was recorded.

Experiments:

1. Wedge set 1 installed horizontally
2. Wedge set 1 installed vertically
3. Wedge set 2 installed horizontally
4. Wedge set 2 installed vertically
5. Wedge set 2 installed horizontally (repeat measurement)
6. Wedge set 2 installed horizontally (repeat measurement - flipped top/bottom wedge)

All data sets show equivalent results. Hence, the mean values with corresponding standard deviations were used for further calculations. From the measured impedances, both the frequency dependent reflection coefficients, r_{Wedges}, as well as the corresponding absorption coefficients, α_{abs}, could be calculated (Eqs. 3.1.1 - 3.1.2). Results show that around 70 Hz, the absorption coefficient of the wedges reaches 0.96. By 100 Hz, it rises to 0.97 and beyond 125 Hz, the absorption of the wedges is at more than 99% (Fig. 3.1.3). This gives rise to the claim that measurements with the laser-scanning vibrometer (from outside the sound field) and those with pressure or intensity probes (from within the sound field) for frequencies larger than 125 Hz are comparable.

$$r_{\text{Wedges}} = \frac{Z_{\text{Wedges}} - 1}{Z_{\text{Wedges}} + 1} \tag{3.1.1}$$

$$\alpha_{\text{abs}} = 1 - |r_{\text{Wedges}}|^2 \tag{3.1.2}$$

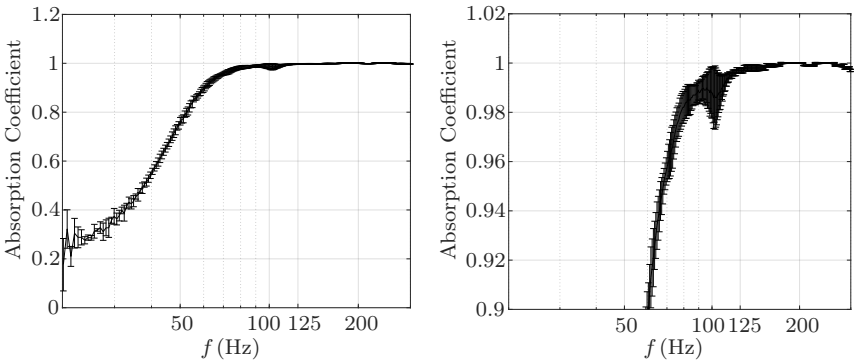

(a) Mean absorption coefficients including standard deviations over frequency.

(b) Mean absorption coefficients larger than 0.9 including standard deviations.

Figure 3.1.3: Measured absorption coefficients of sound absorbing wedges in Kundt's tube.

3.1.2 Reverberation room

The secondary measurement environment, that was used for measurements, was PTB's reverberation chamber with non-rectangular walls. As

described previously (Sec. 2.1), reverberation rooms are characterised by having only reflective walls, which are to completely reflect any incoming sound waves.

PTB's reverberation chamber is qualified for sound power measurements using sound pressure methods from 100 Hz on. The volume of this room is approximately 200 m^3. Diffusers can be hung from the ceiling in different configurations. Just as in the hemi-anechoic room, there is a cavity in the floor of this reverberation room, which allows for the installation of the primary sound source such that its surface is in plane with the surrounding floor (Fig. 3.1.4). The cavities in both the hemi-anechoic as well as the reverberation room are of the same diameter.

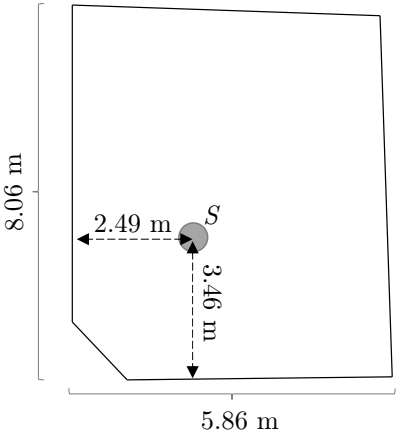

Figure 3.1.4: Constructional drawing of PTB's reverberation chamber with non-rectangular walls. Room height above the primary sound source, S, is 5.02 m.

3.2 Measurement Protocols

For each measurement with the laser-scanning vibrometer, the first step was the definition of a grid. This grid represented a collection of all the points - defined by their x-, y- and z- coordinate - that the scanning vibrometer was to measure. Grid sizes commonly used were of 509, 725,

1425 and 3045 points (Fig. 3.2.1a). All grids were set up with equidistant points. They all included points on the piston itself as well as on the surrounding baffle (Fig. 3.2.1b). This was needed to quantify the undesired yet unavoidable energy transfer from the piston to the surrounding plate and baffle. The grid centre was positioned as best as possible at the piston centre.

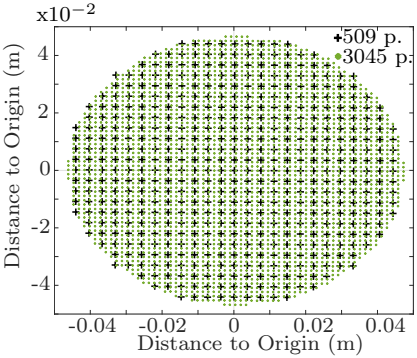

(a) Exemplary comparison of smallest 509 point grid to largest 3045 point grid with diameter of sampled area remaining constant.

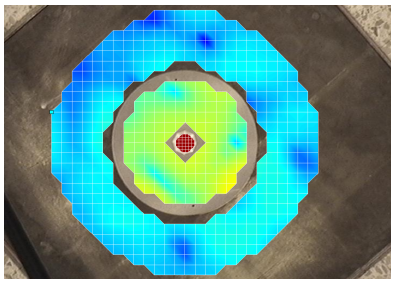

(b) 509 point grid. Dark red central area covered the piston surface, green middle area the supporting plate and the blue outer area measured the brass plate which is part of the room floor.

Figure 3.2.1: Depiction of measurement grids.

The excitation of the piston by the shaker used a fixed phase multi-sine signal. At each grid point, the vibrometer conducted ten measurements before reporting the mean value of these ten measurements as experimental result. No window was applied. The input voltage was chosen in accordance with the manufacturer's specification table. Pre-tests with varying input voltages were used to assure that the primary sources were operated within ranges where sound power output and input voltage showed linear dependence.

The frequency range measured was from 20 Hz to 20 kHz with a resolution of 3.125 Hz. This corresponds to 6400 frequency lines. The frequency dependent quantities measured for each grid point were the amplitude of its movement velocity (in dB) as well as the corresponding phase in relation to the input voltage (in degrees). Amplitudes were measured

as peak values. Furthermore, the frequency independent x-, y- and z-coordinate of each grid point was noted.

Comparative measurements to standardised methods were performed using primarily the enveloping surface method with sound pressure probes (as described in Sec. 2.1). A select few measurements in the hemianechoic room, however, were also conducted using intensity probes. Both sound pressure and intensity measurements were performed using one of two stainless steel arcs (Fig. 3.2.2). To each one of these arcs up to 24 microphones could be attached using acrylic glass rods of 70 cm in length. The glass rods enabled the choice of different radii as they could be moved further inward or outward of the arcs. Microphone positions were chosen such that each microphone covered the same partial surface area. The arcs were moved by a motor, which was placed outside the hemianechoic room. The motor-arc connection was realised using a metallic wire [7].

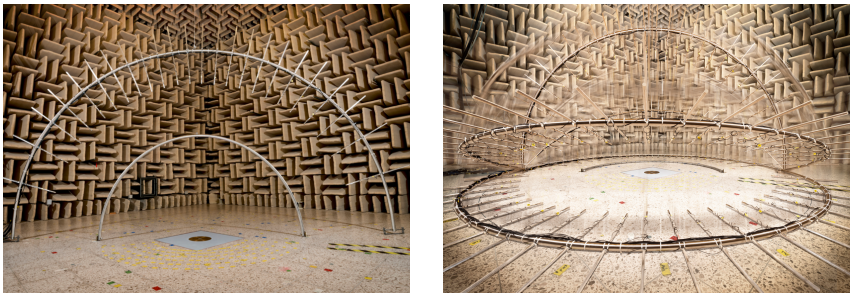

(a) The two stainless steel arcs centred over the primary sound source.

(b) Illustration of the movement of the larger arc over the primary sound source.

Figure 3.2.2: Pictures of the semi-circular arcs used for sound pressure and intensity measurements in PTB's hemianechoic room. Each arc could fit up to 24 microphones which were attached to acrylic glass rods of 70 cm length.

The same excitation signal as for the laser-scanning vibrometer experiments was used for pressure and intensity measurements. For pressure measurements, the same frequency range of 20 Hz - 20 kHz was sampled. As noted previously, intensity measurements were only performed in the hemianechoic room with a frequency range of 20 Hz - 10 kHz. For fur-

ther details the reader is referred to [5] where also the progress on the dissemination of the unit Watt is documented.

3.3 Primary Sound Power Sources

During the author's time at PTB Braunschweig, eight different pistons were used in experiments (Fig. 3.3.1). The present work is based on the results obtained from these sources. For completeness, it should be noted that more recently further primary sound sources were developed [32]. The different pistons used for the eight sources that are relevant to this work were as follows:

- Source 1: acrylic glass piston (Fig. 3.3.1a),
- Source 2: piston of a combustion engine (Fig. 3.3.1b),
- Source 3: aluminium piston of same diameter as Source 2 (Fig.3.3.1b, centre),
- Source 4: Teflon piston of same diameter as Source 2 (Fig. 3.3.1b, left),
- Source 5: aluminium piston with Teflon rings - same diameter as Source 2 (Fig.3.3.1b, right),
- Source 6: aluminium piston of radius 2.8 cm with attached silicone sealing of width 1.5 cm (Fig. 3.3.1c).
- Source 7: cone shaped aluminium piston of 60 mm diameter where the gap between piston and baffle was sealed either with petroleum jelly or an adhesive plastic strip
- Source 8: same as Source 7 but without any sealant between piston and baffle (Fig. 3.3.1d)

In designing the different pistons, the primary restraint was that the piston-shaker assembly had to be manufactured such that it could be embedded into the hole in the floor of PTB's measurement rooms with the piston surface forming a perfect alignment with the flooring. The cavities in both measurement rooms were identical except for their height. They had a diameter of approximately 0.3 m. The piston diameters were only a fraction of that size. Hence, the remaining surface area of the cavity had

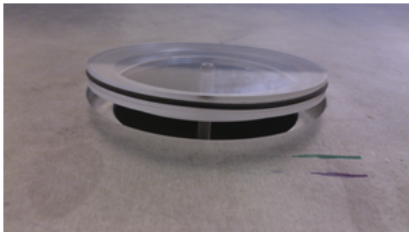

(a) Source 1

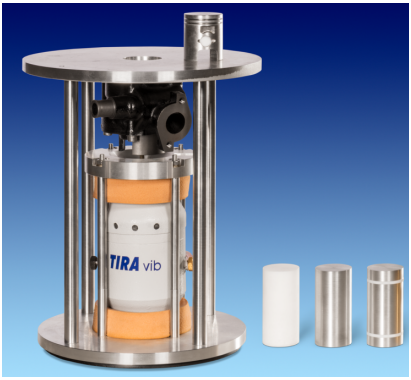

(b) Sources 2 (on top of the aluminium plate), 4, 3 and 5 from left to right.

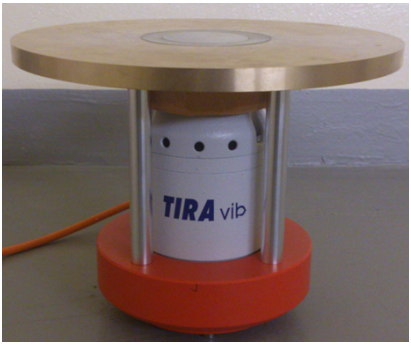

(c) Source 6

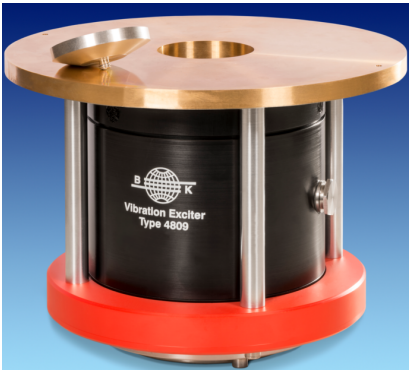

(d) Source 8

Figure 3.3.1: Different physical realisations of primary sound sources used for measurements.

to be covered with a supporting plate. Initially, aluminium was used as material for this plate (Fig. 3.3.1b). In later stages, a supporting plate made of brass was manufactured (Fig. 3.3.1c - 3.3.1d). This was done in order to impede surface motion of the supporting plate. As brass is a much more dense material than aluminium, the weight of the supporting plate increased significantly with the change of materials. The then much heavier supporting plate was much harder to excite and thus, the undesired sound emission from its surface decreased (Fig. 3.3.3).

When lowered into the cavity of the measurement room, the supporting plate was resting on a ledge. This is to say that the diameter of the cavity was enlarged at the top. The height of the supporting plate was chosen to exactly match the distance between the measurement room floor and the top of the ledge. In this way, the surface of the supporting plate, the surface of the piston and the room floor formed one even and edge-free surface. This is the basic condition necessary for the use of the discretised Rayleigh integral.

During the time of the author's investigations, only floor mounted shakers were available. These had to be connected to the supporting plate as the height of the final primary source assembly was consciously chosen to be smaller than the height of the cavity. From a constructional standpoint this meant that only the height of the supporting plate had to be controlled to highest precision but not the height of the entire assembly. This choice also allowed for the transfer of the source from one measurement room to the other. Furthermore, this almost free-hanging construction avoided energy transfers through side paths as much as possible.

Thus, the shakers were mounted onto a base plate. This plate was decoupled from the shaker and connected to the top supporting plate (see Fig. 3.3.1d for an example). Lastly, the pistons were connected to the shaker. This connection was realised by use of a rod, whose length was precisely such that the piston surface formed a perfect alignment with the surface of the supporting plate and the room floor. The gap between the piston and supporting plate was kept as small as possible in order to avoid acoustic short-circuits between the front and back side of the piston. Except for Sources 6 and 7, the gap was air-filled.

The choice of piston material and diameter was such that a maximum level of sound power output was aimed at. Each source needed to display a temporal stability of at least one hour in order to be able to perform measurements under constant conditions. A flat frequency response and monopole-like sound emission were considered as secondary design goals. As expected, over the course of measurements, knowledge was gained that led to an evolution of sources. This process will be discussed next with the aid of selected measurement data and results.

3.3.1 Evolution of primary sources

To describe the main design goals of the individual pistons, a look at a comparison of the frequency responses of the mean velocity levels on the piston surface is most helpful (Fig. 3.3.2). The first three sources were essentially used for pre-studies to develop a first understanding of the behaviour of this type of primary sound source. However, their piston velocity (not shown graphically) and thus their sound power output were far too small.

Especially for Sources 2 and 3, friction caused non-linearities in the frequency response. This friction occurred, on the one hand, between the piston and edges of the supporting plate. On the other hand, there also appeared to be friction between the piston and the combustion engine guide through which it moved (Fig. 3.3.1b - black piece). The guide's task was to inhibit any lateral motion of the piston. The occurrence of friction indicates that this was needed, which in turn was an indicator for bending in the rod that connected the piston to the shaker.

For this reason Source 4 was developed. It used Teflon as piston material with the idea that this softer material would emit more sound than the stiffer aluminium that was used for Source 3. Furthermore, it was hoped that through the use of Teflon, friction between the piston and supporting structures could be reduced significantly. Looking at the mean velocity levels on the piston surface of Source 4 (Fig. 3.3.2 - green line) shows that while sound power output did increase, friction still was critical. In fact, the erratic pattern of the velocity level that was caused by friction would have made it impossible to determine sound power levels with the desired uncertainty of 0.5 dB.

Hence, the next step in the evolution of sources was a combination of Sources 3 and 4 which led to the use of an aluminium piston with Teflon rings. However, while the mean velocity levels on the piston surface showed much less unpredictability than those of Source 4, the overall sound power output of this primary source was again far too small (Fig. 3.3.2 - dark red line).

In the next step then, the idea to use a combustion engine type piston was discarded altogether. This allowed for a more compact design of the primary source as the guide which assured the straight up and down

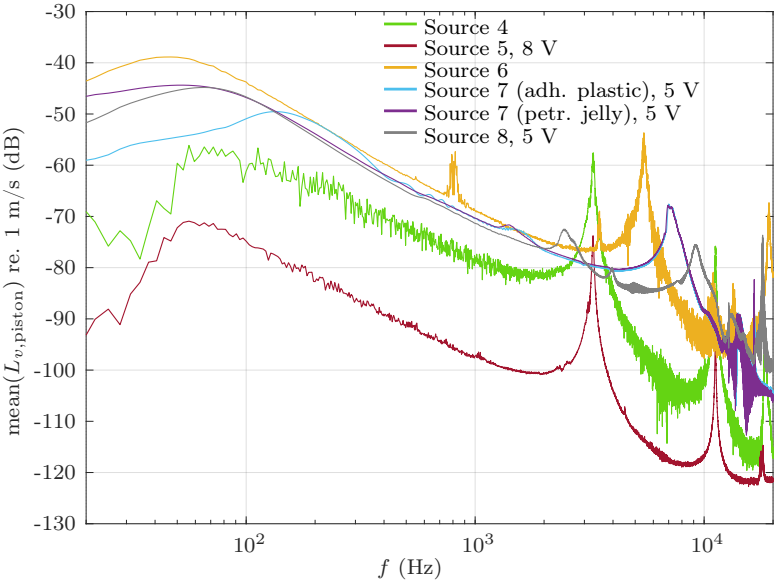

Figure 3.3.2: Comparison of velocity levels for pistons 4 to 8. Corresponding input voltage given where recorded.

motion of the piston could be removed (Fig. 3.3.1b - black piece). The main benefit of this development was that the rod, which connected the shaker to the piston, could be reduced in length. This reduction decreased its bending which in turn reduced friction. The piston was furthermore increased in diameter to produce larger sound output and the supporting plate made of brass to reduce its excitation (as discussed in Sec. 3.3). To seal the gap between piston and supporting plate, a silicone ring was affixed to the piston.

The results in terms of mean velocity levels on the piston surface were a stark improvement over Source 5 (Fig. 3.3.2 - yellow line). The effects of friction between piston and supporting plate were minimal, so that a much more smooth and reliable frequency response was obtained. However, Eigenmodes of the silicone sealing at around 800 Hz and 3.5 kHz appeared. Besides these, the frequency response was very much acceptable until the first piston Eigenmode at 5.5 kHz. Beyond this Eigenmode, though, the softness of the silicone sealing caused large fluctuations in mean piston

velocity levels as the silicone started to move strongly and unevenly (Fig. 5.2.16c).

This could also be shown by an analysis of the sound power contribution due to the different materials (Fig. 3.3.3a). For this investigation, the discretised Rayleigh integral was calculated individually for the points corresponding to different materials as well as for the entire assembly as a whole. For Source 6, one can see that the brass plate shows no excitation for frequencies below the first Eigenfrequency of the silicone sealing (Fig. 3.3.3a - yellow line). However, the first piston Eigenmode at 5.5 kHz is also clearly observable on the brass plate. Ideally, this transfer of energy would be avoided.

From its sound power contribution, the problematic behaviour of the silicone sealing can be seen very clearly (Fig. 3.3.3a - green line). Due to being a very soft material, silicone is only usable in the low frequency range. Already before the first Eigenmode, the silicone sealing disproportionally increases the sound power output of the entire assembly beyond the level that the aluminium part of the piston is able to attain (Fig. 3.3.3a - red vs. black line). After its first Eigenmode, the silicone sealing does not contribute significantly to the sound power output of the entire assembly until the first piston Eigenfrequency. After this, the noisiness that is due to its increasingly erratic motion is clearly visible in the sound power contribution of the silicone sealing. This leads to large fluctuations in the sound power output of the entire assembly. For this reason, the ideas to use softer materials and pistons made of more than one material were dismissed.

Besides a change in piston, also a different shaker was used for Source 7. This allowed for a further reduction in length of the rod that attached the shaker to the piston. With this, bending of this connecting rod, which in turn would lead to lateral motions of the piston and friction, was avoided as much as possible. The piston of Source 7 was cone shaped and made of aluminium. The gap between piston a supporting plate was manufactured such that it was less than 1 mm in width. To further seal this gap, either petroleum jelly or adhesive plastic strips were used. However, neither one of these sealants produced convincing results (Fig. 3.3.2 - purple and blue line). Especially the adhesive plastic strips significantly distorted the piston motion at low frequencies. Looking at the sound power contributions of the different materials also showed that due to the connection that

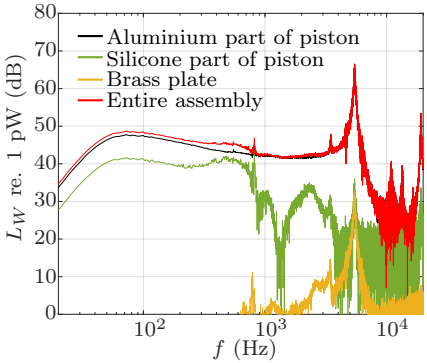

(a) Source 6, 509 point grid.

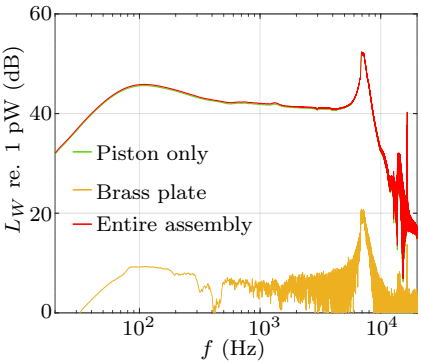

(b) Source 7 (petroleum jelly), 509 pts.

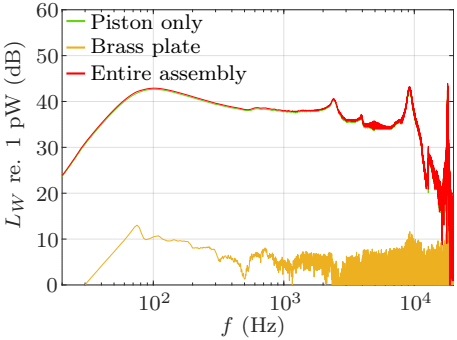

(c) Source 8, 509 point grid.

Figure 3.3.3: Sound power contribution of different areas on and around the piston as defined by their material composition.

the petroleum jelly and plastic strips provided, energy was transferred from the piston onto the surrounding brass plate (Fig. 3.3.3b). This is especially true for the first Eigenmode and should be avoided, if possible. Hence, the sealants were removed and the same source now featuring an air gap between piston and supporting plate labelled as Source 8 (Fig. 3.3.1d).

As desired, the air gap effectively decoupled the supporting brass plate from the piston (Fig. 3.3.3c - yellow line). The sound power contribution from the brass plate was negligible for the entire frequency range and no piston Eigenmodes visible in its sound power spectrum. In terms

of mean piston velocity level, Source 8 showed a first peak around 2.5 kHz (Fig. 3.3.2 - grey line). However, this does not appear to be an Eigenmode. Considering that Source 7 displays a similar though frequency shifted peak, suggests that this peak is not due to the air gap. Between 4 kHz and 6 kHz, though, the effect of the air gap is visible by causing another minor peak as well as a widening of the amplitude spectrum of the mean piston velocity levels. The air gap seems to act like a spring in that frequency range. The first Eigenmode of Source 8 occurs at 9 kHz. Beyond this, the frequency spectrum stays fairly scatter free in comparison to the other sources. However, it does display another non-Eigenmode peak around 13 kHz as well as the second Eigenmode at 18 kHz.

While even the eighth version of a primary source did not show fully satisfactory behaviour, improvements were clearly visible. As mentioned before, the work on the establishment of an ideal primary sound source is still ongoing [32]. While it could not be expected to fully answer all questions concerning primary sound sources in this work, especially the frequency responses of Sources 6 and 8 provided a basis from which conclusions concerning associated uncertainties as well as comparability to current state-of-the-art measurement protocols could be drawn. This will be documented in the following chapters.

4 | Characteristics of the Primary Standard

The evolution of primary standards at PTB has been documented (Sec. 3.3.1). Progress from one source to the next was, as can be expected, driven by the desire to improve emission characteristics. While this process initially focused on material choices, from the design of Source 6 (Fig. 3.3.1c) onwards, more fundamental characteristics of circular piston sources were taken into account; namely emission characteristics and influence of material choice. The corresponding analyses were performed by the author and will be documented in this chapter. While their contribution to the advancement of science may be marginal, they form an integral part to understanding the choices made in designing the physical realisations of primary standards relevant to this work. Furthermore, the interested reader should gain the tools to conceptualise own ideas for primary standards from this chapter.

4.1 Development of a Lumped Parameter Model

As a first step to analytical modelling, a lumped parameter model was built based on the general set-up to be used in measurements after [29]. As described previously, this general set-up consisted of a shaker and piston which were embedded into the floor of a hemi-anechoic room. A laser-scanning-vibrometer was mounted on top of the ceiling of the hemi-anechoic room so that it pointed through a hole in the ceiling directly onto the piston surface. The vibrometer measured the velocity and phase along the surface of the piston (Fig. 4.1.1). The goal in the development of the lumped parameter model was to calculate the sound power output of the piston for various settings. This served as a general guide in choosing optimal materials and equipment for measurements.

To develop the lumped parameter model, the shaker-piston set up was translated into an equivalent circuit diagram, with the shaker acting as electrodynamic transformer (Fig. 4.1.2) [29]. All variables used are detailed in the List of Symbols (page ix). The most important ones were:

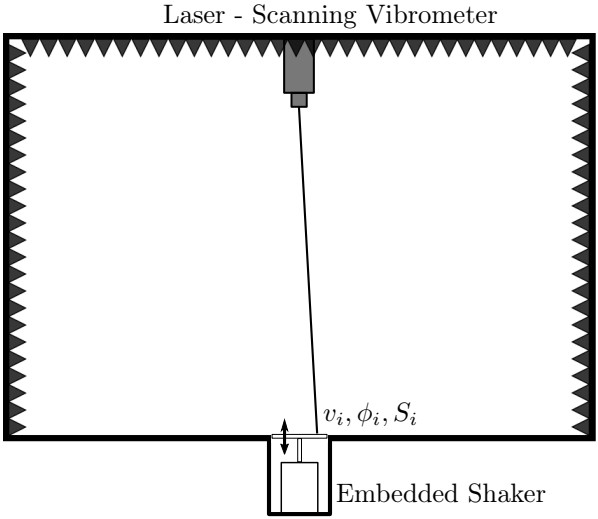

Figure 4.1.1: Sketch of the measurement set-up. The laser-scanning vibrometer pointed through a hole in the ceiling onto the piston surface (from [43]).

- m_{P} - mass of the piston and supporting rod
- r - radius of the vibrating piston
- V_{p} - volume of air behind the piston
- $x_{\max}$ - maximum displacement that the shaker could achieve
- $v_{\max}$ - maximum velocity that the shaker could achieve
- $a_{\max}$ - maximum acceleration that the shaker could achieve

Conversion from the electric to the mechanic side and vice versa used the given relations (Eq. 4.1.1 - 4.1.2) [29].

$$u_{\mathrm{sh}} = B_0 l \cdot v_{\mathrm{sh}} \tag{4.1.1}$$

$$i = \frac{F_{\mathrm{sh}}}{B_0 l} \tag{4.1.2}$$

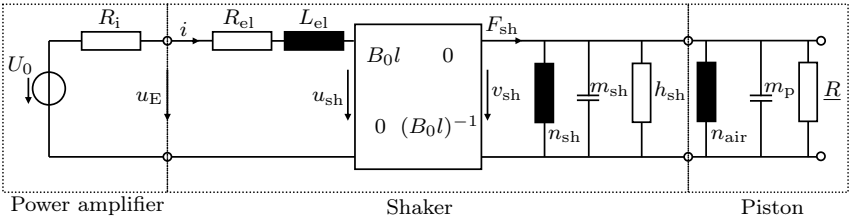

Figure 4.1.2: Equivalent circuit diagram of the shaker-piston set up.

Calculation of sound power was achieved using the Bessel and Struve function of the first kind, $J_1()$ and $H_1()$, respectively (Eq. 4.1.3 - 4.1.9) [10] [44]. The voltage u_E was measured as output of the power amplifier. Hence, it had been adjusted for the inner resistance of the shaker, R_i, which is why the effect of R_i was not included in the calculations. The equation describing the compliance of air behind the piston, n_air, (Eq. 4.1.9) is valid only for emitted wavelengths $\lambda_\mathrm{a} = (2\pi c)/\omega$ that are much greater than the dimensions of the cavity behind the radiating disc. However, in the present case, at frequencies where this condition was not met, the system was mainly controlled by mass.

For the shaker of the preliminary tests at PTB, parameter values are given (Tbl. 4.1.1). The equations denoted for sound power calculations (Eq. 4.1.3 - 4.1.9) list a dependency of the calculated quantity of both piston mass, m_P, and piston radius, r. However, upon choosing a material for the piston, the radius and weight of the piston will correlate. At this time, it was chosen to not include this correlation into the calculations because, this way, it was possible to evaluate different materials more easily.

$$P(\omega, m_\mathrm{P}, u_\mathrm{E}, r) = \rho_0 c \pi r^2 v_\mathrm{eff}^2 \left[1 - \frac{J_1(2kr)}{kr}\right] \tag{4.1.3}$$

$$v(\omega, m_\mathrm{P}, u_\mathrm{E}, r) = \frac{u_\mathrm{E} \cdot B_0 l \cdot Z_\mathrm{mech}(\omega, m_\mathrm{P})}{R_\mathrm{el} + i\omega L_\mathrm{el} + (B_0 l)^2 \cdot Z_\mathrm{mech}(\omega, m_\mathrm{P})} \tag{4.1.4}$$

$$v_\mathrm{eff}(\omega, m_\mathrm{P}, u_\mathrm{E}, r) = \\ = \frac{\mathrm{Min}(\omega^2 x_\mathrm{max}, \omega v_\mathrm{max}, a_\mathrm{max}, \mathrm{Abs}\left[v(\omega, m_\mathrm{P}, u_\mathrm{E}, r)\omega\right])}{\omega} \tag{4.1.5}$$

$$Z_\mathrm{mech}(\omega, m_\mathrm{P}, r) = \\ = \frac{1}{\frac{1}{h_\mathrm{sh}} + i\omega(m_\mathrm{sh} + m_\mathrm{P}) + \frac{1}{i\omega n_\mathrm{sh}} + \frac{1}{Z_{\underline{R_\mathrm{el}}}(\omega r)} + Z_{n_\mathrm{air}}(\omega r)} \tag{4.1.6}$$

$$k = \frac{\omega}{c} \tag{4.1.7}$$

$$Z_{\underline{R_\mathrm{el}}} = \rho_0 c \pi r^2 \left[1 - \frac{J_1(2kr)}{kr} + i\frac{H_1(2kr)}{kr}\right] \tag{4.1.8}$$

$$Z_{n_\mathrm{air}}(\omega, r) = \frac{\rho_0 c^2 \pi^2 r^4}{i\omega V_\mathrm{p}} \tag{4.1.9}$$

To visualise the sound power emitted by the shaker-piston set up for exemplary values of m_P, r and u_E, all equations were evaluated (Fig. 4.1.3). One interpretation of the results is as follows: The lines show the sound power output if 1 Volt is supplied separately for every frequency line, whereas the bars show the sound power output if 3.5 Volt are supplied over the entire bandwidth with pink noise. In equations, this is expressed as: $U_f = 1$ V, for the blue, red and orange line. For the bar chart $U_\mathrm{total} = \sqrt{\int_{20Hz}^{20kHz} U_f^2 df} = 3.5$ V with $U_f^2 = 1.77337 \cdot 1/f$ V^2/Hz.

The initial peaks of the lines – especially visible for the red and blue curves – stem from the mechanical impedance, Z_mech (Fig. 4.1.3). Taking the red curve as a basis, one can observe that the blue and orange curve have the same general shape as the red curve but are shifted due to the impact of differing values of piston mass, m_P. Between 100 Hz and 1 kHz, the red

Table 4.1.1: Parameter values for the shaker-piston assembly used at PTB for the shaker used with pistons one to six.

Quantity	**Parameter Value**	**Unit of Measure**	**Data Source**
R_{el}	3	Ω	[11]
L_{el}	450	μH	[11]
n_{sh}	1/3000	m/N	[11]
h_{sh}	4	s/kg	[11]
m_{sh}	$34.8{\cdot}10^{-3}$	kg	[11]
$B_0 l$	5.6	N/A	[11]
ρ_0	$1.2{\cdot}10^{3}$	kg/m^3	
c	343	m/s	
V_{p}	0.15	m^3	[11]
$x_{\max}$	0.005	m	[35]
$v_{\max}$	1	m/s	[35]
$a_{\max}$	643	m/s^2	[35]

line is almost flat with a loss of approximately 1 dB per octave. At 1 kHz the graphs slope downward. For the red line there is a loss of almost 6 dB between 1 and 2 kHz. Past 2 kHz, sound power output drops at around 12 dB per octave for the red line. This drop in sound power output is due to the electrical impedance from the shaker parameters, R_{el} and L_{el}.

The initial peak is given by the frequency for which the sound power level reaches its global maximum value. The point where sound power level starts to drop significantly can be found by analysing v/u_{E} (Eq. 4.1.10). Specifically, a high frequency approximation (Eq. 4.1.11) as well as a mid-range frequency approximation (Eq. 4.1.12) can be obtained. The intersection of these two approximation expressions (Eq. 4.1.13) yields the frequency at which the sound power loss of approximately 12 dB per octave commences (Fig. 4.1.4).

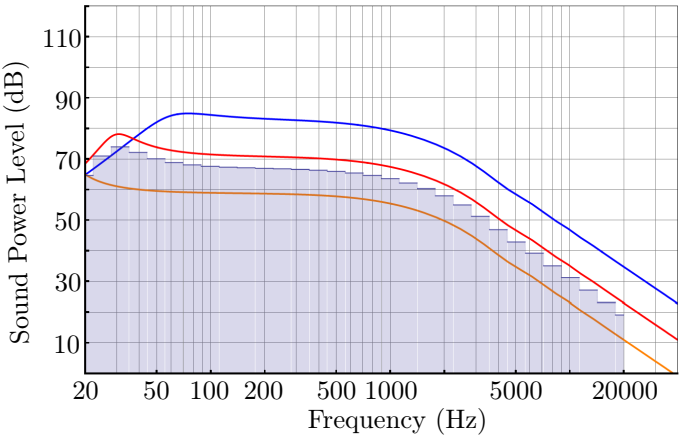

Figure 4.1.3: Sound power level for a reference value of $P_0 = 1$ pW. Parameter values chosen for the lines were: $u_\mathrm{E} = 1$ V, $r = 0.05$ m, $m_\mathrm{P} = 0$ kg (blue), $m_\mathrm{P} = 0.1$ kg (red), $m_\mathrm{P} = 0.5$ kg (orange). Bar chart: $u_\mathrm{Etotal} = 3.5$ V, $r = 0.05$ m, $m_\mathrm{P} = 0.1$ kg.

$$\frac{v(\omega, m_\mathrm{P}, r)}{u_\mathrm{E}} = \frac{B_0 l \cdot Z_\mathrm{mech}(\omega, m_\mathrm{P})}{R_\mathrm{el} + i\omega L_\mathrm{el} + (B_0 l)^2 Z_\mathrm{mech}(\omega, m_\mathrm{P})} \tag{4.1.10}$$

$$\mathrm{abs}(f_\mathrm{high}) = \frac{B_0 l}{4 f^2 L_\mathrm{el}(m_\mathrm{sh} + m_\mathrm{P})\pi^2} \tag{4.1.11}$$

$$\mathrm{abs}(f_\mathrm{mid}) = \\ = \frac{B_0 l \cdot c h_\mathrm{sh} r^2 \rho_0}{2 f h_\mathrm{sh} L_\mathrm{el} + 2 c f L_\mathrm{el} \pi r^2 \rho_0 + 2 c f h_\mathrm{sh}(m_\mathrm{sh} + m_\mathrm{P})\pi R_\mathrm{el} r^2 \rho} \tag{4.1.12}$$

$$f_\mathrm{intersect} = \\ = \frac{1}{2(m_\mathrm{sh} + m_\mathrm{P})\pi^2 r^2 \rho_0 c} + \frac{1}{2 h_\mathrm{sh}(m_\mathrm{sh} + m_\mathrm{P})\pi} + \frac{R_\mathrm{el}}{2 L_\mathrm{el} \pi} \tag{4.1.13}$$

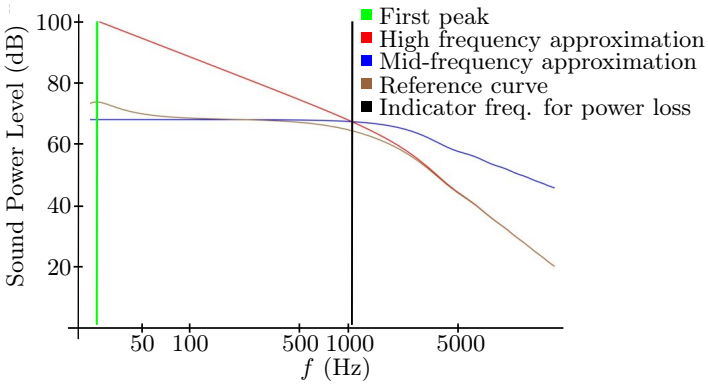

Figure 4.1.4: Analysis of sound power level obtained from the lumped parameter model. For values of $m_{\mathrm{P}} = 0.1$ kg, $r = 0.05$ m and $u_{\mathrm{E}} = 1$ V, the intersection frequency of the high and mid-range frequency approximation is given by $f_{\mathrm{intersect}} = 1062$ Hz and maximum sound power output occurs at $f_1 = 26.1$ Hz.

4.1.1 Comparison of measurement and calculated data

To test the significance of the analytical results, a comparison to measurement data was performed. The quantities evaluated were the velocity level and sound power level for a piston mass of $m_{\mathrm{P}} = 0.1$ kg and radius $r = 0.0495$ m. These correspond to the actual measurement set-up. Further parameter values were chosen as listed before (Tbl. 4.1.1).

Comparing the data from measurements and calculations, it should be noted that in the central frequency range from 200 to 1000 Hz, the experimental behaviour is fairly closely matched by the analytical calculation (Fig. 4.1.5). Outside this range differences are visible. The first low frequency Eigenmode that appears in the calculated data is not matched by the experimental data. It is due to the air volume behind the piston, which acts like a spring at low frequencies creating a spring-mass resonator. In the analytical calculation, this situation is modelled in its purest form and the resulting Eigenmode is prominent. In the experimental data, though, physical limitations in matching the perfect analytical case hinder the observance of the first Eigenmode. Most likely, an exchange of air through

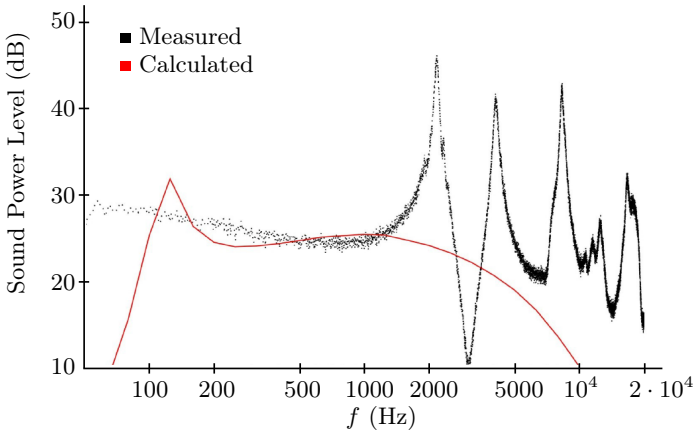

Figure 4.1.5: Comparison of measured and calculated sound power levels.

the gap between piston and surrounding baffle occurred at low frequencies. This would explain why the experimental data do not show the first resonance peak. Similarly, higher frequency Eigenmodes from the measurement are not matched by the calculated data. Reason being that the analytical model is valid only at those frequencies where its constituents are smaller than the corresponding wavelength. At 2 kHz this assumption ceases to hold. Hence, discrepancies between experimental and analytical data occur.

By comparing the set-up that was modelled in the analytic lumped parameter model (Fig. 4.1.6a) with the actual measurement set-up (Fig. 4.1.6b), the differences in level of difficulty are easily visible. Being able to match the sound power output of the physical set-up with a very simple model in the central frequency range of 200 Hz to 1 kHz is thus a good result.

These results could be improved (Fig 4.1.8) - especially in terms of matching the Eigenmodes - through modelling the piston by its impedance, Z_p, rather than as blunt mass (Fig. 4.1.7). The parameter value used for the impedance of the piston was calculated for a piston made of PMMA with radius, $r = 0.05$ m [38]. This almost exactly matches the piston used in the experimental set-up at PTB at that time.

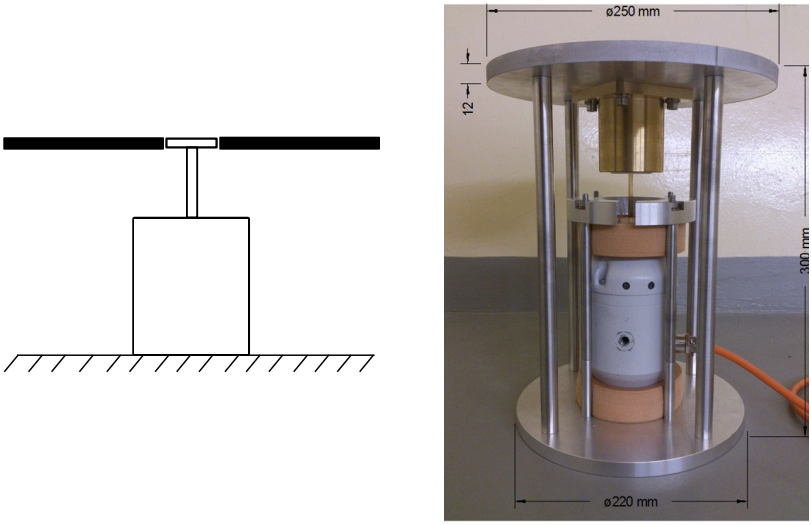

(a) (b)

Figure 4.1.6: Comparison of piston-shaker assembly modelled in the analytical study (Fig. 4.1.6a) and actual piston-shaker assembly used for measurements (Fig. 4.1.6b).

Even though this simple property change already showed the possibilities for improving the analytical calculation, more elaborate analytical models were not developed. Matching the actual set-up in great detail would have been very time consuming. As it was assumed that even with a detailed model prediction of the sound power level of the source to within acceptable tolerances over the entire frequency range would not be possible, development of further analytical models was disregarded.

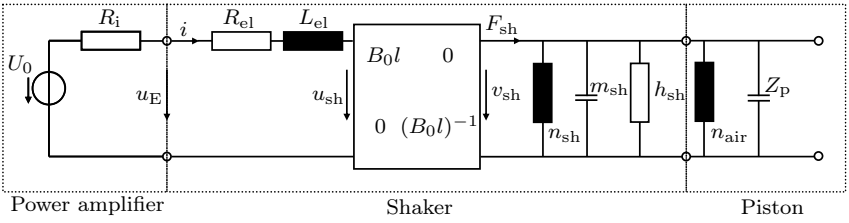

Figure 4.1.7: Lumped parameter model adjusted to model the piston by its impedance, Z_p, rather than its mass.

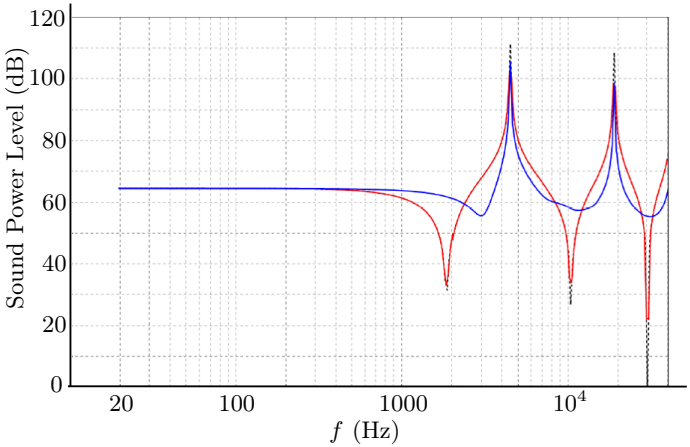

Figure 4.1.8: Sound Power Level from the lumped parameter model (red line) as well as from calculated Eigenmodes (blue line) for a piston of radius, $r = 0.05$ m, made of PMMA [38].

4.1.2 Influence of Major Design Parameters

Even though limitations in the usability of the lumped parameter model were found, it could still be used as a comparative tool to assess the influence of changes on key components of the piston-shaker set-up. These are presented next - one by one.

4.1.2.1 Plate mass

The influence of plate mass, m_{P}, on radiated sound power has already been discussed (Sec. 4.1). To reiterate: increasing plate mass leads to a decrease in sound power output (Fig. 4.1.3). This is the expected result.

4.1.2.2 Plate radius

The influence of plate radius was investigated for PMMA and radii of 1, 3, and 5 cm (Fig. 4.1.9a). As expected, larger piston radii lead to more sound power output for frequencies up to 2 kHz. Beyond 2 kHz, piston with larger radii emit less sound power than piston of smaller radii. The overall shape of the sound power curve is not influenced significantly by piston radius.

4.1.2.3 Plate material

In order to aid with the decision on plate material, three different materials - PMMA, aluminium and Teflon - were compared in terms of their sound power output. The assumption was made that the length of the piston and supporting rod measured 0.30 m. The piston mass was calculated using the density of the materials in question (Figs. 4.1.9b - 4.1.9c). It was also assumed that the piston and supporting rod are of the same material, which may not be the case in experiments. It can be seen that aluminium and Teflon display almost identical sound power output. PMMA emits approximately 2 dB more sound power than both aluminium and Teflon. The general behaviour of all three materials is very similar.

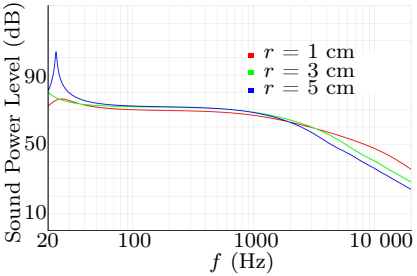

(a) Sound power output of a piston for different radii, r. Material: PMMA, length of piston and supporting rod, $l = 0.3$ m, $m_\mathrm{P} = \rho_\mathrm{PMMA} \pi r^2 l$.

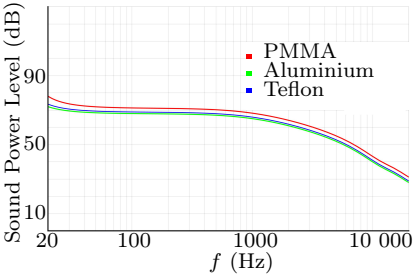

(b) Sound power output of a plate of radius 2 cm for three different materials, $\rho_\mathrm{PMMA} = 1.20 \cdot 10^3$ kg m^{-3}, $\rho_\mathrm{Alu} = 2.70 \cdot 10^3$ kg m^{-3}, $\rho_\mathrm{Teflon} = 2.16 \cdot 10^3$ kg m^{-3}.

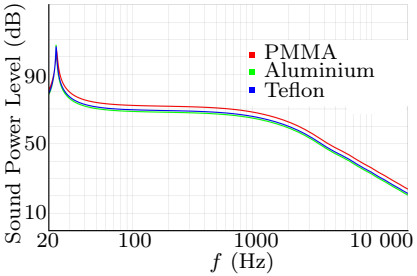

(c) Sound power output of a plate of radius 5 cm for three different materials, $\rho_\mathrm{PMMA} = 1.20 \cdot 10^3$ kg m^{-3}, $\rho_\mathrm{Alu} = 2.70 \cdot 10^3$ kg m^{-3}, $\rho_\mathrm{Teflon} = 2.16 \cdot 10^3$ kg m^{-3}.

Figure 4.1.9: Results on sound power level from variation of different parameters.

4.2 Near Field Effects

Having modelled the apparatus side of the measurement set-up, the shape of the expected sound emission was considered next. This was important so as to not develop a primary sound source solely with maximum sound power output in mind but to develop a primary sound source which would emit sound in such a way that sound pressure measurements could be performed with maximal accuracy. The near field and directivity of sound emission are important factors in these considerations (Sec. 2.1).

The sound power of a source is given as integral of the emitted sound intensity over an enveloping surface surrounding the source. In measurements in general and specifically in the measurements planned here, sound pressure rather than intensity was to be measured as these measurements are easier to carry out (Sec. 2.1). Using the approximation that the intensity is given as product of sound pressure and velocity, the sound power of a source can be calculated (Eq. 4.2.1). However, this approximation is only valid where sound pressure and velocity are in phase [8]. Hence, the near field is defined to be that part of the sound field where sound pressure and velocity are not in phase. Near fields for two variations will be described; a single monopole and a single dipole.

$$P = \int_S \vec{I} \ \mathrm{d}\vec{S} = \int_S p\vec{v} \ \mathrm{d}\vec{S} \tag{4.2.1}$$

4.2.1 Single monopole

Formulations for the sound pressure and radial component of velocity for a monopole are given (Eqs. 4.2.2 - 4.2.3) [17]. The angle between those two quantities describes the phase shift at different radii from the source (Eq. 4.2.4). In this work, this phase shift is defined as near field effect.

For frequencies below 10 Hz, the angle between sound pressure and velocity ranges from 70° to 90° (Fig. 4.2.1). Between 10 Hz and 100 Hz the phase shift drops significantly and measures – depending on the distance from the source – between 10° and 30°. Beyond 1 kHz the phase shift is below 5°. At a distance from the source of exactly one wavelength of the emitted sound in air the angle between sound pressure and velocity measures around 10°. Increasing the distance to two or three wavelengths decreases the phase

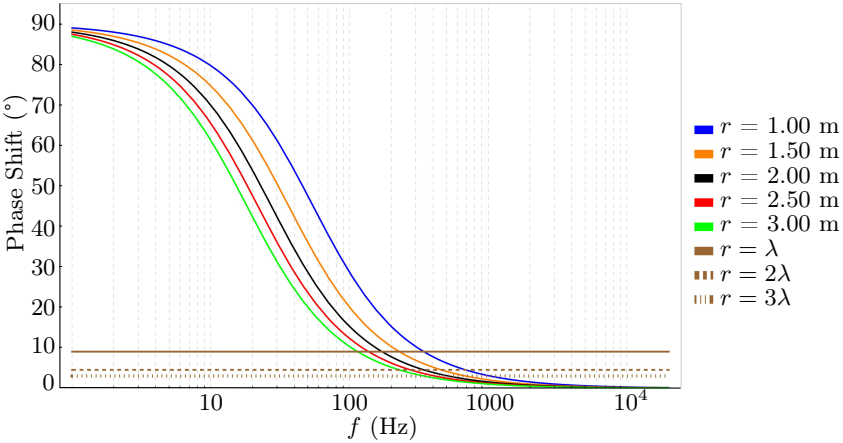

Figure 4.2.1: Near field effect for a single monopole.

shift to 5° and 4°, respectively.

$$p = \frac{\rho_0 c}{4\pi r}\hat{q}ke^{i\left(\omega t - kr + \frac{\pi}{2}\right)} \tag{4.2.2}$$

$$v_r = \frac{1}{4\pi r}\hat{q}k\sqrt{1+\frac{1}{(kr)^2}}\; e^{i\left(\omega t - kr + \frac{\pi}{2} - \arctan\left(\frac{1}{kr}\right)\right)} \tag{4.2.3}$$

$$\theta = -\arctan\left(\frac{1}{kr}\right) \tag{4.2.4}$$

The radial component of the intensity vector can be computed using the product of the pressure and velocity vector as described (Eq. 4.2.5) [17]. Inserting the corresponding equations from above leads to the specific monopole formulation (Eq. 4.2.6). Under consideration of the mathematical relation for the cosine of an inverse tangent function (Eq. 4.2.7), the radial component of the intensity vector can be readily computed (Eq. 4.2.8).

Closer inspection shows that this result is precisely the product of the RMS values of the pressure and radial component of velocity functions (Eq. 4.2.9). The significance of this observation is that the previously introduced

impedance error (Sec. 2.1.1.1) does not occur for monopole sources. It can be easily seen that the corresponding formula follows directly from the current result for the intensity vector (Eq. 2.1.12 - revisited below). This means that the enveloping surface method can be used at any distance from the source in order to calculate accurate sound power levels.

In the realm of this work that is significant as the desired goal was to develop a method that could determine sound power levels at frequencies below 100 Hz. In that frequency range, any in sound field measurements occur in the near field of the source. Hence, if sound power levels from the newly proposed out of sound field method presented in later parts of this work were to be compared to reference measurements from within the sound field, primary standards with monopole emission characteristics would allow for valid comparisons.

$$I_r = \frac{1}{2}\mathrm{Re}\left\{p v_r\right\} \tag{4.2.5}$$

$$I_r = \frac{1}{2}\rho_0 c \frac{\hat{q}^2 k^2}{(4\pi r)^2}\sqrt{1+\frac{1}{(kr)^2}}\mathrm{Re}\left\{e^{i\arctan\left(\frac{1}{kr}\right)}\right\} \tag{4.2.6}$$

$$\cos\left(\arctan\left(\frac{1}{kr}\right)\right) = \frac{1}{\sqrt{1+\frac{1}{(k}r)^2}} \tag{4.2.7}$$

$$I_r = \frac{1}{2}\rho_0 c \frac{\hat{q}^2 k^2}{(4\pi r)^2} \tag{4.2.8}$$

$$I_r = \tilde{p}\tilde{v_r} \tag{4.2.9}$$

$$\tilde{p}\tilde{v}\cos(\tilde{p},\tilde{v}) = \frac{1}{\rho_0 c}\tilde{p}^2 \tag{2.1.12 revisited}$$

In the previous discussion, the validity of the cosine of inverse tangent formulation was postulated from a mathematical point of view (Eq. 4.2.7). The physical correspondence is given by an inspection of the specific acoustic impedance, Z_{sai}, of the air volume that the source emits sound into (Eq. 4.2.10) [8]. After a series of mathematical transformations (Eqs. 4.2.11 - 4.2.14), it can be seen that the angle between the imaginary and real part of the specific acoustic impedance is precisely the opposite of the angle between the sound pressure and radial component of velocity (Eq. 4.2.15 vs. Eq. 4.2.4). Thus, the angles compensate, which provides the

physical reason for the usability of pressure measurements for sound power determination at all distances from the source as shown in the previous discussion.

$$Z_{\text{sai}} = \frac{\rho_0 c}{1 + \frac{1}{ikr}} \tag{4.2.10}$$

$$= \rho_0 c \frac{ikr}{1 + ikr} \qquad | \cdot \frac{1 - ikr}{1 - ikr} \tag{4.2.11}$$

$$= \frac{\rho_0 c}{1 + (kr)^2} \left((kr)^2 + ikr \right) \tag{4.2.12}$$

$$\tan \theta_{\text{sai}} = \frac{|\text{Im}\{Z_{\text{sai}}\}|}{|\text{Re}\{Z_{\text{sai}}\}|} \tag{4.2.13}$$

$$= \frac{1}{kr} \tag{4.2.14}$$

$$\theta_{\text{sai}} = \arctan\left(\frac{1}{kr}\right) \tag{4.2.15}$$

4.2.2 Single dipole

In case that the developed primary standards would not act like monopole sources, the characteristics of dipole sources need to be elaborated, as well. The sound pressure and radial component of velocity of a single dipole are given (Eqs. 4.2.16 - 4.2.17) [17]. Following the same calculations as before, the phase shift at different radii can be calculated (Eq. 4.2.18).

Graphic analysis shows that this means that for a single dipole, sound pressure and velocity are 90° out of phase at 1 Hz (Fig. 4.2.2). At one point between 10 Hz and 100 Hz – the exact frequency depends on the distance from the source – sound pressure and velocity are exactly in phase. Beyond 100 Hz the phase angle increases and past 1 kHz sound pressure and velocity are of almost exactly opposite phase. Maintaining a distance of exactly one, two or three wavelengths leads to phase shifts of approximately 150°, 165° and 170°, respectively.

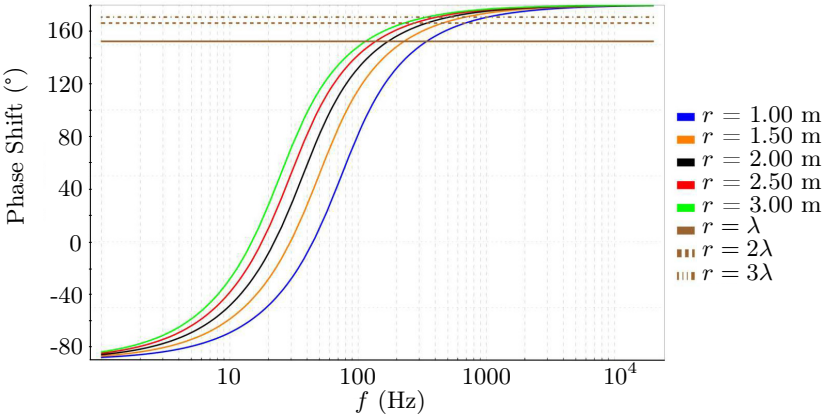

Figure 4.2.2: Near Field Effect for a single dipole.

$$p = \frac{\rho_0 c}{4\pi r}\cos(\theta)\cdot d\cdot\hat{q}\cdot k^2\sqrt{1+\frac{1}{(kr)^2}}e^{i(\omega t-kr-\arctan(\frac{1}{kr})+\pi)} \tag{4.2.16}$$

$$v_r = \frac{\cos(\theta)}{4\pi r}d\cdot\hat{q}\cdot k^2\sqrt{1+\frac{4}{(kr)^4}}e^{i(\omega t-kr+\frac{\pi}{2}+\arctan(\frac{kr}{2}-\frac{1}{kr}))} \tag{4.2.17}$$

$$\theta = \frac{\pi}{2}-\arctan(\frac{1}{kr})+\arctan(\frac{kr}{2}-\frac{1}{kr}) \tag{4.2.18}$$

It was shown that for a single monopole the formulation $I_r = \tilde{p}\tilde{v_r}$ holds at all distances from the source (Sec. 4.2.1). For a single dipole however, one obtains a different solution (Eq. 4.2.19) [17]. Thus, the error Δ in estimating sound intensity levels from sound pressure measurements must be evaluated (Eq. 4.2.20). Depicting Δ graphically shows that the error in calculating the sound intensity level from pressure measurements is significant for frequencies up to approximately 100 Hz (Fig. 4.2.3). This also follows from the analytical equation as for $f \to \infty$, $\Delta \to 10\log_{10}(1) = 0$ (Eq. 4.2.20).

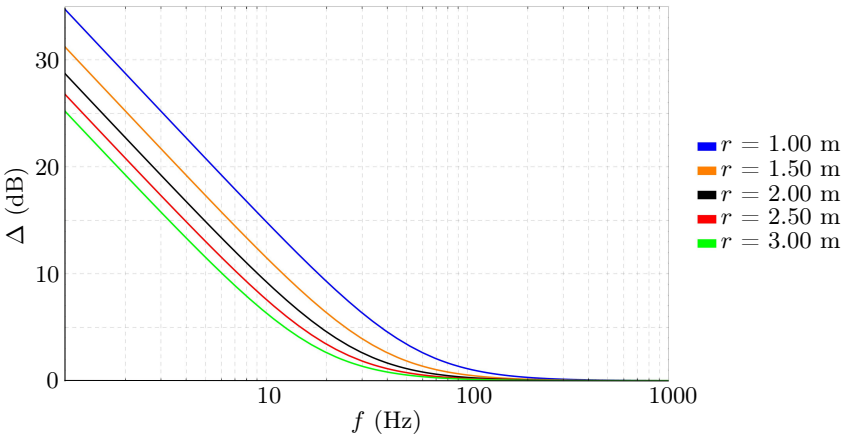

Figure 4.2.3: Dependence of error Δ on distance from the source and frequency.

$$I_\epsilon = \frac{\rho_0 c}{(4\pi r)^2} \cos^2(\theta) d^2 \hat{q}^2 k^4 \left(1 + \frac{1}{(kr)^2}\right) = I_r \left(1 + \frac{1}{(kr)^2}\right) \quad (4.2.19)$$

$$\Delta = 10 \log_{10} \left(1 + \frac{1}{(kr)^2}\right) \quad (4.2.20)$$

4.3 Directivity of the Primary Source

The directivity of sound emission is an important factor when comparing laser-vibrometer measurements with sound pressure measurements. The more uniform sound emission is, the more independent its sound pressure output is from the angle to the source. Conversely, for a sound source with very directed output, microphone placement in the sound field has to be done with a lot of care. Here, the directivity factor, Γ, was used to describe the dependence of sound pressure on the direction from the sound source in the free field. It is formally defined as the fraction of sound pressure in a specific direction over sound pressure in a reference direction; both to be taken in the far field at constant distance, R (Eq.

4.3.1) [10]. Underlined quantities are complex. This can be converted into the directivity measure in dB (Eq. 4.3.2). For the case of a rigid baffled piston, the directivity factor is given (Eq. 4.3.3), where J_1 denotes the Bessel function of the first kind, α is the angle between the z-axis and the point of interest, β is the polar angle in the x-y plane, r is the radius of the piston and k the wave number [10].

$$\Gamma(\alpha,\beta) = \frac{\underline{p}(\alpha,\beta,r)}{\underline{p}(\alpha_0,\beta_0,r)} \quad \text{, for } kr \gg 1 \tag{4.3.1}$$

$$D = 10\log_{10}(\underline{\Gamma} * \text{Conjugate}(\underline{\Gamma})) \tag{4.3.2}$$

$$\underline{\Gamma} = \frac{2J_1(kr\sin(\alpha))}{kr\sin(\alpha)} \tag{4.3.3}$$

The directivity factor in dB (Eq. 4.3.2) was plotted under the assumption that tonal excitation was used (Figs. 4.3.1 - 4.3.2). As mentioned, this measure only holds in the far field. This means that results have to be considered with care for low frequencies. However, for low frequencies sound emission appears to be uniform (Fig.4.3.2). Thus, directivity considerations need only be made for larger frequencies. For these far field measurements can be made. It is observable that for a plate of radius $r = 1$ cm, sound emission is almost entirely uniform whereas for a plate of radius $r = 2$ cm at a frequency of $f = 8$ kHz, sound emission along the vertical axis is approximately 12 dB higher than along the horizontal plane (Fig. 4.3.1a).

For a plate of radius 2 cm at a frequency of 16 kHz, one can also observe that at an angle of approximately 45° almost no sound power is detected as there is destructive interference of sound pressure and velocity at that angle. This leads to the formation of "lobes". The larger the radius, the more "lobes" exist. This means that the number of angles leading to destructive interference increases (Fig. 4.3.1a). Measurements of sound pressure on enveloping surfaces should avoid these angles.

Considering that one plate may not have been able to adequately cover the entire range of 20 Hz – 20 kHz, the use of a plate with larger radius was investigated for frequencies up to 4 kHz. Looking at the directivity measure shows that even a plate of radius $r = 5$ cm produces approximately 30 dB more sound pressure along the vertical than the horizontal axis at 4 kHz (Fig. 4.3.1b). In comparison, a 4 cm plate shows only about 12 dB of

that directivity.

Focusing on specific radii and investigating the directivity of sound emission at varying frequencies confirms previous results (Fig. 4.3.2). A plate of 1 cm in radius displays almost uniform emission up to 16 kHz. Plates with radii larger than 2 cm feature sound emission that is very directed in the z-axis direction for frequencies larger than 8 kHz. The use of such plates at higher frequencies needs to take emission directivities into account. While a set limit in directivity would be meaningful for experiments, no such limit is proposed here as practicability of any standard needs to be evaluated on a case by case basis.

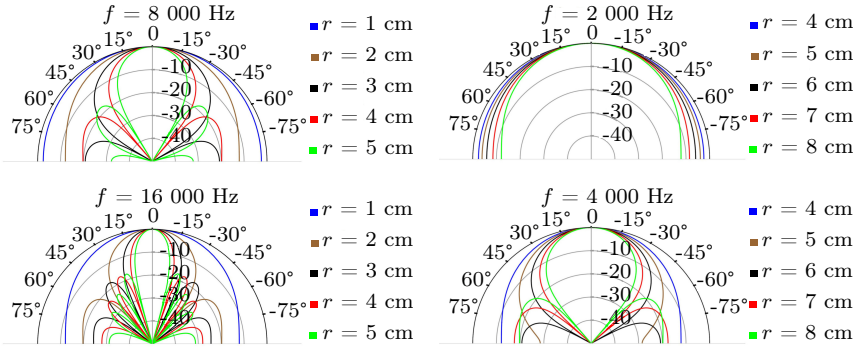

(a) Piston radii of 1 to 5 cm.

(b) Piston radii of 4 to 8 cm.

Figure 4.3.1: Directivity measure, D, of the primary source comparing the performance of different piston radii, r, at set frequencies. Radial axis in [dB].

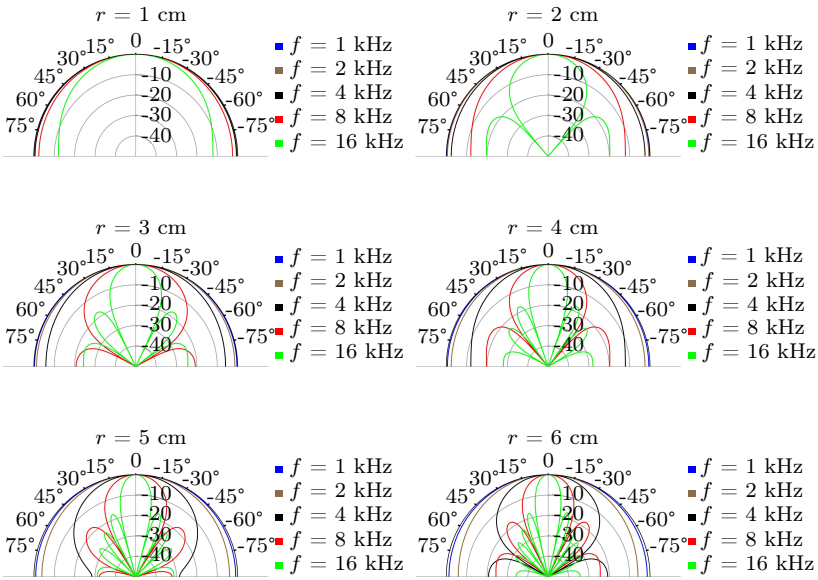

Figure 4.3.2: Directivity measure, D, of the primary source for piston radii of 1 to 6 cm at different frequencies. Radial axis in [dB].

4.3.1 Directivity of sound emission of Source 6

Source 6 was the only source which featured a piston that was made of more than one material; namely it had a central part made of aluminium to which a silicone sealing was affixed (Fig. 3.3.1c). Considering this speciality, the first question of interest to be discussed was whether its experimentally determined directivity would be equivalent to the analytical data of piston sources presented above. For the analytical calculations (Eq. 4.3.2), the piston radius was assumed as $r = 2.8$ cm. This corresponded to the aluminium part of the piston. As previous results showed that the aluminium part of the piston is the major contributor to the sound power output (Fig. 3.3.3a), the silicone sealing was excluded. In the experimental data, both the silicone sealing as well as the aluminium centre part contribute to the measured directivity. Hence, large deviations between experimental and analytical results would indicate that the silicone sealing significantly influences the directivity of sound emission and that previous

assumptions would have to be discarded.

However, results indicate that the analytical model fits the measurement data well. Up to 1.25 kHz, sound emission is uniform and no differences between experimental and analytical data notable (Fig. 4.3.3a). Sound emission is approximately 1 dB larger in the 90° than in the 0° direction at 2.5 kHz and there are small differences between analytical and measurement results (Fig. 4.3.3b). With increasing frequencies, the differences between both methods also become larger. However, both analytical as well as experimental data display the same general behaviour (Fig. 4.3.3c). At 10 kHz the formation of lobes begins (Fig. 4.3.3d). While the general behaviour of the analytical and experimental data graphs is still similar, the absolute difference between the results of the two methods becomes significant. This indicates an influence of the silicone sealing, which shows largely subdivided motions at these frequencies (Fig. 5.2.16c). The analytical model, of course, cannot accommodate for this behaviour. However, it is satisfactory to observe that both analytical as well as measurement data agree in their qualitative description of sound emission, even if there are quantitative differences between both methods. This shows that even the multi-material Source 6 conforms to expected piston behaviours and that the results presented in this chapter are applicable even to that source [36].

4.4 Numerical Modelling

The previous results on directivity indicated that circular piston sources show uniform sound emission at low frequencies, i.e. that they act like monopole sources (Sec. 4.3). However, the directivity factor that was used to obtain this indication is formally defined only for the far-field. At low frequencies, room dimensions limit the in-sound-field measurement possibilities to the near-field, though. For this reason, the preceding discussion on the near field of monopole sources (Sec. 4.2) reasoned the desire for primary standards with that characteristic: namely, that the enveloping surface method for sound power determination (Sec. 2.1.1) produces valid results at any distance from such a source. In order to compare sound power levels obtained by the discretised Rayleigh integral method to those that currently standardised methods return, this would be a crucial factor. Hence, monopole-like sound emission of primary standards was an important goal.

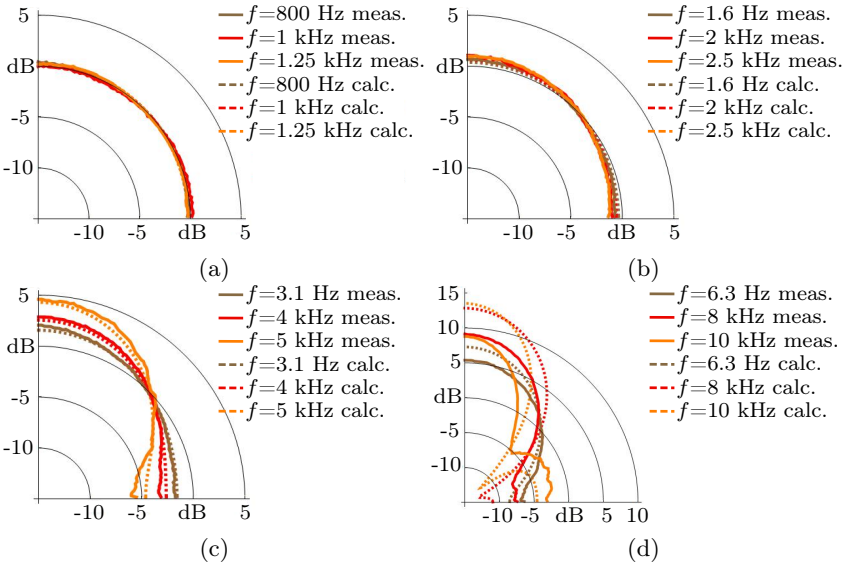

Figure 4.3.3: Directivity, D, of sound emission for different frequencies (from [36]). Measured values obtained from Source 6.

As the far-field limitations of the analytical studies impeded a formal conclusion on the sound emission of the primary standards, numerical simulations using the commercial software COMSOL were performed. The goal was to try and validate that the physical sound sources really act like monopoles at low frequencies. To do so, the sound power output of an assumed monopole source - the rigid piston - was modelled first. The thusly obtained values were compared to analytical formulations for monopole source in order to verify the assumption that a rigid piston truly is a source with that characteristic. With this verification in place, the model could be fed with actual measurement data. The resulting sound power output was compared to the previously determined monopole sound power levels. This allowed for conclusions on the near field characteristics of the real sound sources.

4.4.1 Rigid piston in a free sound field

Initially then, the focus was on the sound field radiated by a rigid baffled piston into a free field. Aspects of interest were possible near field effects as well as directivity of sound emission. Throughout the numerical studies, the piston was assumed to have a radius of $r = 0.0495$ m. Based on the assumption that sound emission of a centrally excited rigid piston is symmetric with respect to the z-axis, computational efficiency was increased by only modelling a 10 degree slice of the hemisphere of interest. Still, the minimal discretisation needed for accurate results (approximately 6 points per wavelength) was only attainable for frequencies up to 500 Hz.

4.4.1.1 Calculation of sound power level from intensity vs. pressure measurements

The question of interest in this first investigation was whether or not the rigid piston truly behaved like a monopole at low frequencies in terms of sound emission. If so, calculation of sound power levels from pressure measurements (Eq. 4.4.1) would yield the same results as calculation from sound intensity measurements (Eq. 4.4.2) as described previously (Sec. 4.2). The values from the numerical model were compared to analytic data (Eqs. 4.1.3 (revisited below) - 4.4.3) that was introduced before (Sec. 4.1). This analysis was performed for three surfaces with distances, d_S, from the source of 0.5 m, 1.0 m and 3.0 m, respectively.

$$P_p = \frac{1}{\rho_0 c} \int p^2 \mathrm{d}S \tag{4.4.1}$$

$$P_I = \int I_n \mathrm{d}S \tag{4.4.2}$$

$$P_\mathrm{a} = \rho_0 c \pi r^2 v^2 \left[1 - \frac{J_1(2kr)}{kr}\right] \tag{4.1.3 revisited}$$

$$\Delta L_{\mathrm{W}_{p/I}} = 10 \log_{10} \frac{P_{p/I}}{P_\mathrm{a}} \text{ dB} \tag{4.4.3}$$

For smaller distances from the source - $d_\mathrm{S} \leq 1.0$m - one can see that both intensity and pressure measurements yield the same sound power levels (Fig. 4.4.1a). Moreover, the investigation model chosen was that of a monopole. The excellent agreement of the results suggests that this model is accurate for a rigid piston at low frequencies. For $d_\mathrm{S} = 3.0$ m, it is observable that the difference in calculated sound power levels starts to deviate above 200 Hz. This can be explained by the inaccuracy of the computational mesh for those frequencies. Plotting the sound pressure levels for a frequency of 500 Hz confirms the monopole-like behaviour of the ideal piston (Fig. 4.4.1b).

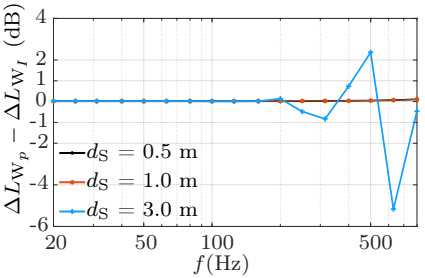

(a) Difference in sound power level, L_W, calculated from sound pressure or sound intensity values for different distances from the source, d_S.

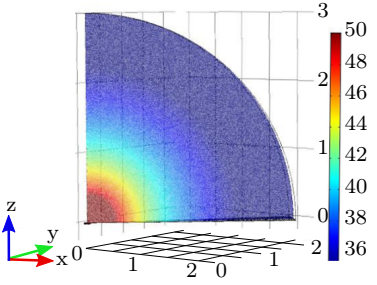

(b) Sound pressure level for $f = 500$ Hz. Piston radius $r = 0.0192$ m.

Figure 4.4.1: Results for sound power levels calculated from either intensity or pressure data.

4.4.1.2 Calculation of Directivites

As before, only frequencies up to 500 Hz were investigated. The analytical calculation of directivities was presented previously (Sec. 4.3). Thus, the goal here was to display the correlation of numerical data with the analytical results focusing on frequencies below 500 Hz. The comparison was accomplished by use of the directivity factor (Eqs. 4.3.1 - 4.3.2). Reference direction for the directivity factor, Γ, was the z-axis. The results show that the numerical and analytical solutions are very close to identical (Fig. 4.4.2).

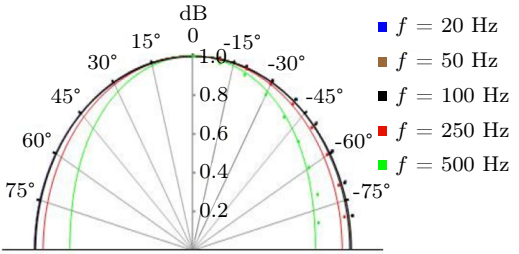

Figure 4.4.2: Directivity measure, D, of the primary source at a distance of $d_S = 0.5$ m in dB. Dots indicate the numerical and lines the analytical solution (from [38]).

4.4.1.3 Near Field Effects

As a reminder, the near field was defined as that area where sound pressure and velocity are not in phase (Sec. 4.2). Here, the phase angle from the numerical data was calculated and compared to the reference angle obtained from the analytical calculation (Eq. 4.2.4). This analysis was performed for three distances from the source, d_S, and three radial angles, α, where α indicates the angle with respect to the x – y plane. Again, one can observe that the theoretical values for a monopole are fitted very well by the numerical data (Tbls. 4.4.1 - 4.4.3).

The joint results from the numerical study confirm the proposition that a rigid piston in a free sound field acts like a monopole source at low frequencies.

Table 4.4.1: Difference between numerical and analytical solution (Eq. 4.2.4) to phase angle between sound pressure and velocity for $d_S = 0.50$ m in degree.

Frequency (Hz)	$\alpha = \mathbf{30}^\circ$	$\alpha = \mathbf{50}^\circ$	$\alpha = \mathbf{70}^\circ$
20	0.07	0.06	0.04
25	0.09	0.07	0.05
31	0.35	0.33	0.30
40	0.14	0.11	0.05
50	0.17	0.14	0.03
63	0.20	0.18	-0.01
80	0.24	0.22	-0.10
100	0.28	0.27	-0.24
125	0.32	0.33	-0.45
160	0.38	0.42	-0.78
200	0.43	0.52	-1.17
250	0.48	0.64	-1.66
315	0.54	0.80	-2.28
400	0.57	1.02	-3.10
500	0.50	1.25	-4.09
630	0.32	1.56	-5.55
800	-0.04	2.15	-6.84

Table 4.4.2: Difference between numerical and analytical solution (Eq. 4.2.4) to phase angle between sound pressure and velocity for $d_S = 1.0$ m in degree.

Frequency (Hz)	$\alpha = \mathbf{30^\circ}$	$\alpha = \mathbf{50^\circ}$	$\alpha = \mathbf{70^\circ}$
20	0.13	0.12	0.12
25	0.15	0.15	0.14
31	0.57	0.56	0.55
40	0.19	0.18	0.18
50	0.21	0.19	0.19
63	0.21	0.20	0.19
80	0.21	0.19	0.18
100	0.21	0.18	0.17
125	0.20	0.17	0.16
160	0.20	0.15	0.14
200	0.21	0.14	0.13
250	0.24	0.14	0.12
315	0.30	0.14	0.10
400	0.41	0.14	0.06
500	0.62	0.15	-0.04
630	0.93	0.12	-0.22
800	1.44	-0.05	-1.14

Table 4.4.3: Difference between numerical and analytical solution (Eq. 4.2.4) to phase angle between sound pressure and velocity for $d_S = 3.0$ m in degree.

Frequency (Hz)	$\alpha = \mathbf{30^\circ}$	$\alpha = \mathbf{50^\circ}$	$\alpha = \mathbf{70^\circ}$
20	0.20	0.20	0.20
25	0.19	0.19	0.19
31	0.57	0.57	0.58
40	0.16	0.15	0.17
50	0.14	0.13	0.15
63	0.12	0.11	0.14
80	0.11	0.09	0.12
100	0.09	0.07	0.11
125	0.09	0.06	0.10
160	0.08	0.03	0.07
200	0.07	0.00	0.03
250	0.06	-0.05	-0.08
315	0.03	-0.15	-0.30
400	-0.03	-0.36	-0.78
500	-0.16	-0.74	-1.65
630	-0.42	-1.46	-3.36
800	-0.97	-2.83	-6.47

4.4.2 Real source in a free sound field

To test the real sources against the same monopole assumption, measurement data were fed into the numerical model. They were obtained from measurements in a hemianechoic room (Sec. 3.1.1) using PTB's Source 3 (Fig. 3.3.1b). This source featured an aluminium piston of radius $r = 0.0192$ m. The assembly was embedded into the floor such that the piston surface was flush with the surrounding brass plate of the hemianechoic room floor. The laser scanning vibrometer measured 563 points - 37 on the piston surface, 132 on the aluminium ring, and 394 on the room floor (Fig. 4.4.3). The excitation signal used was a multi-sine whose FFT frequency resolution was of 3.125 Hz (no window). Frequencies measured ranged from 3.125 Hz to 20 kHz.

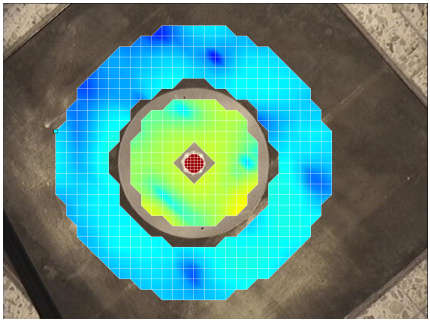

Figure 4.4.3: Measurement grid scanned by the laservibrometer including points on the piston (dark red), points on the aluminium ring (yellow-green) and points on the surrounding room floor (blue).

4.4.2.1 Calculation of sound power level from intensity vs. pressure measurements

The numerical model developed in COMSOL consisted of an aluminium piston of radius $r = 0.0192$ m which was to emit sound into a hemisphere of radius $R = 3.0$ m filled with air. The movement of the piston was modelled after the measurement data from just the piston surface. Thus, for the 37 measurement points on the piston surface, the experimentally determined velocity was prescribed in COMSOL for precisely those 37 points and the

specific frequencies of interest. Numerical data were obtained for frequencies up to 300 Hz with the model run in 3D. Data collected were intensity (RMS), sound pressure level, pressure, and velocity along meridional arcs of radii ranging from 0.5 m to 3.0 m in steps of 0.5 m for two different probe sets:

Probe Set 1
Angles α (with respect to the z-axis): 3°, 9°, 16°, 23°, 30°, 37°, 46°, 56°, 66°, and 90°.
Angles β (with respect to the x-y plane): 0°, 60°, 120°, 180°, 240°, and 300°.
→ Total number of probe points: 60

Probe Set 2
Angles α (with respect to the z-axis): 0° to 90° increasing by 1.5° for every step.
Fixed angle β (with respect to the x-y plane): 0°.
→ Total number of probe points: 61

Analogous to the analysis for the rigid piston in an ideal sound field, the following three questions were investigated:

1. Does sound power level calculated from intensity data equal sound power level obtained from pressure data?
2. Is sound emission uniform?
3. Is there a near-field effect?

The comparison of calculations of sound power level from intensity and pressure data shows that the results correspond reasonably well (Tbls. 4.4.4 - 4.4.5). There seems to be no influence of angle β on the results conforming to the symmetry of sound emission assumption. Moreover, the discretisation chosen for probe set 1 - which corresponded to the measurement set-up employed at PTB at the time – seems sufficient as an increase in measurement points modelled by probe set 2 yielded the same results as probe set 1.

However, a difference of approximately 1 dB is visible between the numerical data obtained from COMSOL and the analytical calculations. The results for the rigid piston were obtained by averaging the 37 velocities

measured with the laser scanning vibrometer on the piston surface. Hence, the difference between the rigid piston and Rayleigh sound power most likely stems from the piston not moving perfectly rigidly.

The difference of 1 dB between the numerical data and the analytical data is less easily explained. All evaluation methods assumed sound radiation into a perfect free field. Hence, they should all coincide. The systematic difference of 1 dB between the numerical COMSOL results and the analytical calculations indicates that COMSOL cannot be used for the description of sound power without further ado. The observed systematic difference is larger than the desired overall uncertainty for the primary standard of 0.5 dB. Thus, sound power determination with numerical methods would require more detailed investigations on the source of the 1 dB difference.

Table 4.4.4: Sound power levels, L_W, from probe set 1 in comparison to analytically calculated sound power levels.

f **(Hz)**	L_W **from num. pressure data (dB)**	**Diff. to** L_W **from num. intensity data (dB)**	**Diff. to** L_W **of rigid piston (dB)**	**Diff. to** L_W **from Rayleigh's integral (dB)**
50	14.91	0.02	-0.89	-1.17
75	19.86	0.02	-0.91	-1.17
100	19.38	0.02	-0.93	-1.17
200	21.42	0.02	-0.87	-1.16
300	22.85	0.03	-0.91	-1.17

4.4.2.2 Calculation of Directivites

To test the uniformity of sound emission, the directivity measure (Eq. 4.3.2) for probe set 2 was calculated. It confirms that sound emission is very uniform and corresponds well with the behaviour of a monopole (Fig. 4.4.4).

4.4.2.3 Near Field Effects

The analysis on near field effects was carried out for probe set 2 at the six different distances from the source. The phase angle from the numerical

Table 4.4.5: Sound power levels, L_W, from probe set 2 in comparison to analytically calculated sound power levels.

f (Hz)	L_W from num. pressure data (dB)	Diff. to L_W from num. intensity data (dB)	Diff. to L_W of rigid piston (dB)	Diff. to L_W from Rayleigh's integral (dB)
50	14.91	0.02	-0.89	-1.17
75	19.86	0.02	-0.91	-1.17
100	19.38	0.02	-0.93	-1.17
200	21.42	0.02	-0.87	-1.16
300	22.85	0.03	-0.91	-1.17

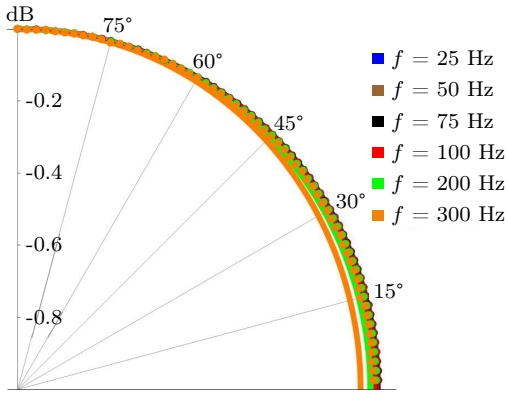

Figure 4.4.4: Directivity measure, D, of probe set 2 compared to theoretical values for a monopole (Eq. 4.3.3). Lines show analytical data for a monopole, dots numerical data of probe set 2.

data for velocity and pressure was calculated and compared to the theoretical angle for a monopole (Eq. 4.2.4).

It can be seen that the absolute value of the difference between the numerical and theoretical value stays below 0.4° for the investigated frequency range, with the largest differences occurring for the largest frequency observed - 300 Hz (Fig. 4.4.5). That trend could be due to insufficiencies in

the mesh for higher frequencies and/or sound emission being not entirely uniform for that frequency any more.

Nevertheless, an absolute deviation of less than 0.4° together with the previous results confirms that the circular pistons used for this work behave like monopole sources at low frequencies. So, pressure measurements in the context of the enveloping surface method can be used to determine the sound power output of the primary standards presented in this work also under near field conditions. These sound power levels from in-sound-field measurements will later be utilised for a comparison to those sound power levels that the discretised Rayleigh integral produced (Chp. 7). The results of this chapter show that their lower frequency limit of comparability was determined by the "cut-on" frequency of the room only and not by the measurement method. For the specific case here, this was at a frequency of $f = 100$ Hz (Sec. 3.1).

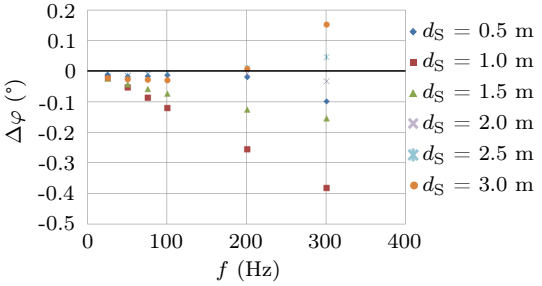

Figure 4.4.5: Difference between phase angles of velocity and pressure for numerical data from the real source and analytical values for a monopole.

5 | Sound Power Determination and Minimal Discretisation

In the experimental set-up investigated here, the circular piston is excited at its centre point. This excitation originates from an electrodynamic shaker to which an iron rod is attached. This iron rod is attached to the centre point of the piston. However, its diameter is significantly smaller than that of the piston. This means that the motion of the piston originates at its centre point, from where it spreads radially outward over the whole piston surface leading to the assumption of piston movement that is point symmetric with respect to its centre point. This process is governed by mass inertia. Hence, the movement of the piston surface can be described by the following three phases:

1. The piston moves uniformly with rigid surface (low frequency range)
2. The piston surface displays an Eigenmode
3. Neither of the above: The piston surface moves subdividedly with no distinct pattern

The sound power output of the piston is to be determined for each one of the three phases. This chapter introduces the methods used to do so and discusses the aspect of required discretisations that assure a desired accuracy of the determined sound power levels.

5.1 Ideal Pistons - Analytical Calculation of Sound Power

For the case of an ideal rigid circular piston an analytical solution for its emitted sound power exists (Eq. 5.1.1) [8]. With the notation used as follows, the sound power output of this ideal scenario can be calculated (Fig. 5.1.1).

- ρ - density of medium into which sound is emitted
- c - speed of sound in medium

- v_0 - constant surface velocity of the piston
- r - radius of the piston
- J_1 - Bessel function of the first kind

$$P_{\text{rigid}} = \rho c \cdot v_0^2 \cdot \pi r^2 \left[1 - \frac{J_1(2kr)}{kr}\right] \tag{5.1.1}$$

In the experimental set-up investigated here, ideal rigid movement of the piston could only be expected in the low frequency range. This is due to the piston radius being significantly larger than the radius of the rod by which it was attached to the shaker. Hence, this analytical solution could only yield relevant results in the low frequency range. For specific cases of interest, an estimation on the frequency range for which the analytical solution would be valid could be obtained from a calculation of the first Eigenmode frequency. The limit of validity would be before the first Eigenmode. If it were of interest, a more specific frequency range could be found by measuring different points on the piston surface and analysing differences in movement velocities or displacements between the different measurement points. However, as the analytical solution only covers the ideal case of a perfectly rigid piston, it is not suitable for the calculation of the real piston's sound power output in the entire frequency range of interest (20 Hz - 20 kHz). The discretised Rayleigh integral will be used for this aim instead.

5.2 Discretised Rayleigh Integral

The discretised Rayleigh integral was derived and introduced by Hübner under the name direct finite element method [16]. Since then, the method has been extended from planar radiators [33] to three dimensional sources of any shape [12][28]. Detailed descriptions of the derivation and underlying assumptions can be found in the literature (in particular [12] and [16]). Hence, only a short summary of the principle of the discretised Rayleigh integral will be given here.

An arbitrary three dimensional surface that envelops a collection of individual sound sources is considered. Under the assumption that there is

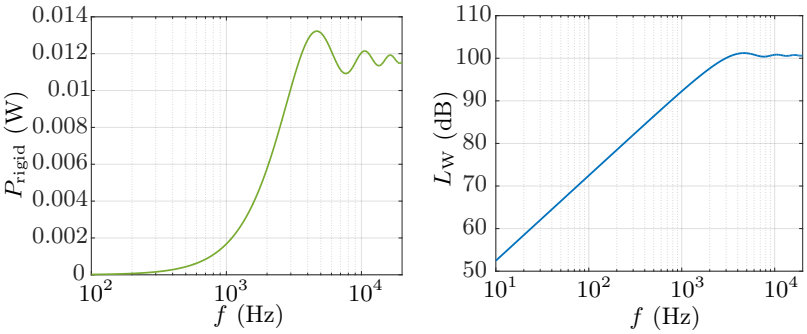

(a) Sound power

(b) Sound power level

Figure 5.1.1: Sound power and sound power level for an ideal rigid piston (Eq. 5.1.1). Parameter values used: $c = 343$ m/s, $r = 0.03$ m, $\rho = 1.2041$ kg/m^3, $v_0 = 0.1$ m/s.

no energy loss in the gaseous medium due to dissipation, the total sound power that is emitted by this collection of sources can be found through integration of the normal component of the total sound intensity produced by the entire collection of sources on said enveloping surface (Fig. 5.2.1) [28].

This normal component of sound intensity is given by the time averaged product of the total sound pressure and normal component of particle velocity at every point of the enveloping surface chosen (Eq. 5.2.1). However, the total sound pressure is just the sum of the individual sound pressure contributions of all sources within the enclosed volume. The same holds true for the sound velocity (Eq. 5.2.2). Rearrangement of the terms shows that, in fact, the normal component of sound intensity at each point of the enveloping surface is given by the sum of the individual contributions of each individual point of the collection of sound sources as well as the sum of the interaction terms between the individual points of the collection (Eq. 5.2.3 - 5.2.4).

By extension, the same is true for the total sound power: It is given as sum of the sound power emitted by each individual source in absence of all other sources, P_i, and the sum of the interaction of each sound source with all other sound sources, P_{ij} (Eq. 5.2.5) [28].

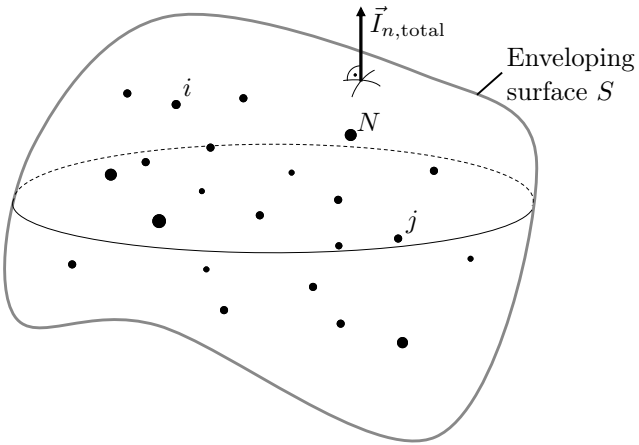

Figure 5.2.1: Schematic of sound power determination of a collection of N sound sources by integration over an enveloping surface (adapted from [28]).

$$I_{n,\text{total}} = \overline{p_{\text{total}} \cdot v_{n,\text{total}}}^{t} \tag{5.2.1}$$

$$I_{n,\text{total}} = \\ = \overline{(p_1 + p_2 + p_3 + ... + p_N)(v_{n,1} + v_{n,2} + v_{n,3} + ... + v_{n,N})}^{t} \tag{5.2.2}$$

$$I_{n,\text{total}} = \sum_{i=1}^{N} \overline{p_i v_{n,i}}^{t} + \sum_{i=1}^{N} \sum_{\substack{j=1 \\ i \neq j}}^{N} \overline{p_i v_{n,j}}^{t} \tag{5.2.3}$$

$$I_{n,\text{total}} = \sum_{i=1}^{N} I_{n,i} + \sum_{i=1}^{N} \sum_{\substack{j=1 \\ i \neq j}}^{N} I_{n,ij} \tag{5.2.4}$$

$$P_{\text{total}} = \sum_{i=1}^{N} P_i + \sum_{i=1}^{N} \sum_{\substack{j=1 \\ i \neq j}}^{N} P_{ij} \tag{5.2.5}$$

In the specific experimental set-up considered throughout this work, the individual sound power sources are assumed to be monopole sources located on the surface of a planar piston which undergoes harmonic motion. Sound emission occurs into the hemisphere above the piston surface (Fig. 5.2.2). Under these assumptions, the Rayleigh integral is applicable and the sound power contribution of each monopole source, P_i, as well as the interaction terms, P_{ij}, are known (Eqs. 5.2.6 - 5.2.7) [18]. Similarly, the flux, $\hat{q}_i$, can be expressed in terms of the measurement quantities movement velocity, $\hat{v}_i$, and corresponding surface area, S_i (Eq. 5.2.8). Thus, the discretised Rayleigh integral as applicable to this work can be established (Eq. 2.3.1 - repeated below) [18].

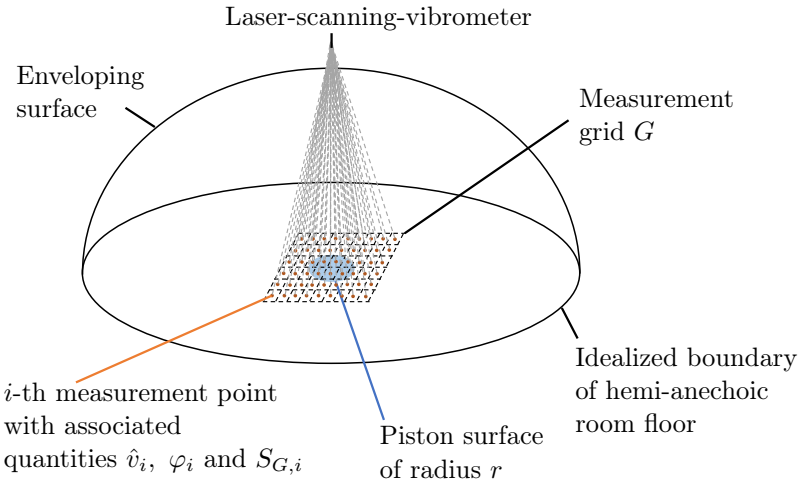

Figure 5.2.2: Schematic of measurement set-up. The piston surface as well as parts of the surrounding baffle are discretised and desired quantities measured by a laser-scanning vibrometer.

The notation used is as follows:

- ρ - mean density of the gaseous medium (here: air)
- c - speed of sound in the medium (here: air)
- k - wave number
- $\hat{q}_i$ - amplitude of the sound energy flux of the i-th monopole

- d_{ij} - linear distance between the i-th and j-th monopole source
- ϕ_i - phase of the sound flux of the i-th monopole
- $\hat{v}_i$ - amplitude of movement velocity of the i-th monopole
- $\tilde{v}_i$ - RMS value of the movement velocity of the i-th monopole
- S_i - surface area covered by the i-th monopole

$$P_i = \frac{\rho_0 c}{2\pi} \cdot k^2 \cdot \frac{\hat{q}_i^2}{2} \tag{5.2.6}$$

$$P_{ij} = \frac{\rho_0 c}{2\pi} \cdot k^2 \cdot \frac{\hat{q}_i \hat{q}_j}{2} \cdot \frac{\sin(kd_{ij})}{kd_{ij}} \cos(\phi_i - \phi_j) \tag{5.2.7}$$

$$\hat{q}_i = \hat{v}_i S_i \tag{5.2.8}$$

$$\begin{aligned} P_{\text{Rayleigh}} = &\sum_{i=1}^{N} \frac{\rho_0 c}{2\pi} k^2 \tilde{v_i}^2 S_i^2 + \\ &+ \sum_{i=1}^{N} \sum_{\substack{j=1 \\ i \neq j}}^{N} \frac{\rho_0 c}{2\pi} k^2 \tilde{v_i} \tilde{v_j} S_i S_j \frac{\sin(kd_{ij})}{kd_{ij}} \cos(\phi_i - \phi_j) \end{aligned} \tag{2.3.1 revisited}$$

It was shown that the sound power determined with this method is equal to the sound power obtained from the integral form of the Rayleigh integral for all types of planar radiators [18]. Thus, the integral and discretised form of the Rayleigh integral are equivalent and, hence, the validity of the discretised Rayleigh integral established for the specific case of the piston-shaker set-up investigated here. Moreover, the only boundary condition imposed by the use of the discretised Rayleigh integral is the requirement to use a solid planar radiator.

5.2.1 Equivalence of the discretised Rayleigh integral and the analytical solution for the ideal rigid piston

As stated previously, the sound power of an ideal rigid circular piston can be calculated analytically using the Bessel function of the first kind, J_1

(Eq. 5.1.1). In the measurement set-up described here, the piston will only move rigidly in the low frequency range. Of interest is the establishment of an equivalence between the analytical solution and the discretised Rayleigh integral under the assumption that the piston moves uniformly, i.e. rigidly.

In the low frequency range, the following condition holds: $kr = r\omega/c = 2\pi r/\lambda \ll 1$. This means that the wavelength of emitted waves, λ, is much bigger than the radius, r, of the piston. For this condition of $kr \ll 1$, using the series expansion of the Bessel function of the first kind, J_1, the analytical solution for sound power of a rigid piston (Eq. 5.1.1) can be simplified (Eq. 5.2.9) [30].

$$P_{\text{rigid,simpl.}} = \rho_0 c \pi r^2 v_0^2 \frac{(kr)^2}{2} \tag{5.2.9}$$

In the most extreme case, under the assumption of a rigid piston, one could suppose that a single point measurement would suffice for the use of the discretised Rayleigh integral. This measurement point could be located anywhere on the piston surface. Under this supposition, the Rayleigh integral simplifies as the double sum used to calculate the interaction terms of all measurement points vanishes (Eq. 5.2.10). As the total number of measurement points, N, is unity ($N = 1$) and the movement velocity, v_i, of the single point measured is just the movement velocity of the entire rigid piston, v_0, the single sum is obsolete (Eq. 5.2.11).

Only circular piston are considered in this work. Hence, the surface area, S, can be described in terms of the piston radius, r (Eq. 5.2.12). After simplification the desired result is obtained: $P_{\text{Rayl,simpl.}} = P_{\text{rigid,simpl.}}$ (Eq. 5.2.13). Hence, in the low frequency range - where the piston moves uniformly - the analytical solution and the single-point simplified discretised Rayleigh's integral are equivalent.

$$P_{\text{Rayl.,simpl.}} = \frac{\rho_0 c}{2\pi} k^2 \sum_{i=1}^{N} v_i^2 S_i^2 \tag{5.2.10}$$

$$P_{\text{Rayl.,simpl.}} = \frac{\rho_0 c}{2\pi} k^2 v_0^2 S^2 \qquad \text{since } N = 1 \tag{5.2.11}$$

$$P_{\text{Rayl.,simpl.}} = \frac{\rho_0 c}{2\pi} k^2 v_0^2 \pi^2 r^4 \qquad \text{since } S = \pi r^2 \tag{5.2.12}$$

$$P_{\text{Rayl.,simpl.}} = \rho_0 c \pi r^2 v_0^2 \frac{(kr)^2}{2} \qquad \text{after simplification} \tag{5.2.13}$$

To demonstrate this equivalence numerically, the sound power output of a supposed rigid piston was calculated for different values of kr using the simplification $P_{\text{Rayl,simpl.}} = P_{\text{rigid,simpl.}}$ and placed in relation to the respective non-simplified expressions, P_{Rayleigh} as well as P_{rigid}. As expected, for $kr \ll 1$ the sound power levels for all methods are equivalent. This equivalence holds up to $kr \approx 0.5$ (Fig. 5.2.3).

As the simplification used to obtain $P_{\text{rigid,simpl.}}$ was based on the assumption that $kr \ll 1$, it makes sense mathematically that the equivalence to the complete analytical solution, P_{rigid} (Eq. 5.1.1), breaks at $kr \approx 0.5$. However, the observation that the same is true for the simplified Rayleigh integral, $P_{\text{Rayl,simpl.}}$ (Eq. 5.2.13), requires a further structural explanation.

Closer inspection of $kr \leq 0.5$ reveals that this condition is equivalent to saying that the circumference of the piston, $2\pi r$, needs to be smaller than half the wavelength of the emitted sound waves in air, λ_{a} (Eq. 5.2.14 - 5.2.18). This seems logical. When the piston emits low frequency sound waves, it does so as one unit and can be considered as one monopole. However, when it emits high frequency sound waves, its dimension becomes large in comparison to the wavelength of the emitted waves. Hence, it cannot be considered as one monopole any more but needs to be viewed as a collection of multiple monopoles. For this reason, the single point simplification of the Rayleigh integral, $P_{\text{Rayl,simpl.}}$ (Eq. 5.2.13), is not valid for $kr > 0.5$ even if the piston moves perfectly rigidly.

The same structural effect accounts for the already mathematically justified requirement to use the non-simplified analytical solution, P_{rigid} (Eq. 5.1.1), instead of the simplified analytical solution, $P_{\text{rigid,simpl.}}$ (Eq. 5.2.13), for

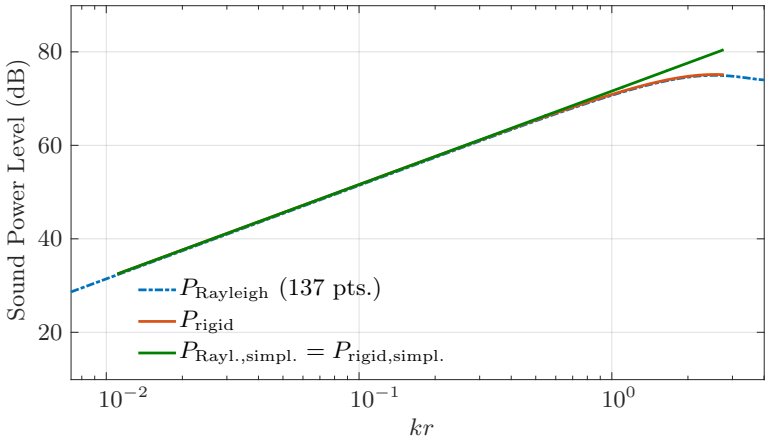

Figure 5.2.3: Sound power calculated for an assumed rigid piston with $v_0 = 5 \cdot 10^{-3}$ m/s using either the complete discretised Rayleigh integral, P_{Rayleigh}, (Eq. 2.3.1), the simplification $P_{\text{Rayl.,simpl.}} = P_{\text{rigid,simpl.}}$ (Eq. 5.2.13) or the analytical solution for a rigid piston, P_{rigid}, (Eq. 5.1.1).

$kr > 0.5$. In that case the behaviour of the Bessel function is the equivalent to the interaction terms of the discretised Rayleigh integral.

For the piston radii relevant to this work $kr = 0.5$ corresponds to frequencies of $f \approx 900$ Hz for a piston radius of $r = 0.03$ m and $f \approx 540$ Hz for a piston radius of $r = 0.05$ m.

$$kr \leq \frac{1}{2} \tag{5.2.14}$$

$$r \leq \frac{1}{2k} \tag{5.2.15}$$

$$r \leq \frac{c}{4\pi f} \tag{5.2.16}$$

$$r \leq \frac{\lambda_a}{4\pi} \tag{5.2.17}$$

$$2\pi r \leq \frac{\lambda_a}{2} \tag{5.2.18}$$

Using an exemplary discretisation of 137 points on the piston surface, it

was shown numerically that the complete discretised Rayleigh integral, P_{Rayleigh} (Eq. 2.3.1), is equivalent to the complete analytical solution for the rigid piston, P_{rigid} (Eq. 5.1.1), in the entire frequency range chosen (Fig. 5.2.3). This is the expected and desired result. The general validity of this statement will be shown mathematically in the following section.

5.2.2 Convergence of the discretised Rayleigh integral

In the previous discussion it was shown numerically that the discretised Rayleigh integral converges to the analytical solution for a rigid piston, given that a sufficient number of measurement points is used. This shall now be shown mathematically, as well.

The reader is reminded of the following three statements, which are considered general knowledge and, thus, used without proof:

$$\lim_{x\to\infty} \frac{\sin(x)}{x} \to 0 \tag{5.2.19}$$

$$\lim_{x\to 0} \frac{\sin(x)}{x} \to 1 \tag{5.2.20}$$

$$\left|\frac{\sin(x)}{x}\right| < 1 \quad \forall x \quad \text{(Fig. 5.2.9a)} \tag{5.2.21}$$

The following simplifying assumptions describe the rigid motion assigned to the piston:

$$v_i = v_j \quad \forall i,j \quad \text{uniform motion} \tag{5.2.22}$$

$$S_i = S_j \quad \forall i,j \quad \text{uniform distribution of sampling points} \tag{5.2.23}$$

$$\sum_{i=1}^{N} S_i = S \quad \text{no surface area of interest is unsampled} \tag{5.2.24}$$

$$\phi_i = \phi_j \quad \forall i,j \quad \text{uniform motion} \tag{5.2.25}$$

$$d_{ij} = d_{ji} \quad \forall i,j \quad \text{regular Cartesian coordinate grid} \tag{5.2.26}$$

Mathematically speaking, there are two variables for which limit considerations can be made: the frequency, f, as well as the number of sampling points, N. From a practical standpoint, however, only considerations on N are sensible here. In all measurements relevant to this work the frequency

range was fixed to 20 Hz - 20 kHz and only the number of sampling points was varied. For this reason, the convergence of the discretised Rayleigh integral only considers convergence for large N and not f throughout this work.

In order to verify the convergence under these conditions, it will be assumed that the frequency, f, is constant while the number of sampling points, N, approaches infinity. The experimental analogue is to focus on a single frequency band while increasing the number of sampling points, N. As all frequency bands measured were finite, the results are applicable to any of the frequency bands of interest without loss of generality.

The proof of the convergence of the discretised Rayleigh integral for large N will first consider the case of $N = 2$ before realising an induction for all N.

Assumption $N \to \infty$ and f is fixed
Sample Case: N=2

$$
\begin{aligned}
P_{\text{rigid}} = \\
&= \frac{\rho c}{2\pi} k^2 \Big[v_1^2 S_1^2 + v_2^2 S_2^2 + v_1 v_2 S_1 S_2 \frac{\sin(k d_{1,2})}{k d_{1,2}} \cos(\phi_1 - \phi_2) + \\
&\quad + v_2 v_1 S_2 S_1 \frac{\sin(k d_{2,1})}{k d_{2,1}} \cos(\phi_2 - \phi_1) \Big] \qquad (5.2.27) \\
&= \frac{\rho c}{2\pi} k^2 \Big[2 v_1^2 S_1^2 + 2 v_1^2 S_1^2 \frac{\sin(k d_{1,2})}{k d_{1,2}} \Big] \qquad (5.2.28)
\end{aligned}
$$

Using the simplifying assumptions (Eqs. 5.2.22 - 5.2.26), the following simplifications can be made:

$$
\begin{aligned}
P_{\text{rigid}} = \\
&= \frac{\rho c}{2\pi} k^2 \Big[2 v_1^2 (\frac{1}{2} S)^2 + 2 v_1^2 (\frac{1}{2} S)^2 \frac{\sin(k d_{1,2})}{k d_{1,2}} \Big] \qquad (5.2.29) \\
&= \frac{\rho c}{4\pi} k^2 v_1^2 S^2 \Big[1 + \frac{\sin(k d_{1,2})}{k d_{1,2}} \Big] \qquad (5.2.30)
\end{aligned}
$$

Induction on N:
As v_i is assumed to be constant for all measurement points i, it will be denoted as v_0 in the remainder of the proof.

$$P_{\text{rigid}} = \frac{\rho c}{2\pi} k^2 \left[N v_0^2 (\frac{1}{N} S)^2 + v_0^2 (\frac{1}{N} S)^2 \sum_{i=1}^{N} \sum_{\substack{j=1 \\ j \neq i}}^{N} \frac{\sin(k d_{ij})}{k d_{ij}} \right] \tag{5.2.31}$$

$$= \frac{\rho c}{2\pi} k^2 v_0^2 S^2 \left[\frac{1}{N} + \frac{1}{N^2} \sum_{i=1}^{N} \sum_{\substack{j=1 \\ j \neq i}}^{N} \frac{\sin(k d_{ij})}{k d_{ij}} \right] \tag{5.2.32}$$

$$\text{Note that} \quad \lim_{N \to \infty} \max(d_{ij}) = \text{const.} > 0 \tag{5.2.33}$$

The previous statements (Eq. 5.2.33) follows from the observation that the maximal distance between any two points of the entire measurement set is given by those points that are located directly opposite from each other on the edge of the measurement surface, i.e. which are at a distance of approximately one diameter apart. As the size of the measurement surface is assumed to remain constant under increasing numbers of sampling points, the diameter of this surface remains constant. Hence, also the maximally observed distance between any two points from the data set is approximately constant.

Limit considerations as $N \to \infty$ then show the following:

$$\lim_{N \to \infty} k d_{ij} \not\to 0 \tag{5.2.34}$$

$$\text{Thus} \quad \lim_{N \to \infty} \frac{\sin(k d_{ij})}{k d_{ij}} \not\to 1 \tag{5.2.35}$$

$$\text{But (Eq. 5.2.21)} \quad \left| \frac{\sin(k d_{ij})}{k d_{ij}} \right| < 1 \quad , \forall f, d_{ij} \tag{5.2.36}$$

As the following double summation has $N(N-1)$ members, it follows that:

$$0 < \sum_{i=1}^{N} \sum_{\substack{j=1 \\ j \neq i}}^{N} \frac{\sin(k d_{ij})}{k d_{ij}} < N(N-1) \quad , \forall N \tag{5.2.37}$$

This means that:

$$P_{\text{rigid}} < \frac{\rho c}{2\pi} k^2 v_0^2 S^2 \left[\frac{1}{N} + \frac{1}{N^2} N(N-1) \right] \tag{5.2.38}$$

Hence, for fixed finite frequencies:

$$\lim_{N \to \infty} P_{\text{rigid}} < \frac{\rho c}{2\pi} k^2 v_0^2 S^2 \tag{5.2.39}$$

This shows that the sound power P_{rigid} has an upper bound. It can be easily seen that $P_{\text{rigid}} \geq 0$. Thus P_{rigid} is bounded. However, to also be convergent, the following needs to hold:

$$\lim_{N \to \infty} \sum_{i=1}^{N} \sum_{\substack{j=1 \\ j \neq i}}^{N} \frac{\sin(k d_{ij})}{k d_{ij}} \to C_x \quad \text{for some } C_x < \infty \tag{5.2.40}$$

To attempt to validate this statement graphically, histograms of classes showing the distances between measurement points, d_{ij}, were plotted for different numbers of measurement points, N, (Fig. 5.2.4). A convergence in histogram shapes can be seen. If histogram shapes converge, so does the double summation (Eq. 5.2.40) as the wave number k is assumed to be constant.

However, this is an example for a single geometry only. While it suggests that the double summation (Eq. 5.2.40) converges, it is no proof for the general case. Specifically, it should be noted that for all discretisations used here, the measurement points were uniformly distributed. This conforms to the experimental protocol that was used for this work. If discretisations were refined unevenly over the measurement surface (for instance only on some areas of the piston surface), results may vary.

To generalise results, sound power levels using the complete discretised Rayleigh integral were calculated for the Eigenmodes $E = 0$ (rigid piston) to $E = 3$ under different numbers of measurement points, N (Fig. 5.2.5). Per Eigenmode, the resulting sound power levels were referenced to the one that was obtained with the largest discretisation (least minimal distance between measurement points). By plotting these sound power level differences as function of distance between neighbouring points, a convergence for increasing discretisation levels becomes apparent. Connecting this

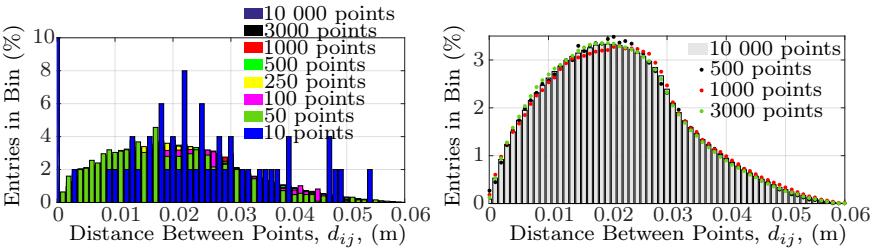

(a) Discretisations using N=10 to N=10 000 points.

(b) Focus on the largest discretisations using $N \geq 500$ points.

Figure 5.2.4: Histograms showing the distribution of linear distances between measurement points, d_{ij}, for varying numbers of measurement points, N. The piston radius measured $r = 0.03$ m. A convergence in histogram shape with increasing N is observable.

result to the discussion on the analytical solution for the rigid piston (Sec. 5.2.1, Fig. 5.2.3) proves that for the case of a rigid piston ($E = 0$) not only does the discretised Rayleigh integral converge, but it converges to the analytical solution.

While this result is no formal proof of the convergence of the discretised Rayleigh integral for all possible surface shapes and discretisations, it was used as argument to conclude that for the experimental set-up relevant to this work, discretised Rayleigh integral sound power levels will converge to a common and accurate value for sound power with increasing numbers of measurement points. This is a fundamental result as it forms the basis for the reasoning that the accuracy of calculated sound power levels will increase with finer discretisations.

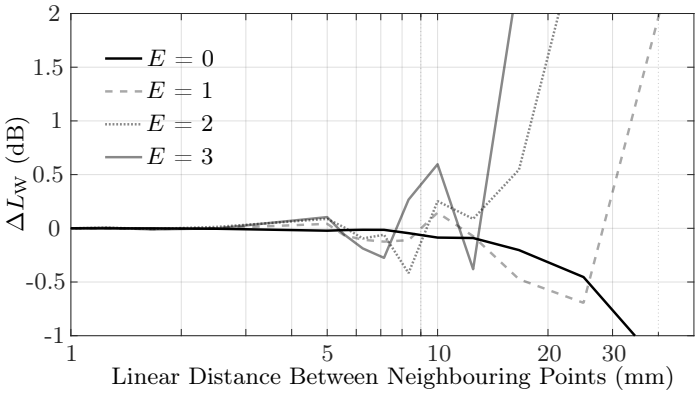

Figure 5.2.5: Difference in sound power level as function of minimal distance between measurement points for Eigenmodes, E, zero to three. Reference sound power level given by the one calculated for the largest discretisation.

5.2.3 Minimal discretisations

From the previous discussion it was concluded that the discretised Rayleigh integral converges with increasing number of measurement points. Minimal numbers of measurement points that were needed for the practical implementation in order to remain below a pre-defined threshold sound power level difference could be extrapolated from these results (Fig. 5.2.5). However, these results are only valid for the ideal Eigenmodes zero to three and were obtained from a single geometry. Thus, broader generalisations were needed.

Essential for any minimal discretisation is that it is sufficiently fine, i.e. that it captures the surface motion well enough so that the calculated sound power is within the desired limit of uncertainty in comparison to the truly emitted sound power. Three different approaches to define such a minimal discretisation will be elaborated:

1. Variation of points per radial distance, n_r, for fixed Eigenmodes and their frequencies

2. Development of unifying equations describing minimal discretisations for all Eigenmodes (after [20])

3. Specific measurement data

In this section the terms discretisation and grid are used interchangeably. While the term discretisation could be seen as mathematical description, the term grid describes the experimental representation of an (ordered) collection of measurement points. In so far, both terms describe the same collection of points and are used as equals.

5.2.3.1 Variation of discretisation for fixed Eigenmode frequencies

Once a piston has been designed in terms of material and diameter choice, the frequency location of its Eigenmodes can be calculated (see App. A for details). At this point, rather than focusing on the exact frequency location or material parameters, though, the Eigenmode shapes were focused on. These are characteristic of circular pistons and independent of material choice. Only symmetrical Eigenmodes were considered since excitation was modelled to occur at the centre point and no tilting of the piston assumed. A focus was placed on varying the sampling for the different mode shapes. Matching the exact amplitude of the actual measurement set-up was deemed to be of secondary importance. Hence, amplitudes were simply scaled to a maximal deflection of $1.5{\cdot}10^{-3}$ m which roughly corresponded to those that were observed in initial test measurements [37]. In this way, the shape and relative position of points to each other was retained for all Eigenmodes (Fig. 5.2.6). This was considered to be the primary factor determining the accuracy of calculated sound power levels under different discretisations.

To develop a systematic discretisation scheme, the piston radius, r, and polar angle π were used as reference lengths. These lengths were then subdivided into segments of equal size according to the desired number of points per reference distance - which was denoted as n_r. For simplicity, the same value of n_r was used for the radial distance and polar angle. Considering that only symmetrical Eigenmodes were considered, this approach should not have skewed results in any direction. Lastly, the piston's centre point was always included in the discretisations (Fig. 5.2.7).

For a chosen discretisation, the deflection of each point within the discretisation was calculated (Eq. A.0.5) and scaled so that the maximal deflection for the entire discretisation - which of course always occurred

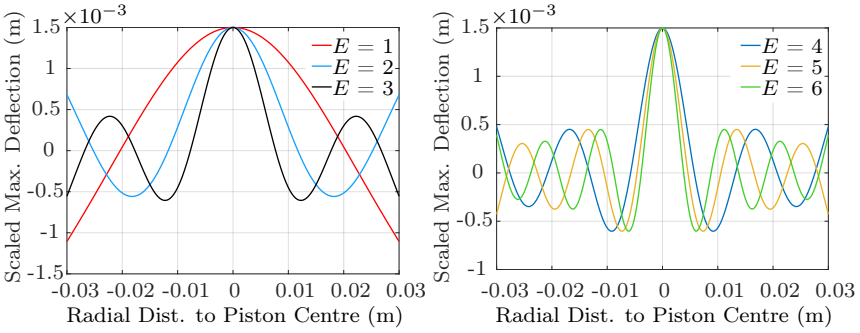

Figure 5.2.6: Shape of the first 6 Eigenmodes, E, scaled to a maximal deflection of $1.5{\cdot}10^{-3}$ m.

at the centre point - was $1.5{\cdot}10^{-3}$ m (Fig. 5.2.7). From the deflection at every point, the associated velocity was calculated taking the relevant Eigenmode frequency, f_E, into account. The piston surface was assumed to be in the x-y plane (zero deflection). Points with negative deflection were assigned the phase angle $\phi = -\pi$. Points with positive deflection were assigned the phase angle $\phi = \pi$. While this could be considered random, this approach again focused on retaining the relative location between points rather than the accurate magnitude. As a last pre-requisite to the use of the discretised Rayleigh integral, the total surface area of the piston, $S = \pi r^2$, was divided by the number of points in the chosen discretisation. Thus, each point in the discretisation was assigned to represent the same surface area. Finally, the sound power levels for the different Eigenmodes under the varied discretisations were calculated and compared (Eq. 2.3.1, Fig. 5.2.8).

In a first step, a PMMA piston (Fig. 3.3.1a) corresponding to the one used in initial measurements was modelled. Piston radii of $r = 3$ cm and $r = 5$ cm were assumed (Figs. 5.2.8a - 5.2.8b). The calculated sound power levels for the different discretisations used were referenced to the sound power level obtained with $n_r = 100$. Sound power levels converge before this reference value, so valid conclusions could be drawn. The desired threshold of accuracy was set at 0.5 dB. This corresponded to the total uncertainty for the realisation of the unit Watt aimed at in the project. Realistically, of course, the threshold should be set lower in this case as

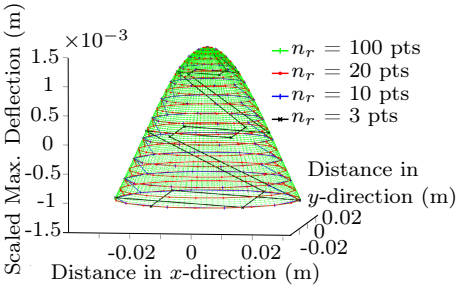

(a) First Eigenmode for grids with 3, 10, 20 and 100 points per radial distance r and polar angle π.

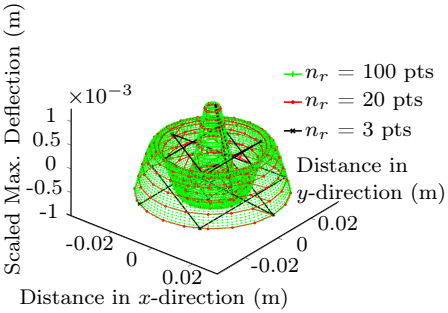

(b) Third Eigenmode for discretisations of 3, 20 and 100 points per radial distance r and polar angle π.

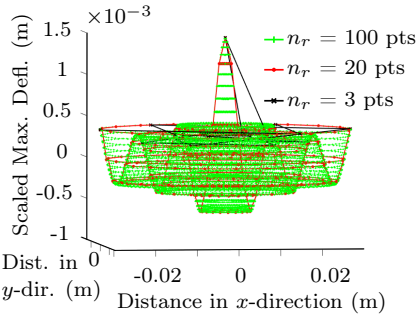

(c) Sixth Eigenmode for discretisations of 3, 20 and 100 points per radial distance r and polar angle π.

Figure 5.2.7: Visualisation of different discretisations.

the total uncertainty includes many more variables than just the influence of the discretisation. However, the threshold of 0.5 dB was retained as further reduction showed no gain in understanding.

Looking at these first results shows that, as expected, higher order Eigenmodes require finer discretisations (Fig. 5.2.8a). This makes intuitive sense and could be assumed based on the visualisations of the surface deflections (Figs. 5.2.7a - 5.2.7c). While for the first Eigenmode small discretisations capture the surface shape with some accuracy, the same cannot be said for the sixth order Eigenmode any more. In fact, the grid with $n_r = 3$ is not able to detect the extent of the range in deflection of

the piston surface nearly adequately for the sixth order Eigenmode (Fig. 5.2.7c, black line).

Secondly, the accuracy of the sound power levels of the different grids does not generally increase with a linear trend. Instead, there is a range of discretisations where the difference to the reference sound power level remains almost constant (Fig. 5.2.8a, purple line for $n_r \approx 10 - 20$). While this does not provide immediate insight, it shows the importance of selecting a reference discretisation that is several orders larger than the discretisation under test in order to avoid a false judgement on convergence.

Thirdly, comparing the results for the two different piston radii at first glance suggests that the larger piston of 5 cm radius (Fig. 5.2.8b) requires a lesser discretisation than the smaller 3 cm piston (Fig. 5.2.8a). This could be further evidenced by a comparison to a 25 cm piston (Fig. 5.2.8c). For this larger piston, the Eigenmode frequencies were idealised and distributed in the frequency range that was later used in measurements (20 Hz - 20 kHz). This may not immediately correspond to a physical material but places the analysis in a more reasonable frequency range.

This largest piston requires the smallest amount of discretisation. This is precisely due to the Eigenmode frequencies chosen. Comparing the frequencies for the third Eigenmode, one can see large differences. For the 3 cm PMMA piston, this Eigenmode frequency is located at 118 kHz. For the 5 cm PMMA, the third Eigenmode occurs at 42.4 kHz and for the fictional 25 cm piston the third Eigenmode was set to occur at 5 kHz. This difference in frequencies influences the choice of n_r much more than the difference in radius. To confirm this assessment, a 5 cm piston was modelled twice where in the first case all Eigenmodes were to occur at 100 Hz (Fig. 5.2.8d) and in a second case all Eigenmodes were to occur at 10 kHz (Fig. 5.2.8e). This comparison shows that the frequency of the emitted sound waves is the dominant factor in determining the minimally required discretisation.

Eigenmodes at lower frequencies require a finer discretisation than Eigenmodes at higher frequencies. In fact, for the case where all Eigenmodes were modelled to occur at 10 kHz, almost no difference is discernible in the behaviour of the sound power level differences for the different Eigenmodes (Fig. 5.2.8e). In contrast, for the case where all Eigenfrequencies were assumed to be 100 Hz, differences for small n_r can be observed (Fig.

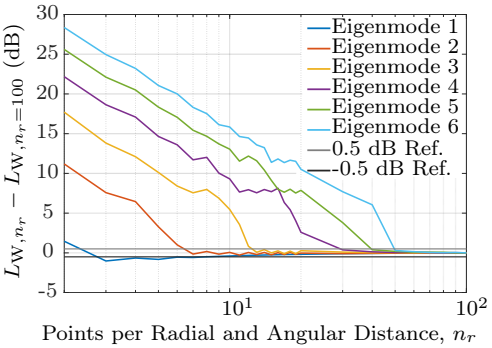

(a) Piston radius $r = 0.03$ m at calculated Eigenfrequencies (see table A.0.1).

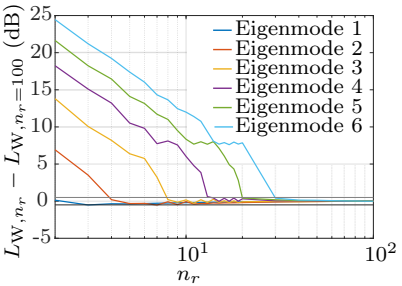

(b) Piston radius $r = 0.05$ m at calculated Eigenfrequencies (see table A.0.1).

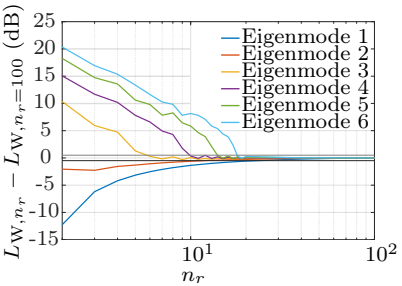

(c) Piston radius $r = 0.25$ m at Eigenfrequencies of $f_{E1} = 100$ Hz, $f_{E2} = 1$ kHz, $f_{E3} = 5$ kHz, $f_{E4} = 10$ kHz, $f_{E5} = 15$ kHz, $f_{E6} = 20$ kHz.

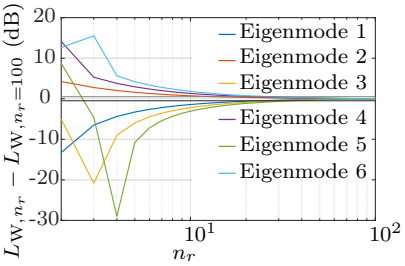

(d) Piston radius $r = 0.05$ m where all Eigenfrequencies were assumed as $f_E = 100$ Hz.

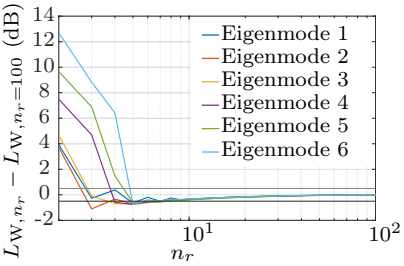

(e) Piston radius $r = 0.05$ m where all Eigenfrequencies were assumed as $f_E = 10$ kHz.

Figure 5.2.8: Results for linear differences in sound power level, L_Δ, depending on discretisation n_r for different Eigenmodes and -frequencies: the reference value for all cases was the sound power level of the grid where $n_r = 100$ (denoted as $L_{W,n_r=100}$).

5.2.8d). The convergence of the difference in sound power level occurs at similar rates, though.

Mathematically this can be explained by investigating the sound power interactions terms, P_{ij}, in the discretised Rayleigh integral (Eq. 5.2.7). Specifically, the term $\sin(kd_{ij})/(kd_{ij})$ is of interest, where k is the wave number and d_{ij} the distance between points i and j. Looking at a plot of this term (Fig. 5.2.9a) shows that the larger kd_{ij} becomes, the less relevant its input to sound power becomes.
For constant k, the physical interpretation then is that the interaction between points that are further away from each other (large d_{ij}) is less important than the interaction between neighbouring points (small d_{ij}). This makes intuitive sense.

For constant d_{ij} the interpretation is that with increasing frequency f (increasing k), the range of relevant neighbouring points becomes smaller. The larger the emitted frequency is, the more each point on the piston surface acts as individual point source that is independent of its neighbouring points. To depict this graphically, different threshold levels for kd_{ij} were chosen and the frequency-distance pairs that fall below the desired threshold plotted (Fig. 5.2.9b). One can observe that for low frequencies even large distances between points fall in the region where $kd_{ij} \leq 10$, i.e. where $\sin(kd_{ij})/(kd_{ij})$ is relevant and the interaction term P_{ij} sizeable. With increasing frequency, the distance d_{ij} where the same is true decays exponentially. This means that for higher frequencies only the interaction of points with very small distances d_{ij} between each other is relevant to overall sound power output.

These observations explain the results for the 5 cm piston with the modelled Eigenfrequencies of 100 Hz versus 10 kHz (Fig. 5.2.8d and 5.2.8e). For smaller frequencies discretisation size has to be chosen such that the interaction between all points on the piston is well sampled. This requires larger grids. For higher frequencies, though, smaller grids with a reasonable resolution of the surface shape are sufficient as each measurement point acts more and more like an isolated point source.

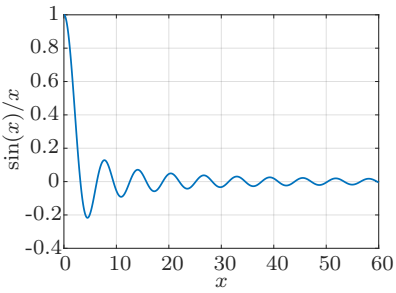

(a) Behaviour of $\sin(x)/x$ for different values of x.

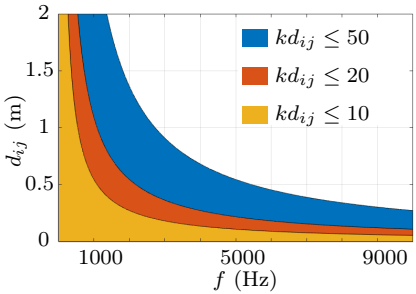

(b) Areas where kd_{ij} is below selected threshold values for combinations of emitted frequency and distance between points i and j.

Figure 5.2.9: Graphical analysis of the importance of the sound power interaction terms, P_{ij} (Eq. 5.2.7), at different frequencies.

5.2.3.2 Variation of discretisation and frequencies for different Eigenmodes

From the results of the previous section it is possible to determine a minimally required discretisation under the assumption of specific material properties and piston sizes for different Eigenmodes at their associated frequencies. These are rather stringent requirements and the scope of the results fairly limited. Hence, the purpose of this section is to extend the results for a minimally required discretisation to the entire frequency range of interest (20 Hz - 20 kHz). Previous work of Hübner et al. served as guideline [20].

For clarity, a change in notation was used for this section. The order of the Eigenmodes was denoted by n and the number of elements per radial and angular distance by N_x. These N_x are equivalent to the n_r used in the previous section. In order to facilitate the distinction between n and n_r, the change in notation was used. Throughout this section, L_Δ denotes a difference in sound power level that is referenced to a grid with $N_x = 50$.

In a first step, the difference in sound power level for the fifth Eigenmode (n = 5) for grids with varying discretisations was plotted over the frequency range of 20 Hz to 40 kHz (Fig. 5.2.10). From this plot, a minimally

necessary discretisation as denoted by $N_{x,\min}$ could be extrapolated for every frequency. $N_{x,\min}$ was defined as that discretisation size for which the sound power level difference, L_Δ, fell below the threshold value for the first time. Consequently, this minimal discretisation depended on the user specified threshold value of L_Δ. For this analysis, the frequency range was extended to 40 kHz even though the practical realisation was limited to 20 kHz. This was mainly done to be able to explore larger values of kr in the next step.

In this next step then, the difference in sound power level, L_Δ, was plotted over kr for varying discretisations (Fig. 5.2.11). This allowed a better understanding of the general behaviour of the sound power level difference for the different discretisations. Conforming to Hübner et al.'s results [20], it showed that there are three distinct phases for L_Δ as it passes over kr.

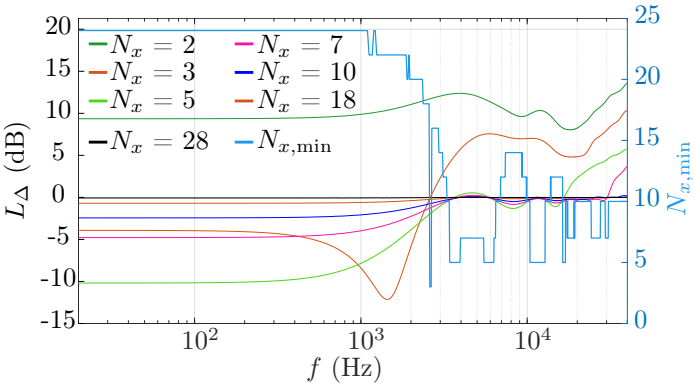

Figure 5.2.10: Difference in sound power level, L_Δ, over frequency, f, for different discretisations of the fifth order Eigenmode (n = 5). A piston radius of $r = 0.05$ m was used and the minimum necessary discretisation, $N_{x,\min}$, with threshold value of $L_\Delta = 0.5$ dB determined for each frequency.

For small kr, all discretisations produce significant sound power level differences L_Δ. With increasing kr, these errors diminish and L_Δ approaches zero. At this point the second phase starts. This second phase can be defined as that stage at which L_Δ is below the desired threshold value. The length of this phase in term of values of kr depends on the chosen discretisation N_x. Larger N_x cover larger values of kr as expected. However,

all discretisations show a divergence of L_Δ for large kr. It commences at a grid characterising value of kr. At this point, the third phase begins. In this stage L_Δ increases with increasing kr.

Plots depicting this behaviour are shown for Eigenmodes 1, 3, 6 and 10, where a piston with radius of 25 cm was assumed (Fig. 5.2.11). This larger piston radius was again used to extend the range of kr. Discretisations for which L_Δ does not fall below the desired threshold value for any value of kr are not suitable for sound power determination at any frequency. These grids only display the first and third stage of the previously described behaviour.

While only the results for the 25 cm piston are shown, the same analysis was carried out for pistons with radii of 3 and 5 cm, respectively. As expected, the difference in sound power level, L_Δ, is solely dependent on the discretisation N_x and independent of the piston radius r. This is true for all Eigenmodes. For this reason, only the 25 cm piston was considered in further parts of this section.

From this analysis of L_Δ over kr, one can find the minimum necessary discretisation, $N_{x,\min}$, for every frequency. This discretisation is given as the smallest N_x for which L_Δ falls below the desired threshold value. As the goal was to realise the unit Watt with an accuracy of 0.5 dB, two threshold values were chosen here. The first threshold value was $L_\Delta < 0.5$ dB and the second threshold was chosen as $L_\Delta < 0.3$ dB. The second threshold is more applicable to the physical realisation of the unit Watt as it would allow for further uncertainty contributions from the measurements itself.

Following the approach of Hübner et al. [20] to analyse the minimally required discretisations systematically, these were put in relation to their corresponding Eigenmode n and referenced to the fraction of solid body wavelength on the piston surface, λ_K, to wavelength of the sound emitted in air, λ_a (Fig. 5.2.12a - continuous lines). In fact, the fraction $\lambda_\mathrm{K}/\lambda_\mathrm{a}$ is given as division of kr by πn (Eq. 5.2.41). This allows for direct comparison of the different Eigenmodes, n.

$$\frac{\lambda_\mathrm{K}}{\lambda_\mathrm{a}} = \frac{kr}{\pi n} \tag{5.2.41}$$

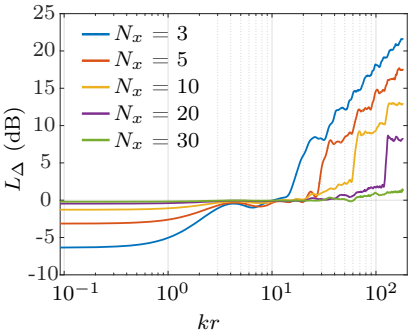

(a) Piston radius $r = 0.25$ m, first Eigenmode.

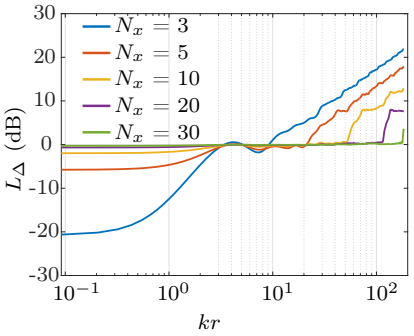

(b) Piston radius $r = 0.25$ m, third Eigenmode.

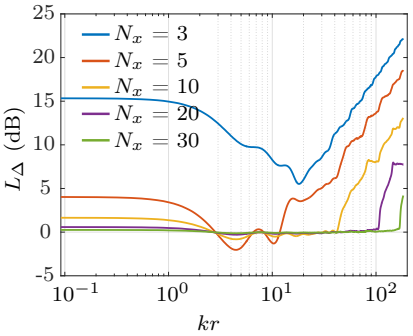

(c) Piston radius $r = 0.25$ m, sixth Eigenmode.

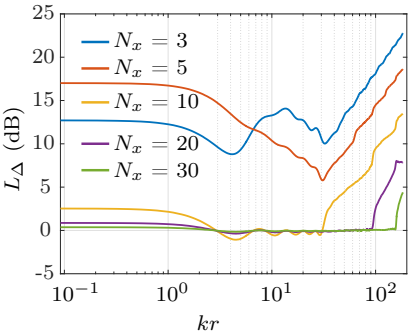

(d) Piston radius $r = 0.25$ m, tenth Eigenmode.

Figure 5.2.11: Results for linear differences in sound power level, L_Δ, over kr for different Eigenmodes and discretisations. The reference discretisation was $N_x = 50$.

It can be seen that, using the strict mathematical definition of $N_{x,\min}$, erratic and outlier prone curves are obtained. As these outliers are not predictable and due to fortunate sampling rather than systematic differences, a smoothing operation was used to obtain more realistic curves (Fig. 5.2.12a - dashed lines). This smoothing was achieved using a moving average with a window length of 100 elements on both sides. In particular, it was possible to match the directly calculated values of $N_{x,\min}/n$ very well with this smoothing for $\lambda_\mathrm{K}/\lambda_\mathrm{a} \geq 1$ (Fig. 5.2.12b).

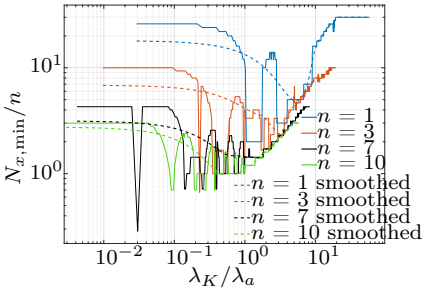

(a) Comparison of directly calculated and smoothed minimum number of discretisation, $N_{x,\min}$, per Eigenmode number, n.

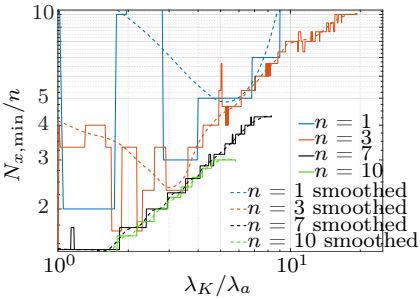

(b) Detailed view of the accuracy of the smoothing operation for $N_{x,\min}/n$ in the area where $\lambda_\mathrm{K} \approx \lambda_\mathrm{a}$.

Figure 5.2.12: Graphical representation showing the approximation of the exact minimum discretisation $N_{x,\min}$ by a smoothed graph.

Calculating the minimal discretisations for all Eigenmodes and kr and applying the smoothing operation, graphs depicting the relation of $N_{x,\min}/n$ over $\lambda_\mathrm{K}/\lambda_\mathrm{a}$ for the first ten Eigenmodes could be plotted (Fig. 5.2.13a). These graphs all follow the same general pattern: for very small $\lambda_\mathrm{K}/\lambda_\mathrm{a}$ the minimal discretisation per Eigenmode is approximately constant. It decreases and reaches its global minimum at $\lambda_\mathrm{K}/\lambda_\mathrm{a} \approx 1$, i.e. where the wavelength on the piston surface and wavelength of emitted waves are approximately equal. This is expected.

For $\lambda_\mathrm{K}/\lambda_\mathrm{a} \geq 1$ then, $N_{x,\min}/n$ increases and displays a linear relation towards $\lambda_\mathrm{K}/\lambda_\mathrm{a}$. This linear relation is the same for all Eigenmodes, n, which conforms to the findings of Hübner et al. [20]. However, here it

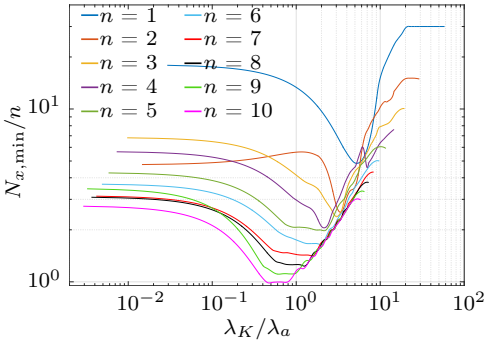

(a) Interpolated minimum discretisations, $N_{x,\min}$, per Eigenmode, n, in reference to the relation of solid body wavelength, λ_K, to emitted wavelength in air, λ_a. The threshold value of 0.3 dB was used.

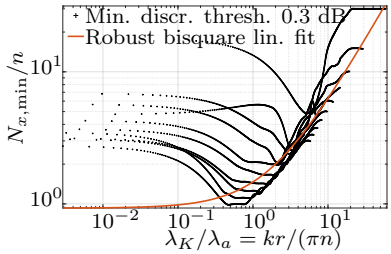

(b) Linear fit of minimal discretisations over the first ten Eigenmodes for a threshold value of 0.3 dB.

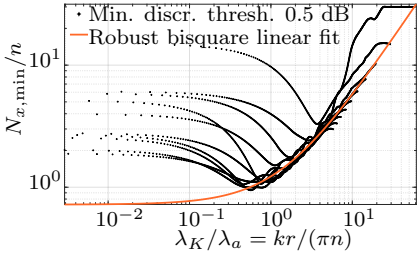

(c) Linear fit of minimal discretisations over the first ten Eigenmodes for a threshold value of 0.5 dB.

Figure 5.2.13: Dependence of minimal discretisations on the relation of solid body wavelength, λ_K, to emitted wavelength in air, λ_a. Lines are only valid for $\lambda_\mathrm{K}/\lambda_\mathrm{a} \geq 1$.

was also shown that this linear relation does not hold when the emitted wavelength, λ_a, is larger than the surface wavelength on the piston, λ_K, i.e. for $\lambda_\mathrm{K}/\lambda_\mathrm{a} < 1$.

In order to establish the equations for the linear relation between $N_{x,\min}/n$ and $\lambda_\mathrm{K}/\lambda_\mathrm{a}$, the collection of values for the ten Eigenmodes was fitted using a robust bisquare linear fit. This was performed both for the threshold of 0.3 dB (Fig. 5.2.13b) as well as for the threshold of 0.5 dB (Fig. 5.2.13c). The equations obtained in this way are given (Eqs. 5.2.42 - 5.2.43). As explained, they are only valid for $\lambda_\mathrm{K}/\lambda_\mathrm{a} \geq 1$.

$$\begin{aligned} \lambda_\mathrm{K}/\lambda_\mathrm{a} \geq 1: \; & L_\Delta < 0.3 \text{ dB} \\ & N_{x,\min} = 0.171kr + 0.930n \quad (R^2 = 0.9886) \end{aligned} \tag{5.2.42}$$

$$\begin{aligned} \lambda_\mathrm{K}/\lambda_\mathrm{a} \geq 1: \; & L_\Delta < 0.5 \text{ dB} \\ & N_{x,\min} = 0.161kr + 0.721n \quad (R^2 = 0.9988) \end{aligned} \tag{5.2.43}$$

For $\lambda_\mathrm{K}/\lambda_\mathrm{a} < 1$, the dependence of the minimally required discretisation $N_{x,\min}$ on the Eigenmode n is not pronounced (Fig. 5.2.14). This result is an extension of the previous discussion on the frequency dependent importance of the interaction terms d_{ij} (Sec. 5.2.3.1). There it was shown that for small frequencies, the phase relation between all points on the piston has to be well sampled. It should be expected that the accurate sampling of phase relations requires a certain number of points, even if the description of displacements on the observed surface could be executed with a much smaller number of points. The current result confirms this claim by showing that, indeed, sampling quality at small frequencies is largely independent of the observed surface displacements.

Hence, a generic value, which is independent of the Eigenmode order, is suggested for discretisations when $\lambda_\mathrm{K}/\lambda_\mathrm{a} < 1$ (Eq. 5.2.44). This generic value of $N_{x,\min} = 30$ is the largest minimal discretisation size for the first ten Eigenmodes at $\lambda_\mathrm{K}/\lambda_\mathrm{a} < 1$ (Fig. 5.2.14). No smoothing operation was applied for its obtention.
While there are Eigenmodes ($n = 4$ for instance) which could be resolved with slightly smaller discretisations, the differences are marginal and, thus, the use of a generic value reasonable.

$$\lambda_\mathrm{K}/\lambda_\mathrm{a} < 1 : \qquad N_{x,\min} = 30 \tag{5.2.44}$$

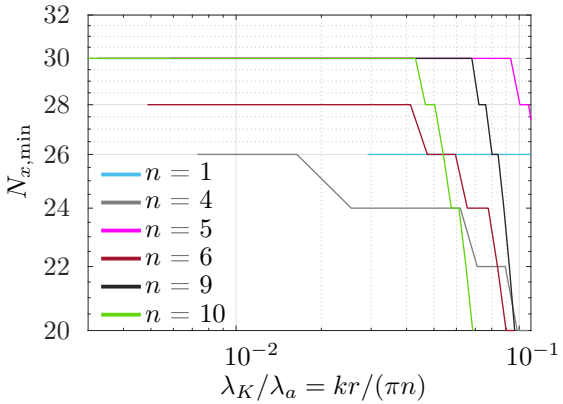

Figure 5.2.14: Minimal discretisation sizes, $N_{x,\min}$, for small $\lambda_\mathrm{K}/\lambda_\mathrm{a}$ and different Eigenmodes, n.

For completeness, it should be noted that for the piston sizes relevant to the project described here, the frequency for which $\lambda_\mathrm{K}/\lambda_\mathrm{a} = 1$ for the first Eigenmode and a piston of size $r = 0.03$ m is given by $f = 5.7$ kHz. For a piston with radius $r = 0.05$ m, that frequency is given by $f = 3.4$ kHz. For larger order Eigenmodes the corresponding frequencies are, of course, higher.

The last part of this chapter will be devoted to an example from real measurement data. As the surface motions observed during measurements are not limited to perfect Eigenmode shapes, that analysis will show if the current ideal shape discretisations are transferable to experimental realities.

5.2.3.3 Measurement data example - using subsets to determine minimal grid size

An experimental analysis on required minimal discretisation was performed for the so called Source 6 (Fig. 3.3.1c). This source featured an aluminium

piston of radius, $r = 2.8$ cm, to which a silicone sealing of width 1.5 cm was affixed. The effective moving piston thus consisted of both the aluminium part as well as the silicone sealing. This source was the only one that was not made of a homogeneous piston material, but rather of two distinct ones with drastically different bending stiffnesses. This, however, was not the design goal. Instead, the silicone sealing was used in the hope that it would provide a better seal of the air gap between piston and baffle.

Of course, it could be expected that the silicone would show rather erratic movement behaviour for higher frequencies. However, the discretised Rayleigh integral does not pose any restrictions on the velocity distribution of the surface. Hence, a sufficient discretisation should nonetheless allow for a correct determination of sound power emission. The increased complexity of this particular source made it the best choice for an experimental determination of minimal discretisation as any result valid for this source could be applied to all of the less complex remaining sources (Fig. 3.3.1).

The reference measurement with the largest discretisation used 1425 scanning points (Fig. 5.2.15a). It included not only points on the piston surface but also points on the surrounding baffle. The measurement procedure itself as well as the need to also scan the baffle were explained in detail previously (Chp. 3 and Sec. 3.2).

From the velocity measurements of the individual points, the mean velocity level on the piston surface was extracted (Fig. 5.2.15b). It shows that the first Eigenmode occurs at approximately 5.5 kHz and the second Eigenmode at 19.15 kHz (Fig. 5.2.16d). Furthermore, there is a first resonance from the silicone sealing at 800 Hz. This resonance creates a mode that is revolving around the piston centre (Fig. 5.2.16b). Further such resonances can be observed at 3.5 kHz as well as between 11 kHz and 15 kHz.

Besides the 800 Hz resonance, the frequency spectrum of the velocity level is smooth until approximately 3 kHz. This indicates uniform motion of the piston for those frequencies (Fig. 5.2.16a). After the first Eigenmode, this smoothness disappears and the frequency spectrum becomes noisy. This is an indicator for the subdivided motion of the piston surface (Fig. 5.2.16c). The observations from the frequency spectrum of the velocity level on the piston surface translate directly to the sound power spectrum of the entire measurement grid (Fig. 5.2.15c).

To proceed with the experimental determination of the minimal discretisation required to replicate the sound power spectrum of the 1425 point grid to within a threshold difference of 0.5 dB, subsets with 200, 400, 500, 650, 800, 1000 and 1200 data points were created. The point sizes of the subsets were chosen such that they represent realistic orders of magnitude for a measurement but without any specific rule to determine their size. The sound power level corresponding to each subset was calculated (Fig. 5.2.17).

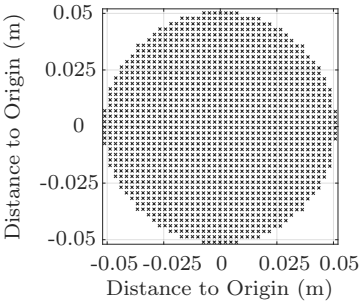

(a) Measurement grid with 1425 points. Piston radius of the source: $r = 0.043$m.

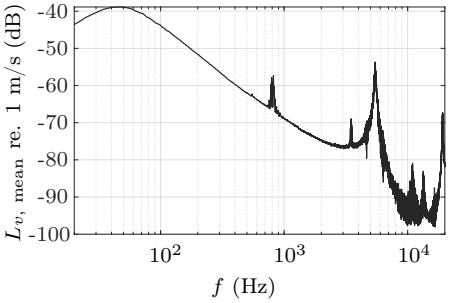

(b) Mean velocity level on the piston surface.

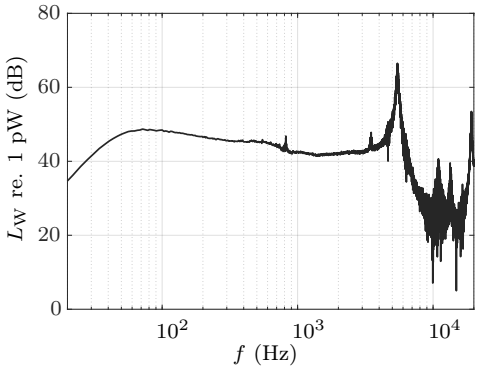

(c) FFT sound power output of Source 6.

Figure 5.2.15: Base data and results from 1425 point measurement of Source 6.

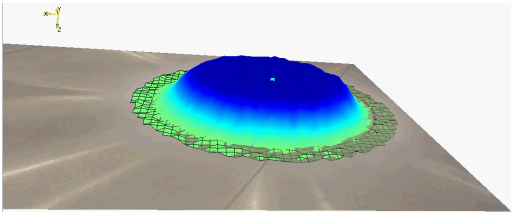

(a) Snapshot of piston motion at $f = 100$ Hz. Piston moves almost perfectly rigidly.

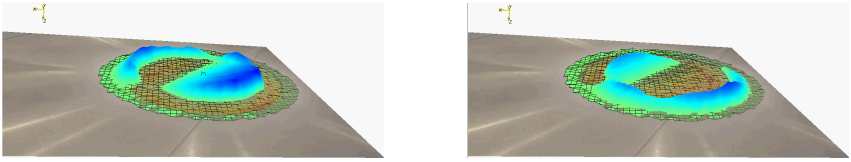

(b) Snapshots of piston motion at $f = 803$ Hz. A mode revolving around the piston centre is visible.

(c) Snapshots of piston motion at $f = 10.825$ kHz. Erratic movement of silicone sealing can be observed.

(d) Snapshots of piston motion at $f = 19.15$ kHz. Second Eigenmode observable.

Figure 5.2.16: Selected piston surface shapes at indicated frequencies.

It is immediately apparent that where the sound power spectrum is smooth, even the smallest 200 point grid approximates the emitted sound power within the desired 0.5 dB threshold level (Fig. 5.2.18a). Differences in the quality of the grids become visible where resonances and erratic surface

motions make the sound power level spectrum noisy. As such, the 200 point grid is not able to resolve the 800 Hz resonance to within threshold level but is able to do so for the first Eigenmode (Fig. 5.2.18a). The 400 point data set displays improving results but is still not able to fully resolve the 800 Hz resonance below threshold value (not shown graphically).

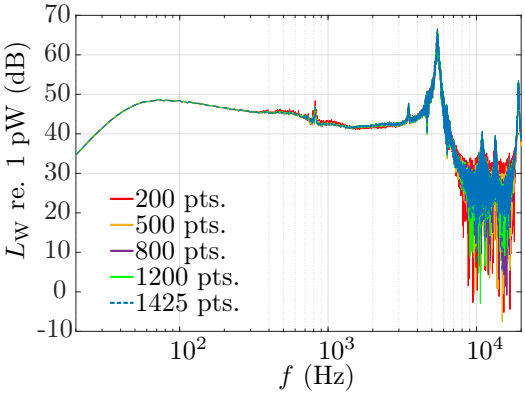

Figure 5.2.17: Comparison of calculated sound power levels using different discretisations.

The resolution of the 500 point grid is good enough to determine the sound power level at the 800 Hz resonance to within threshold level (Fig. 5.2.18b). The 800 (Fig. 5.2.18c) and 1200 point grids (Fig. 5.2.18d) show further increases in accuracy for the 800 Hz resonance as well as for the entire frequency range up to 6 kHz. The minimal discretisations thus are 200 points for frequencies up to 300 Hz and 500 points for frequencies up to 6 kHz. To put this in reference to previous results, the 200 point grid corresponds to $N_x \approx 8$ and the 500 point grid to $N_x \approx 13$. Using the generic formula derived in the previous section for the threshold level of 0.5 dB (Eq. 5.2.43), a discretisation of $N_x = 4$ is obtained for the resolution of the second Eigenmode and $N_x = 2$ for the resolution of the first Eigenmode. Considering that the 200 point grid is able to resolve both Eigenmodes below threshold level suggests that this could be realistic.

The experimental data show, however, that this resolution of Eigenmodes is not the crucial point in the determination of the required discretisation. In fact, no subset grid is able to resolve the frequency range from 6 kHz to 19

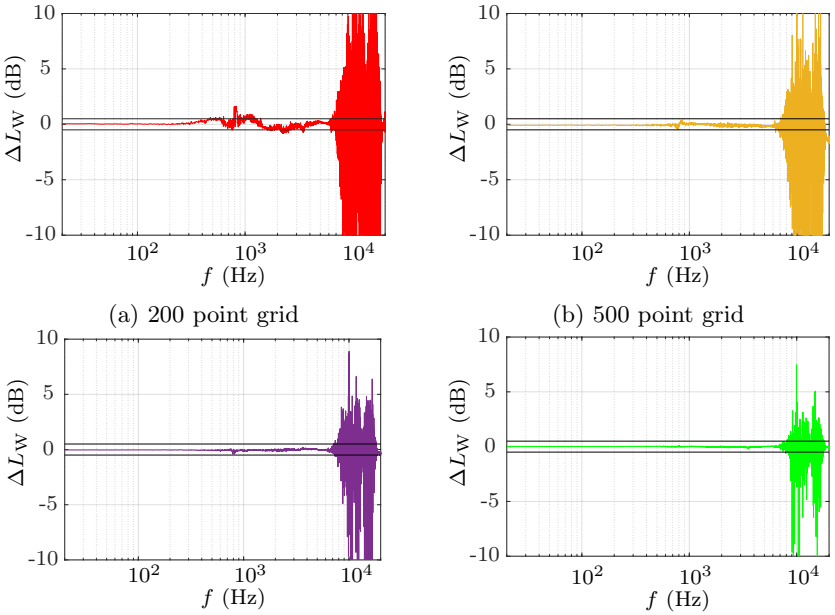

(a) 200 point grid

(b) 500 point grid

(c) 800 point grid

(d) 1200 point grid

Figure 5.2.18: Linear differences in sound power level, ΔL_W, of grids with denoted numbers of points in reference to 1425 point grid. Black horizontal lines denote a threshold of $\Delta L_W = 0.5$ dB.

kHz. This is that frequency range between the first and second Eigenmode where the silicone sealing is displaying largely subdivided motion (Fig. 5.2.16c). While the discretised Rayleigh integral does not pose any limit on such behaviour, this result shows that from an experimental standpoint such behaviour should be avoided. In fact, the lack of convergence to a sub-threshold sound power level even for the 1200 point grid indicates that the 1425 point grid - which was used as reference with the understanding that it should provide the correct sound power level - may itself not be able to determine the sound power level for that frequency range to the desired level of accuracy.

The conclusion from this analysis then is that pistons should be designed such that their surface motion is as even as possible. This is the expected result. Materials with very low bending stiffness should be avoided. While

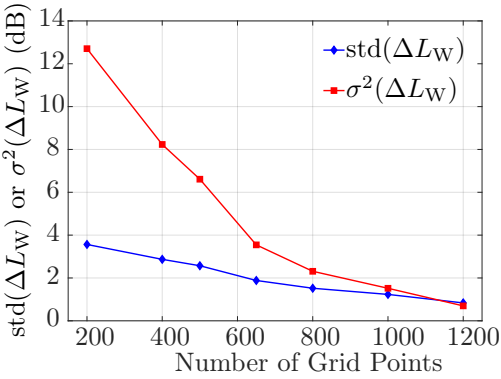

Figure 5.2.19: Standard deviation and variance, σ^2, of sound power level difference, ΔL_W, for different grid sizes.

Eigenmodes do not need extremely fine discretisations for the determination of their emitted sound power, surface shapes with rapidly changing displacement gradients can quickly be too complex to adequately sample in real life measurements.

Lastly, to determine the increase in quality of determined sound power levels for the subset grids, the standard deviation and variance over the entire frequency range from 20 Hz to 20 kHz of the corresponding sound power level difference, ΔL_W, was plotted (Fig. 5.2.19). In particular, the variance can be used as indicator to judge the increase in accuracy that larger grids offer. Considering that neither the standard deviation nor the variance are fully convergent to zero again shows that the 1425 point grid, which was used as reference, does not provide a resolution that is good enough for the entire frequency range measured.

Increasing the measurement grid size could be one solution to this problem. However, as no upper limit to this grid size can be estimated, this could be a very time consuming task. In particular as measurement time also increases with increasing grid sizes. Hence, the more realistic approach is the development of primary sources with improved surface behaviour, which allow for the determination of the emitted sound power with grids of up to 1425 measurement points over the entire frequency range.

In this analysis, the smaller grids were defined by selecting subsets of the largest grid. In reality of course, these smaller grids would be individually defined measurement grids themselves. To evaluate the difference that the simplified subset approach produces, a separate measurement grid with 509 points was established. When compared to a 509 point subset that was selected from the large 1425 point grid, a significant difference in sampling strategies shows (Fig. 5.2.20a).

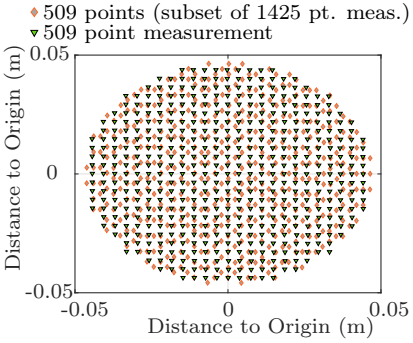

(a) Evenly distributed measurement grid vs more unevenly distributed subset of larger grid.

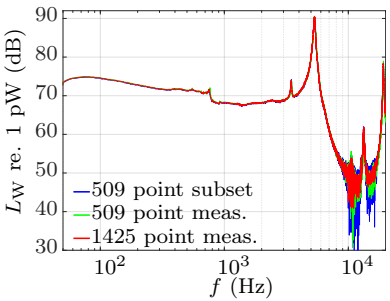

(b) Sound power level comparison for different measurement grids. 509 point sets as depicted in the grid plot.

Figure 5.2.20: Selecting a subset of a larger measurement set yields less exact results than performing a second measurement with a grid of subset size.

Where the individually defined measurement grid (green triangles) shows a uniform distribution over the piston surface, the subset of the larger grid (grey diamonds) is not uniformly distributed. This of course stems from selecting some points from the larger set but not all. In effect, this unequal distribution leads to some areas of the piston that are very well sampled and some areas that are not sampled in the same manner.

While this is not critical for frequency ranges where the piston surface is approximately smooth, this is an important factor for those frequency ranges where the piston surface moves in an increasingly subdivided manner, i.e. the range from 6 - 19 kHz for Source 6. However, while the definition of individual measurement grids improves the accuracy of the

obtained sound power levels (Fig. 5.2.20b) and decreases the standard deviation and variance of corresponding sound power level differences, ΔL_{W}, there is still no convergence of sound power levels over the entire frequency range for the source tested and the conclusions drawn from the analysis of the subset approach remain valid.

6 | Determination of the Uncertainty of the Primary Standard for the Unit Watt

So far, measurement data have been reported without the corresponding uncertainty levels. This, of course, is scientifically wrong. Hence, the goal of this chapter is to develop strategies that allow for the determination of uncertainty budgets relevant to the primary standards under test. All data reported in this chapter pertain to Source 8 (Fig. 3.3.1d) and measurements in the hemi-anechoic room unless specifically denoted otherwise. As the measurement approach that was used is entirely new, there was no previous research or standardised procedure on uncertainty determinations for this specific case. Thus, internationally recognised guidelines - namely the guide to the expression of uncertainty in measurement (GUM) [24] as well as its first supplement detailing the use of Monte Carlo methods [25] - served as references in the determination of uncertainty budgets.

6.1 Pre-Studies

6.1.1 Exclusion of noisy data

As a prelude to the actual determination of uncertainties, the quality of the measured data needed to be assessed. So far, it was assumed that all measurement points provided valid data. Valid in this case meant correctly measured velocities and phase components that were caused by the motion of the primary source only.

The need to check measured data for validity arose from the previously described energy transfer between piston and baffle (Sec. 3.3). As of this point, there had been no source that had been able to completely avoid a transfer of energy from the piston to the surrounding baffle. For this reason, some part of the baffle in the surrounding of the piston had to be sampled during measurements. The first question then was, how much area of the baffle needed to be measured. While this seemed a simple question at first, it did require a strong compromise between area sampled and points used to sample that area. In practice, point densities on the

piston and baffle were chosen to be equal. Considering that the baffle spanned an area that was many orders larger than the piston surface area, even measuring only that part, which was closest to the piston, quickly led to a situation where the number of measurement points on the baffle was larger than the number of points on the piston. This was not desirable as the baffle measurement was not the central part of the investigation. A more detailed analysis of recommended ratios of points on the baffle versus points on the piston surface can be found in the appendix (App. C).

Theoretically though, even measuring many more points on the baffle than on the piston surface should have been unproblematic. The movement velocity of each point should have been very small and the overall sound power contribution of the baffle less than 1 dB. Thus, if all measurement data were valid, one could have measured an infinite number of points on the baffle without any loss in accuracy of the determined sound power level. In reality, this was not true.

In order to demonstrate this, the unfiltered measurement results - frequency responses of peak velocity levels - for every point of a 1425 point measurement were plotted (Fig. 6.1.1a). It is evident that not all points provide valid data. In fact, two areas of interest are visible. The first one is described by those graphs which show peak velocity levels of -40 dB to -60 dB at 100 Hz. These graphs belong to points on the piston surface. The second area of interest is described by those graphs whose peak velocity level is approximately -100 dB for the frequency range of 20 - 50 Hz. These curves belong to points on the baffle whose measurement data describe the true motion of the baffle. By the definition used here, these are points on the baffle with valid measurement data.

All other curves are noise. Two factors were most likely responsible for these invalid measurement data. Firstly, the reflection of the laser light. Ideally, the laser should hit the piston surface at a 90° angle so that the incident and reflected ray travel along the same line. However, this perfect set up could only be achieved for few points. This was partly due to the piston surface not moving perfectly uniform and partly due to the incident angle not being perpendicular for points farther away from the piston centre. Hence, there were points for which the incident ray was scattered upon reflection from the measurement surface. This effect may

have led to invalid measurement data as the part of the reflected ray which reached the laser-scanning vibrometer did not contain information about the measurement surface any more.

Secondly however, the more realistic explanation for the noisy curves is an excitation of the baffle through secondary sources. Namely, the connection of the shaker to its support structure (Fig. 3.3.1d). As only floor-mounted shakers were available during the author's time at PTB, the shaker had to be connected to a fixed structure in some way. In order to have a mobile one-piece source which could be lowered into the measurement room floor cavities, this fixed structure had to be connected to the (brass) ring which surrounded the piston. Even though a maximum level of decoupling was implemented, movement energy was likely transferred from the shaker to the measurement surface. This is the most probable explanation for the noisy curves that were observed.

The central question thus was, how to mathematically distinguish noisy data points from valid data points. A systematic approach that would be easy to generalise and program was desired. Hence, the option chosen here was averaging the measured velocity levels over the frequency ranges from 50 - 200 Hz and 10 - 20 kHz, respectively. If the difference between the two averaged velocity levels was smaller than a pre-defined threshold value, the measurement of that point was considered to be noise and not signal. This point was then excluded from the calculation of sound power because it was assumed that the recorded measurement did not provide valid data (Fig. 6.1.1b). Threshold values used were either 35 or 40 dB as these signal to noise ratios (denoted SNR) provided the best compromise between exclusion of invalid data and retention of a sufficient number of remaining measurement points.

6.1.2 Calculation of sound power with reduced measurement data sets

After adjusting the measurement data to only contain points with valid measurement data, two approaches were followed to obtain sound power levels from the reduced measurement data sets. First, the area covered by the excluded points was distributed evenly among the remaining measurement points and the sound power calculated using just the remaining data.

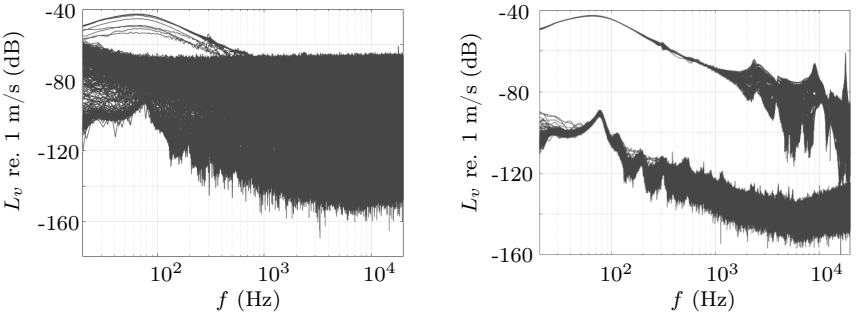

(a) Measured peak velocity levels for the 1425 point grid.

(b) Measured peak velocity levels excluding points with SNR < 35 dB. The upper set of graphs corresponds to the piston surface and the lower set of graphs to the baffle.

Figure 6.1.1: Velocity levels before and after signal to noise filtration for exemplary data of Source 8 at 6 V input voltage.

This meant that all points were assigned to cover the same surface area. Considering that most noisy data points were on the baffle (Figs. 6.1.2a - 6.1.2b), this approach led to an artificial increase in piston surface area. However, as the goal in this step was the development of a strategy on the calculation of sound powers with reduced data sets rather than its determination to highest precision, this inaccuracy was tolerated at this stage.

In the second approach, the data for the excluded points was obtained from the remaining data points using an interpolation. In this case only a linear interpolation was possible. This was due to the observation that noise measurements tended to occur within neighbouring points in certain areas of the measurement surface (Fig. 6.1.2b). These areas were primarily on the surrounding baffle, where measured velocity levels were already small. Hence, for example a spline interpolation using the remaining points was not possible.

Comparing the sound power levels from both approaches shows that the linear interpolation leads to an overestimation of the sound power emitted by the source (Figs. 6.1.2c-6.1.2d). Hence, it is better to just exclude data points with noise measurements. In that case, the area covered by the

excluded points should be distributed among the remaining points that measure that same area only - baffle or piston.

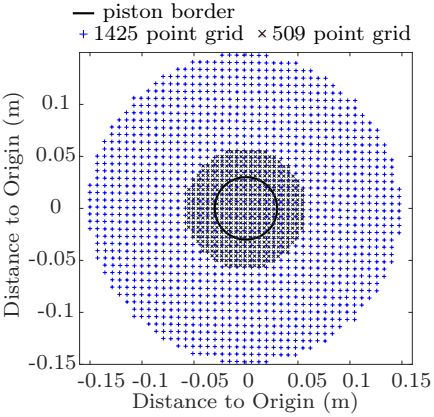

(a) Laser vibrometer measurement grids.

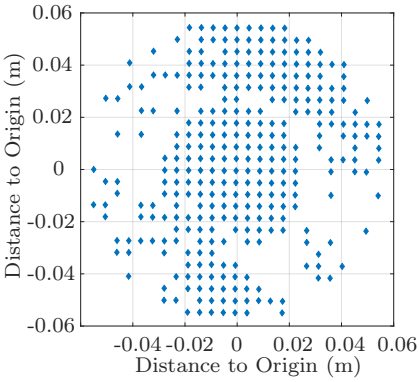

(b) 509 point measurement grid excluding points with SNR < 35 dB. Piston radius, $r = 0.03$ m.

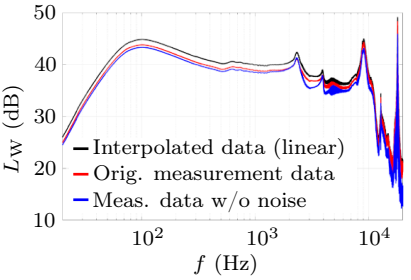

(c) Comparison of calculated sound power level conducting a signal to noise ratio analysis.

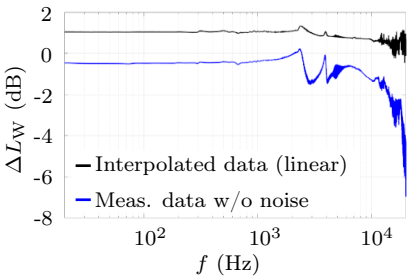

(d) Difference in calculated sound power levels conducting a signal to noise ratio analysis. Data referenced to results of original data set.

Figure 6.1.2: Influence of interpolation on sound power levels.

6.1.3 Influence of individual parameters

The parameters that determine the uncertainty of the obtained sound power levels are naturally those that appear in the discretised Rayleigh

integral formulation (Eq. 2.3.1). These are:

- velocity (RMS value)
- associated phase angle
- x-, y-coordinate
- speed of sound in air, c
- density of air, ρ

The first three of these uncertainty contributors are specific to each data point while the last two can be considered as constant for each entire measurement run. This was the assumption that was made here, as the duration of an entire measurement was in the range of one to two hours. Firstly, the impact of each one of the contributors is discussed individually before the results of a Monte Carlo simulation will be shown. The measurement data used in this subsection pertained to Source 6 (Fig. 3.3.1c).

6.1.3.1 Variation of velocities

Firstly, the influence of the accuracy of the measured velocities was investigated. To do so, normal distributions with mean value zero and standard deviations of 0.1 dB and 0.5 dB were created. For each data point and each one of the 6400 frequency lines measured, one value was chosen at random from the distributions. This value was added to the measured velocity level and the sound power calculated with the thusly modified velocity levels.

By plotting the sound power level differences between the original and modified data, the effect of the velocity variations becomes visible (Fig. 6.1.3). While the 0.1 dB inaccuracy model does not produce substantial differences in calculated sound power levels, the 0.5 dB inaccuracy model shows sizeable effects. According to the data sheet of the manufacturer for the laser scanning vibrometer, the maximal error of measurements is 3%. For measurements on the piston surface, this corresponds to a value between the 0.1 dB and 0.5 dB uncertainty. Hence, the results from the 0.5 dB uncertainty model represent an upper limit on uncertainty from velocity measurements alone.

It should also be noted that grid size counteracts increases in inaccuracies. This is the expected result and can be used as tool should increases in accuracy be required. Bearing the previous discussion about signal to noise ratios in mind (Sec. 6.1.1), though, increases in grid size should occur while maintaining the same maximal distance from the source, i.e. by increasing the density of points on the same amount of total area.

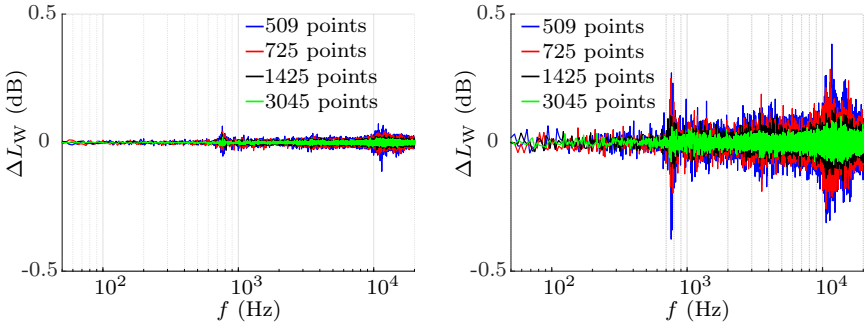

(a) Standard deviation of 0.1 dB.

(b) Standard deviation of 0.5 dB.

Figure 6.1.3: Sound power levels calculated for velocities adjusted with distributions of varying standard deviations. Obtained sound power levels were referenced to respective original solution. Results are reported for grids of varying sizes.

6.1.3.2 Variation of phase components

The same approach as for the velocities was used for the investigation of the dependence of sound power levels on the accuracy of phase measurements. For each frequency line and each data point, the measured phase components were adjusted by a normally distributed random factor with mean value zero and standard deviation of 1° or 5°. The calculated sound power levels were referenced to the sound power level calculated for the respective original measurement (Fig. 6.1.4).

Comparing these results for the phase variations to those of the velocity variation (Fig. 6.1.3), indicates that, generally speaking, the calculated sound power levels react more strongly to inaccuracies in velocity measurements than to those in phase measurements. Only for resonance frequencies

this does not hold true. The 5° variation of velocities again corresponds to the maximal error to be expected. Increasing the number of measurement points on a constant total measurement area reduces the difference in sound power level for all frequencies. This is congruent with the result obtained for the velocity variation.

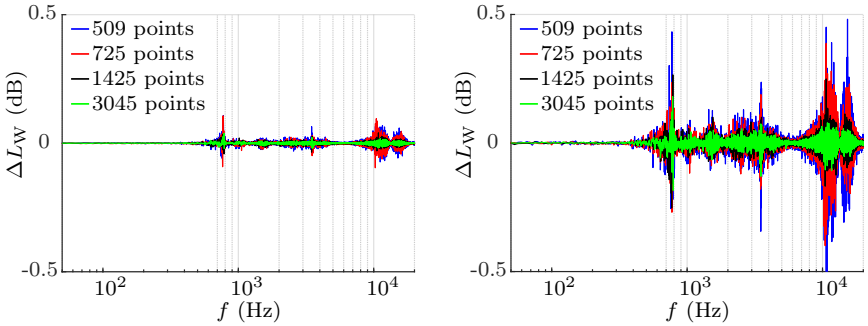

(a) Standard deviation of 1°.

(b) Standard deviation of 5°.

Figure 6.1.4: Sound power levels calculated for phase components adjusted with distributions of varying standard deviations. Obtained sound power levels were referenced to respective original solution. Results are reported for grids of varying sizes.

6.1.3.3 Variation of distance between measurement points

To assess the dependence of sound power levels on the accuracy of x- and y-coordinate measurements, each grid point was adjusted by a normally distributed random factor that was drawn from a normal distribution with mean value zero and standard deviation of 1 mm . Analogous to the previous procedures, the calculated sound power levels were referenced to the respective original data.

To analyse the results of this variation, one key consideration is the degree of distortion that the variation introduced into the measurement grid. For instance, the adjusted 509 point grid does not appear evenly distributed any more (Fig. 6.1.5a). But for most points, the assumption holds that an adjusted point did not move past a neighbouring point of the original data set. Hence, the original grid is fairly well represented by the adjusted grid and the calculated sound power levels do not deviate much (Fig. 6.1.5b).

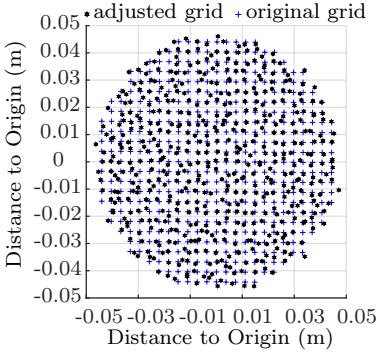

(a) Comparison of 509 point grids used for computations – black grid points adjusted by random normal factor with standard deviation 1 mm.

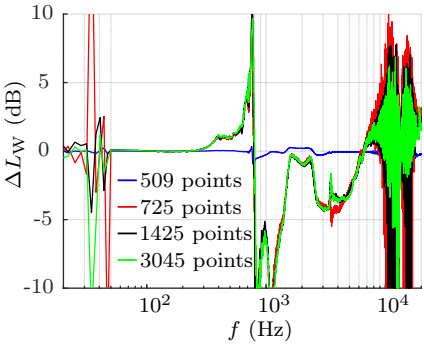

(b) Effect on sound power levels for grid uncertainties of 1 mm for each grid point. Sound power levels for the adjusted grids were referenced to corresponding original grid sound power levels.

Figure 6.1.5: Variation of x- and y-coordinates of measured grid coordinates.

This changes for larger grid sizes. There, the mean distance between neighbouring points in the original data set is significantly smaller than 1 mm. Hence, the adjusted grid does not represent the original data well any more. This means that the modelled piston surface displacement is significantly different from the originally measured one. This is why the difference in sound power level is larger for larger grids (Fig. 6.1.5b). This is especially true for frequencies where the piston does not move uniformly.

Overall, the sound power level differences between the varied grid and the original one are also much larger than those observed for the velocity or phase variations. Certainly, the standard deviation of 1 mm in the normal distribution used for this uncertainty modulation overestimates the manufacturer's claim of 3% uncertainty. However, this should not derail from observing that the determination of each data point's coordinates is vital for accurate sound power determinations.

6.1.3.4 Variation of static parameters

The variables density of air, ρ_0, and speed of sound in air, c, correspond to variations in static pressure and temperature. These were assumed to be constant for the duration of one entire measurement. Considering that this was a time span of less than two hours, the assumption seemed reasonable. Hence, variations in ρ_0 and c were modelled by globally selecting one value that was different from the one that was customarily used for calculations. Specifically, $c = 344$ m/s and $\rho_0 = 1.30$ kg/m^3 were used. The obtained sound power levels were related to those which used the reference values of $c = 340.87$ m/s and $\rho_0 = 1.2016$ kg/m^3 (Fig. 6.1.6). These reference values were measured in the hemianechoic room on a regular weather day. They were not confirmed for each measurement as the measurement environments were in a closed building with fairly constant climate. To increase precision of results, static pressure and temperature should be recorded for each measurement run, of course.

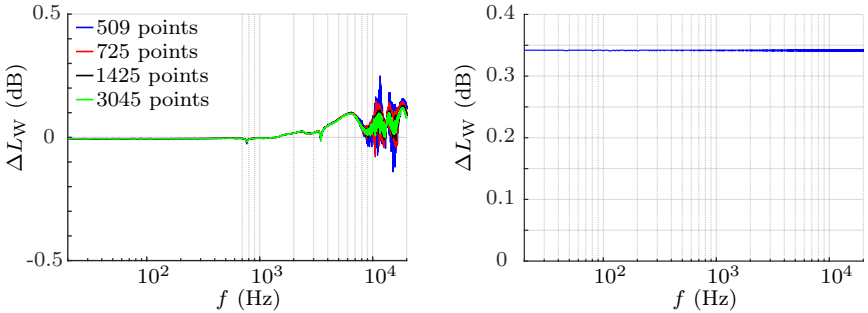

(a) Difference in sound power level for c=344 m/s in comparison to c=340.87 m/s.

(b) Difference in sound power level for $\rho_0 = 1.3$ kg/m^3 referenced to $\rho_0 = 1.2016$ kg/m^3.

Figure 6.1.6: Sound power level differences for variations in density of air, ρ_0, and speed of sound in air, c.

The analysis of results for varying the parameter ρ_0 is very straight forward. As ρ_0 is simply a pre-factor without any dependence on frequency or discretisation in the discretised Rayleigh integral (Eq. 2.3.1), changing ρ_0 simply adds a constant offset to the calculated sound power levels (Fig. 6.1.6b).

Looking at the discretised Rayleigh integral (Eq. 2.3.1), the parameter c appears both as a factor in front of the summation as well as inside the double summation in the wave number k since:

$$k = \frac{2\pi f}{c} \tag{6.1.1}$$

Thus, varying the speed of sound, c, causes differences in calculated sound power levels that are both frequency and discretisation dependent (Fig. 6.1.6a). The differences are larger, the more non-rigidly the piston moves. Considering that even for the relatively small change in temperature modelled here, the maximum difference in sound power level exceeds 0.1 dB, an accurate observation of temperature is necessary for results at highest precision.

6.2 Monte Carlo Simulations - Analysis Routines

Having observed the influence of the individual parameters on calculated sound power levels individually, the next step was the development of a frequency dependent uncertainty budget. Logically, this could not be extrapolated from the data of a single variation of individual parameters as the results would be biased and invalid. Hence, a more rigorous approach was needed. The Monte Carlo method fulfils this requirement and was the most obvious choice for the experimental set-up in use.

The idea of Monte Carlo simulations is to perform a large number of repeat calculations (subsequently also called runs) for the same quantity, where all input parameters are varied concurrently within their individual uncertainty limits. By performing a multitude of such calculations for the output quantity, its true mean and standard deviation as well as coverage intervals can be estimated. With this, the uncertainty of the resulting variable (here: sound power) can be determined, taking into account the uncertainty of all input parameters at the same time (here: velocity, phase, x- and y-coordinates, static pressure and temperature) [25].

The quality of Monte Carlo simulations increases with increasing numbers of runs. The guide to the expression of uncertainty in measurement (GUM) suggests one million runs as target [25]. However, this was impossible

to achieve using the full data sets obtained from the measurements in this project. This was due to the complexity of the discretised Rayleigh integral (Eq. 2.3.1) which, among others, includes an NxN matrix with the distances of all points to each other (N denotes the total number of points sampled). This matrix had to be evaluated for each frequency line measured: 6400 in this case. Hence, the evaluation of the discretised Rayleigh integral with all measurement data was a time consuming task and one million runs not feasible for the full data set.

For this reason, the first approach was to reduce the data set size. This was done in two ways. Firstly, only 24 points on the piston surface were considered in the evaluation. It was confirmed that these points provided valid measurement data. Secondly, only the one-third octave band mid-frequencies in the measured frequency range of 20 Hz - 20 kHz were used. Thus, only 30 of the measured 6400 frequency lines and only 24 of the sampled 509 points were evaluated. With this significant reduction in model size, one million runs of a Monte Carlo simulation could be realised.

For each run and each frequency line, the measured input data velocity as well as x- and y-coordinate were modified independently by a random number drawn from a uniform distribution with mean value one and half-width 3%. The measured phase values were modified in the same way using a uniform distribution with mean value zero and half-width 3°. The speed of sound in air, c, as well as the density of air, ρ_0, used the same distribution as was used for the velocity variations. However, ρ_0 and c were modified by the same factor for all frequencies whereas velocities were modified individually for each frequency line. The choice to use uniform instead of normal distributions as in the pre-studies (Sec. 6.1) was made in accordance with the manufacturer's data sheet for the laser-scanning vibrometer in use. There, only a global uncertainty value of 3% is given. This is represented most accurately by uniform distributions. In utilising these, realistic estimates for the uncertainties of the determined sound power levels could be expected.

From the distribution of the thusly calculated sound power levels for the 10^6 runs, a mean and an expanded uncertainty corresponding to a 95% coverage interval ($k = 2$) was calculated for each one-third octave band mid-frequency (Fig. 6.2.1, Tbl. 6.2.1). Considering that the maximum of these expanded uncertainties is 0.23 dB indicates that the accuracy

of 0.5 dB, which was desired for the realisation of the unit Watt, could be realistic. However, as these first results were based on a drastically reduced measurement set, further and more detailed investigations were necessary.

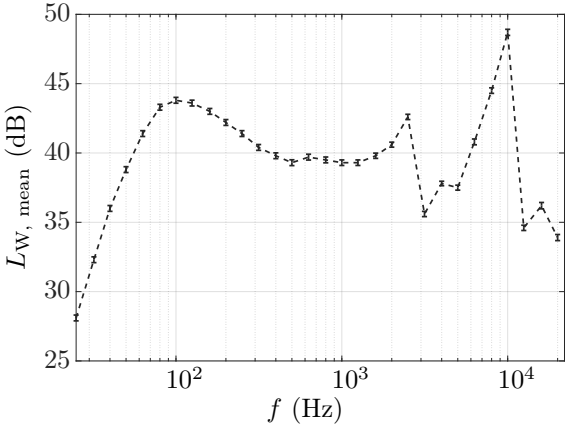

Figure 6.2.1: Mean sound power levels including expanded uncertainties from Monte Carlo simulation - 10^6 runs and $\pm 3\%$ / $\pm 3°$ uncertainties. Measurements were performed using Source 8.

6.2.1 Establishment of a general analysis routine

In order to generalise the results on uncertainty, three different measurements were analysed. The first one used a grid with 509 measurement points while the latter two used the same 1425 point grid. The three measurements were performed independently of each other on different days in PTB's hemi-anechoic chamber with the laser-scanning vibrometer pointing through a hole in the ceiling onto the piston surface (see Fig. 4.1.1 for reference). Source 8 was used with an input voltage of 5V for the shaker in all three measurements.

To establish a data analysis routine, the following three questions needed to be answered:

1. How to filter noisy data?
2. How many runs in the Monte Carlo simulations to perform?

3. Which metrics to report?

As no standardised procedure for the data analysis was available, the methods used in this work represent a suggestion and first approach. Without doubt, different ideas could be explored in future works.

Table 6.2.1: Results from Monte Carlo simulation - 10^6 runs and ±3% / ±3° uncertainties.

Frequency (Hz)	**Mean Sound Power Level (dB)**	**Expanded Uncertainty (k=2) (dB)**
25	28.1	0.21
31.5	32.3	0.21
40	36.0	0.21
50	38.8	0.21
63	41.4	0.21
80	43.3	0.21
100	43.8	0.21
125	43.6	0.21
160	43.0	0.21
200	42.2	0.21
250	41.4	0.21
315	40.4	0.21
400	39.8	0.21
500	39.3	0.21
630	39.7	0.21
800	39.5	0.21
1000	39.3	0.20
1250	39.3	0.20
1600	39.8	0.19
2000	40.6	0.18
2500	42.6	0.19
3150	35.6	0.19
4000	37.8	0.16
5000	37.5	0.18
6300	40.8	0.21
8000	44.5	0.20
10000	48.7	0.22
12500	34.6	0.19
16000	36.2	0.23
20000	33.9	0.22

6.2.1.1 Filtration of noisy data

The separation of erroneous noise measurements from valid signal data using signal to noise filters was already discussed at the beginning of this chapter (Sec. 6.1.1). This method involves the determination of a threshold velocity level difference between the averaged low and high frequency response of each data point, which is denoted by SNR. Here, the hope was to establish a generic SNR value which could be used for the data analysis of all measurements. This would be ideal as it could be transferred most easily to standardised analysis procedures.

Two such threshold values - SNR = 35 dB and SNR = 40 dB - were assessed based on the 509 point measurement data set (Fig. 6.2.2). These specific SNR values were chosen based on the experience that they provided the best compromise between exclusion of noisy data and retention of sufficient data points for a valid analysis.

Looking at the unfiltered data from the 509 point measurement, a clear distinction between piston velocity levels (upper family of curves) and baffle velocity levels (lower family of curves) could be made (Fig. 6.2.2a). However, in the low and mid-frequency range there are also measurement curves visible which lie between the piston and baffle measurements. These curves were assumed to represent faulty measurement data and were to be excluded by the SNR filtration.

The SNR = 35 dB filter retained 435 of the original 509 points. However, it was not able to improve the quality of the velocity level spectrogram significantly (Fig. 6.2.2b). It mainly filtered points along a straight path across the measurement surface (Fig. 6.2.2c) but retained some of those points whose velocity level curves fell between the baffle and piston response. Hence, the SNR = 35 dB filter was categorised as providing a level of filtration that was too small for a satisfactory improvement of results. The straight line of excluded points that appeared in the comparison of the unfiltered 509 point grid and the SNR = 35 dB grid (Fig. 6.2.2c) was later found to correspond to a fine fishing line that was part of the experimental set-up for the comparative sound pressure measurements (Fig. 3.2.2). It was removed after the first measurement with the 1425 point grid as it evidently provided more laser reflection than anticipated.

The SNR = 40 dB filter was able to improve the velocity level spectrogram

by refining the distinction between piston and baffle velocity levels (Fig. 6.2.2d). However, it only retained 223 of the original 509 data points. This meant that less than 50% of the original measurement data were used to represent the entire area measured. Nonetheless, SNR = 40 dB was used as reference filter as its performance in terms of filtration was much better than the SNR = 35 dB filter.
The points that remained after the SNR = 40 dB filtration were essentially those that were on the piston surface as well as small parts of the baffle (Fig. 6.2.2e). This led to the conclusion that the measurement of the piston surface itself provided good results and that the need for filtration arose primarily from the baffle measurements.

In the 1425 point data sets, the limitations of the generic SNR filter approach became more apparent. Based on the experience with the 509 point data set, only the SNR = 40 dB filter was used. For the first measurement set, this SNR filter reduced the data set to 764 points but could not significantly improve the velocity level spectrogram (Figs. 6.2.3a - 6.2.3b). In the filtered grid the fishing line was again visible (Fig. 6.2.3c) but in contrast to the results from the 509 point grid, the distinction between piston surface and baffle was much less pronounced. This, of course, was the main reason why the spectrogram did not improve significantly after filtration.

The reason for not increasing the threshold value in the SNR filter beyond 40 dB became apparent in the analysis of the data set of the second 1425 point measurement (Figs. 6.2.4a - 6.2.4b). For this data set, only 251 data points remained after filtration. This corresponds to questionable 18% of the original measurement data. Comparing the filtered and unfiltered grid showed that, again, the filter removed almost exclusively points on the baffle (Fig. 6.2.4c).

So, while the generic SNR = 40 dB filter provided poor results in terms of clean spectrograms for the first 1425 point measurement, it showed a level of filtration for the second measurement set that was too radical. This is the main limitation of a generic filter. Hence, for the second 1425 point measurement a different, individualised filter was finally used. This filter was developed after determination of suitable frequency specific velocity levels from the spectrogram of the unfiltered measurement set (Fig. 6.2.4a). Specifically, the indicator frequencies $f_1 = 100$ Hz and $f_2 = 1500$ Hz were

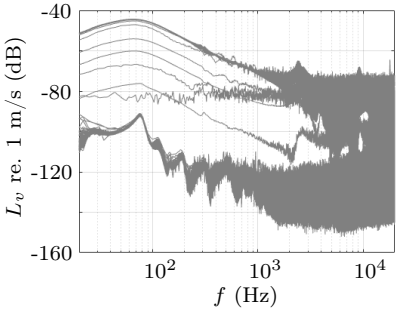

(a) 509 point measurement without filter.

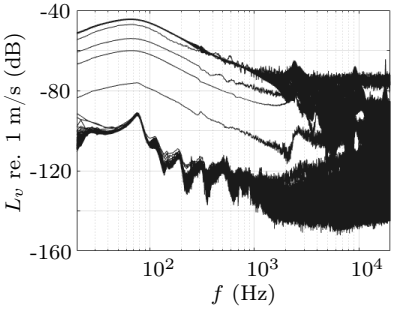

(b) SNR = 35 dB filter. 435 data points remaining.

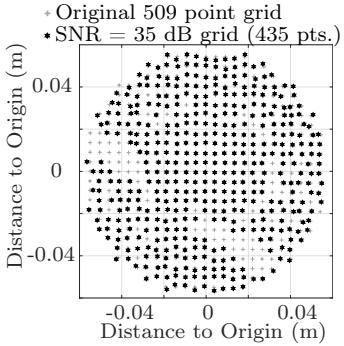

(c) Grid comparison for SNR = 35 dB. $r = 0.03$ m.

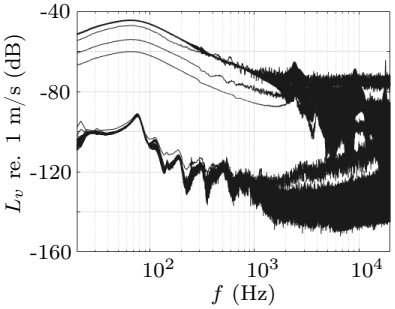

(d) SNR = 40 dB filter. 223 data points remaining.

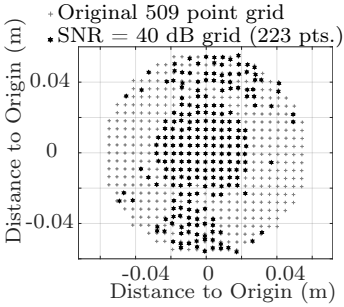

(e) Grid comparison for SNR = 40 dB. $r = 0.03$ m.

Figure 6.2.2: 509 point measurement data with and without signal to noise filtration. Filtered grids include uncertainty modelling.

used. Data points, i, that were allowed to pass the filter had to satisfy either one of the following two conditions:

$$L_{v,i} > \text{-50 dB at } f_1 = 100 \text{ Hz}$$
$$\textit{or}$$
$$L_{v,i} < \text{-125 dB at } f_2 = 1500 \text{ Hz}$$

With this frequency specific filter, 805 of the original 1425 data points were retained and a very clean distinction between piston and baffle velocity levels attained (Fig. 6.2.4d). The noisy data points were filtered efficiently. Interestingly, the comparison between filtered and unfiltered grid showed that now almost exclusively points on the edge of the measurement surface were removed (Fig. 6.2.4e). Hence, this individualised filter provided a better representation of the measurement surface as well as an improved distinction between noisy and valid data.

The disadvantage of individualised filters clearly is the need for case specific fitting of the filter to the measurement data. This would hinder a universal data analysis routine and possibly make it more difficult to compare data for the same source in different measurement locations. Regardless of the filter in use, though, the ideal case is the absence of a need for filtration. Hence, while one could devote a lot of effort into finding the perfect filter, the suggested approach would be to rather spend that time and energy in improving the measurement set-up such as to make the need for filtration obsolete.

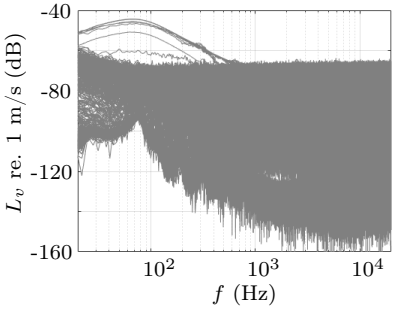

(a) First 1425 point measurement without filter.

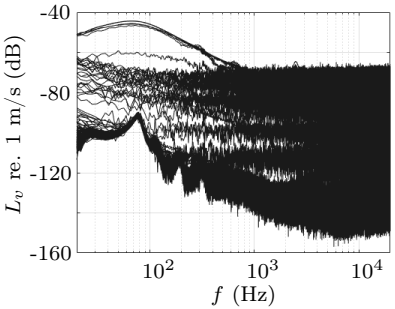

(b) SNR = 40 dB filter. 764 data points remaining.

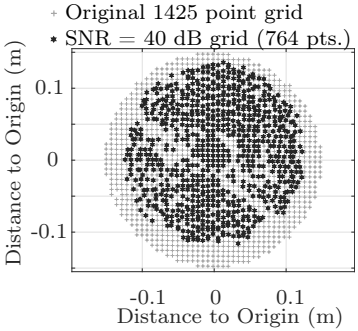

(c) Grid comparison for SNR = 40 dB. Filtered grid includes uncertainty modelling. $r = 0.03$ m.

Figure 6.2.3: 1425 point data from first measurement with and without signal to noise filtration.

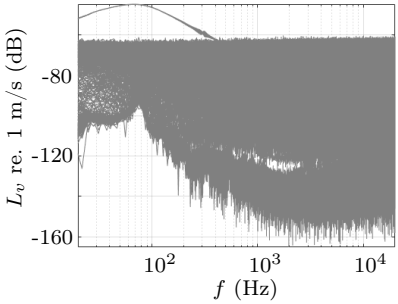

(a) Second 1425 point measurement without filter.

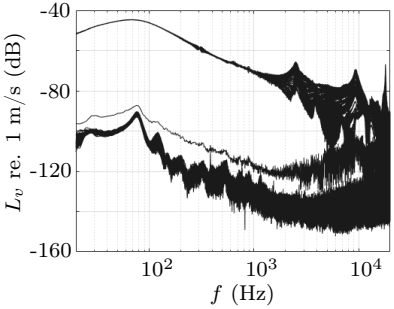

(b) SNR = 40 dB filter. 251 data points remaining.

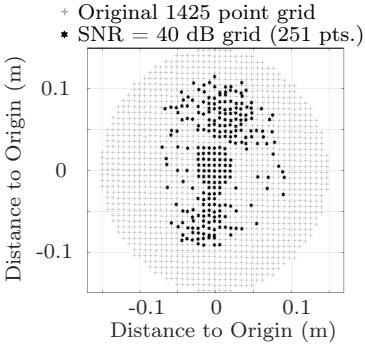

(c) Grid comparison for SNR = 40 dB. $r = 0.03$ m.

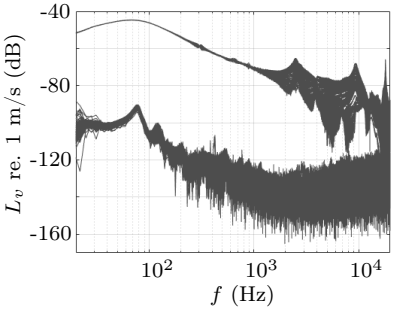

(d) After application of 100 Hz and 1.5 kHz filter. 805 data points remaining.

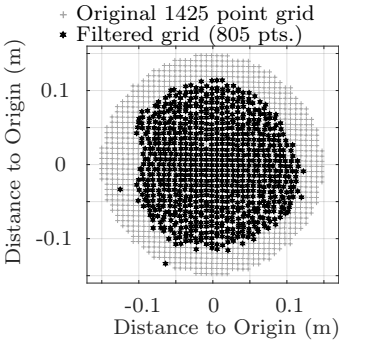

(e) Grid comparison for frequency specific filter. $r = 0.03$ m.

Figure 6.2.4: 1425 point data from second measurement with and without filtration. Filtered grids include uncertainty modelling.

6.2.1.2 Determination of required number of runs in Monte Carlo simulation

The first supplement to the Guide to the Expression of Uncertainty in Measurement (GUM) states that ideally the number of runs, M, should be at least 10^4 times greater than $1/(1\text{-}p)$ - where p denotes the coverage probability [25]. For a coverage probability of 95% thus, at least $2 \cdot 10^5$ runs should be performed. However, each calculation of the discretised Rayleigh integral - meaning each one of the 6400 frequency lines here - involves matrices of the size NxN, with N being the number of data points in the grid used. Hence, each run is time intensive, making the realisation of 200 000 runs impossible even when using filtered measurement data.

The first supplement to the GUM further states that, for cases such as the one here, it is allowable to use a smaller number of runs, M, and regard the probability density function (PDF), $g_Y(\eta)$, with variable η for the output quantity Y, as Gaussian. This normal distribution has to be assigned the mean, y, and standard uncertainty, $u(y)$, from the limited data with a less than optimal number of runs. According to the GUM, this approach does take model non-linearities into account and allows for the calculation of coverage intervals even though it is, logically, less reliable than results obtained from the use of an adequate number of runs [25].

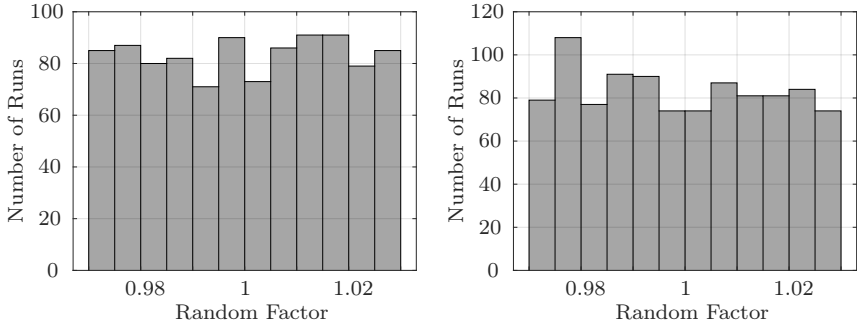

(a) $f = 1$ kHz (b) $f = 10$ kHz

Figure 6.2.5: Distribution of pseudo-random factors used for the velocity measurement uncertainty modelling of Point #118 (most central point at $d = 6.2 \cdot 10^{-4}$ m from the centre of the primary source) in the 509 point data analysis with SNR = 40 dB. Total number of runs: $M = 1000$.

Having established that a smaller number of runs is permissible, it was desirable to develop a better understanding of specific values for numbers of runs M that could be expected to deliver stable results.To do so, the data from the 509 point measurement using the filter SNR = 40 dB were used as basis (Fig. 6.2.2d).

To determine the corresponding sound power levels using Monte Carlo trials, pseudo-random factors were used to modify the input variables velocity, phase, grid coordinates, speed of sound in air and density of air. These pseudo-random factors were drawn from uniform distributions with mean value 1 and suitable half-widths. These half-widths were defined as 3% for the variables velocity (Fig. 6.2.5) and grid coordinates as based on the manufacturer's data sheet. For the variable phase, the half-width was defined as 3° and for the environmental parameters density and speed of sound in air, the half-width of the uniform distribution used was at 1%. The environmental parameters and grid coordinates were modified by the same factor for all frequencies of an entire run whereas velocity and phase data were modified individually for each frequency line. All pseudo-random factors were drawn individually and independently for all variables. They were considered as realistic representations of the uncertainty contribution of the different variables, with more weight placed on those that were measured by the laser-scanning vibrometer rather than the environmental ones.

Once the pseudo-random factors were determined for each variable, the frequency specific sound power level could be calculated using the discretised Rayleigh integral (Eq. 2.3.1). One run in the Monte Carlo simulation consisted of the calculation of sound power levels for all 6400 measured frequency lines from 20 Hz to 20 kHz. The parameter M determined the number of runs that were to be executed.

Considering that the SNR = 40 dB filter removed data points from the original data set, the area corresponding to these points was distributed evenly among those points that covered the same material - piston or baffle - as discussed previously (Sec. 6.1.2). Hence, the total area covered was determined by the unfiltered data set. If points on the piston surface were removed by the filter, their corresponding area was distributed evenly amongst the remaining points on the piston surface. Equivalently, the area of the removed points on the baffle was distributed evenly among

the remaining points on the baffle. Thus, all points on the piston were assumed to cover the same area and all points on the baffle were assumed to represent the same amount of area. This meant that the variation of the measured grid coordinates by pseudo-random factors did not influence the total area covered but did influence the distance matrix, d_{ij} (Eq. 2.3.1), which accumulated the distances between all points in the grid. This simplification aided in the reduction of calculation time and was expected to not alter results. The verification of this assumption for the specific measurement case of this work is documented in the appendix (App. B).

Finally, four distinct Monte Carlo simulations were performed with $M = 100$, $M = 200$, $M = 500$ and $M = 1000$ runs. The simulation covering 1000 runs was regarded as reference and the means, $\tilde{y}$, and expanded uncertainties, U, of the distributions from the other simulations compared to those of the 1000 run simulation (Fig. 6.2.6). The results show that even the Monte Carlo simulation with 100 runs provides results that are comparable to those of the 1000 run Monte Carlo simulation. The rapid convergence of results indicates that stable results can be achieved with a value as little as $M = 100$. This also speaks of the stability of the method for sound power determination used. As the sound power, that is determined by the discretised Rayleigh integral, is based on separate measurements of many points, the impact of each individual uncertainty contribution is minimised. Hence, the thusly obtained sound power levels have very small associated uncertainties.

6.2.1.3 Reported metrics

As described earlier, the first supplement to the GUM states that when Monte Carlo simulations are performed with less than the ideal number of runs, the resulting probability density function (PDF) is to be regarded as Gaussian [25]. In the present case, the random factors used in the uncertainty modulation were drawn from uniform distributions, though. The assumption that the resulting sound power level distributions nonetheless converge to a normal distribution is based on the Central Limit Theorem. This theorem states that the convolution of three or more uniform distributions is approximately normal ([24], Annex G.2).

That assumption on the nature of the resulting sound power level distributions, $G_Y(\eta)$, needed to be confirmed. To do so, the sound power level distributions after Monte Carlo simulations for the three sample frequen-

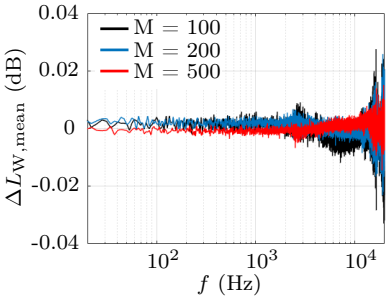

(a) FFT comparison of mean sound power levels for different numbers of runs, M. Reference: $L_{W,mean,M=1000}$

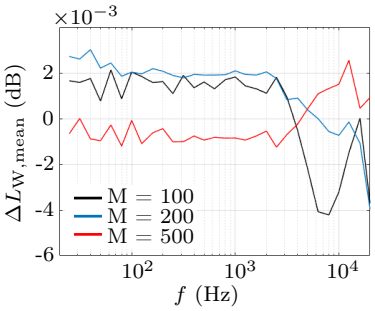

(b) 1/3rd octave band comparison of mean sound power levels for different numbers of runs, M. Reference: $L_{W,mean,M=1000}$

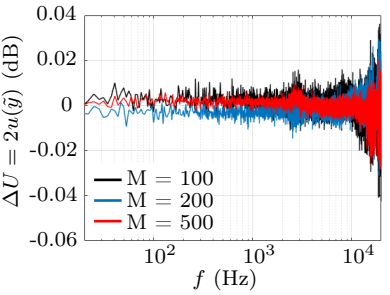

(c) Comparison of exp. uncertainties in FFT lines. Reference: $U_{M=1000}$

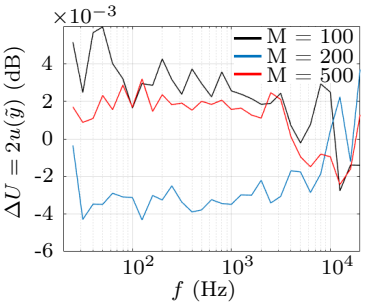

(d) Comparison of exp. uncertainties in 1/3rd octave bands. Reference: $U_{M=1000}$

Figure 6.2.6: Analysis on rate of convergence of Monte Carlo simulations. Reference data given by a Monte Carlo simulation with $M = 1000$ runs.

cies $f = 100$ Hz, $f = 1500$ Hz and $f = 15$ kHz at 100, 200 and 1000 runs M were plotted (Fig. 6.2.7). The result show that the sound power level distributions can indeed be considered as Gaussian. The more runs M that were used, the more closely $G_Y(\eta)$ follows a normal distribution. This is to say that increasing the number of runs, refined the results. Even though only three sample frequencies are shown here, the result was expected to be valid without loss of generality for any combination of frequency and number of Monte Carlo runs.

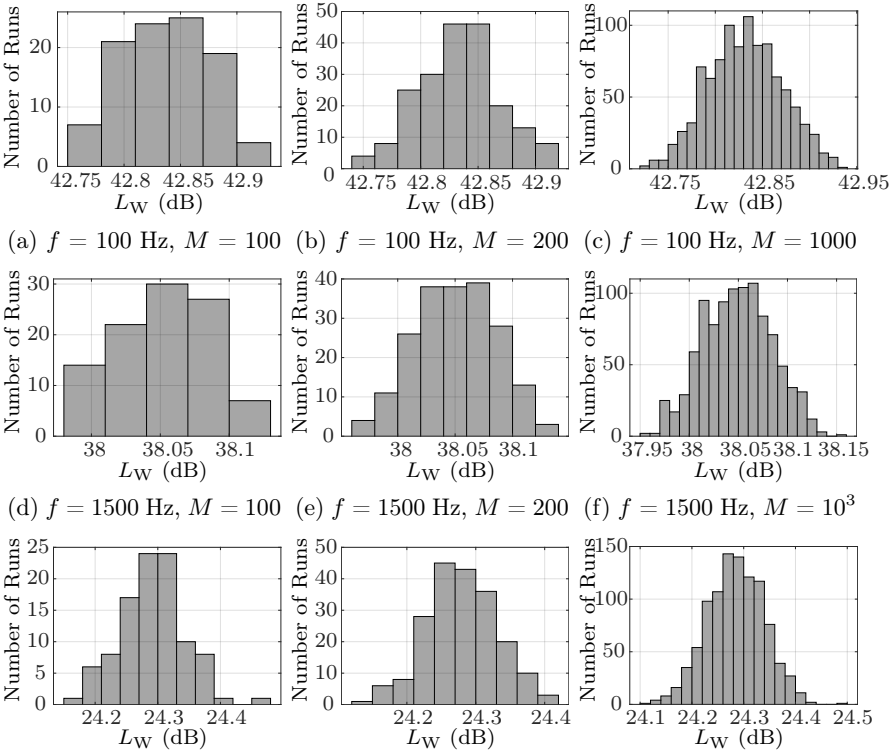

(a) $f = 100$ Hz, $M = 100$ (b) $f = 100$ Hz, $M = 200$ (c) $f = 100$ Hz, $M = 1000$

(d) $f = 1500$ Hz, $M = 100$ (e) $f = 1500$ Hz, $M = 200$ (f) $f = 1500$ Hz, $M = 10^3$

(g) $f = 15$ kHz, $M = 100$ (h) $f = 15$ kHz, $M = 200$ (i) $f = 15$ kHz, $M = 1000$

Figure 6.2.7: Distributions of individual sound power level results from Monte Carlo simulations with either 100, 200 or 1000 runs at exemplary frequencies.

Following the procedure described in the first supplement to the GUM, the mean $\tilde{y}$ and standard deviation $u(\tilde{y})$ of the sound power level distributions obtained from the Monte Carlo simulations were used, respectively, to define the PDF $G_Y(\eta) = \mathrm{N}(\tilde{y}, u^2(\tilde{y}))$. It describes the knowledge of the true PDF for the output quantity Y (here: sound power level). This true PDF is defined as $g_Y(\eta) = \mathrm{N}(y, u^2(y))$ [25].

As last step, coverage intervals needed to be calculated. The first supple-

ment to the GUM describes their direct calculation based on the discrete representation **G** of the distribution functions $G_Y(\eta)$ [25]. These discrete representations **G** correspond to the sound power level distributions obtained from the Monte Carlo simulations in this case. A coverage probability of $p = 95\%$ was desired. Considering, however, that the distribution functions $G_Y(\eta)$ were assumed to be normal and follow the normal probability density function $g_Y(\eta)$, calculating the expanded uncertainty $U = k \cdot u(\tilde{y})$ with a value of $k = 2$ should have also corresponded to a coverage probability of $p = 95\%$ as well [24]. The calculation of expanded uncertainties is computationally simpler than the determination of coverage intervals based on the discrete representations.

Thus, results from both approaches were compared for the Monte Carlo simulation with $M = 1000$ runs (Fig. 6.2.8). By plotting - for every FFT frequency line - the mean value $\tilde{y}$ of the Monte Carlo sound power level distribution together with the corresponding coverage interval and expanded uncertainty, it was confirmed that both methods coincide. Hence, in the further parts of this chapter, the reported metrics are the mean values $\tilde{y}$ as well as the corresponding expanded uncertainties $U = 2 \cdot u(\tilde{y})$ of the sound power level distributions obtained from the specific Monte Carlo simulations.

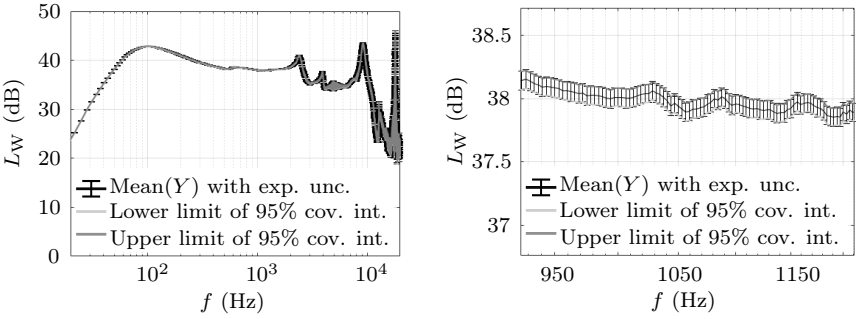

(a) Entire frequency range measured

(b) Detailed view

Figure 6.2.8: Mean sound power levels of the distributions obtained from $M = 1000$ runs in a Monte Carlo simulation for the 509 point grid with SNR = 40 dB. Comparison of interval lengths as defined by either 95% coverage intervals or expanded uncertainties ($k = 2$).

6.3 Monte Carlo Simulations - Results

Measurements using Source 8 were performed with input voltages of 5V and 6V. As a greater number of measurements was performed with the 5V input voltage, the analysis routine in the previous discussion was established based on those data (Sec. 6.2.1). However, for the experimental determination of sound pressure and intensity values in the sound field, an input voltage of 6V was utilised. In order to allow for a comparison with these results in the following chapter (Chp. 7) as well as for completeness, the results of both the 5V and 6V measurements will be shown here.

6.3.1 5V input voltage - comparison of results

For the input voltage of 5V, the same data sets as in the previous discussion (Sec. 6.2.1), were used. This meant data sets from three measurements - namely one 509 point and two distinct 1425 point grids - could be compared. In fact, these three measurements led to five data sets:

- The 509 point measurement without any filtration.
- The 509 point measurement with a SNR filter of 35 dB.
- The 509 point measurement with a SNR filter of 40 dB.
- The first 1425 point measurement with a SNR filter of 40 dB.
- The second 1425 point measurement with frequency specific filtration at 100 Hz and 1.5 kHz.

These five data sets were chosen in this way to provide a good representation of expected measurement results in general. They are diverse enough to cover the aspects of grid size, surface area measured and types of filtration used in a manner that general conclusions can be drawn. The procedure used in the Monte Carlo simulations was described previously (Sec. 6.2.1.2), so that, here, only results will be presented.

The grids as well as velocity distributions for all sets except the one using the SNR = 35 dB filter are shown at the end of this section (Figs. 6.3.1 - 6.3.4). This was done to assure a compact description of the data that form the basis to this comparison and maintain readability. The data from the SNR = 35 dB filtered set were shown previously (Figs. 6.2.2b - 6.2.2c). They were not repeated here as this data set was excluded in the

calculation of piston only sound power levels.

In addition to the filtration using signal to noise threshold values, a cut off frequency of 200 Hz was used in the analysis of the 509 point (Fig. 6.3.2) and first 1425 point measurement (Fig. 6.3.3). Especially the 1425 point velocity levels showed a significant amount of noise even after filtration with the SNR = 40 dB filter (Fig. 6.3.3c). The cut off frequency was based on the assumption that the baffle's impact on sound emission is largest and possibly significant in the low frequency range. Towards the mid and high frequency range, baffle motion does not contribute to emitted sound power any more. Thus, having observed the noisiness in the data even after signal to noise filtration, the idea was to retain the low frequency impact of the baffle but omit its mid and high frequency contribution. To do so, velocity levels that were below -60 dB at 200 Hz were set to the value of -500 dB for all frequencies between 200 Hz and 20 kHz. In this way, no further points were excluded from the analysis. Yet, their effect on sound emission was removed for the corresponding frequency range. This cut off frequency was also used in the analysis of the 509 point SNR filtered data sets in order to maintain consistency in the data analysis. Hence, the only data sets that included baffle sound power contributions over the entire frequency range were the unfiltered 509 point and the second 1425 point measurement with the individualised filter.

Firstly, sound power levels were compared in one-third octave bands (Tbls. 6.3.1 - 6.3.2). Looking at the mean sound power levels for the five different data sets, it is notable that these do not coincide but, instead, show level differences of up to 2 dB (Tbl. 6.3.1). However, the expanded uncertainties for each individual data set are well below this mark (Tbl. 6.3.2). As a matter of fact, for all filtered data sets, the expanded uncertainties for all one-third octave bands are at 0.1 dB. For the unfiltered 509 point data set, the expanded uncertainties are larger but still well below the 1 dB mark. Thus, the filtration did improve data quality but could not explain the differences in mean sound power levels.

The expanded uncertainties of the filtered data sets are smaller than those obtained during the pre-studies that were discussed at the beginning of this chapter (Sec. 6.2). This is partly due to the improvement in data quality due to filtration and the increased number of iterations. The other part is the fact that for the pre-studies all variables were modelled with

uncertainty distributions of 3% standard deviation, whereas for the current analysis, the parameters density of air, ρ_0, and speed of sound in air, c, were modelled with uncertainty distributions of only 1% half-widths.

For the five data sets under investigation here, the differences in mean sound power levels become more apparent still when they are plotted together (Fig. 6.3.5). It is observable that the 509 point data set without any filtration generally provides the lowest mean sound power levels while the second 1425 point measurement with the individualised frequency filter generates the largest mean sound power levels (Fig. 6.3.5a). Both frequency responses are roughly parallel to each other. Yet, an offset of approximately 2 dB can be seen between them. When displaying the mean sound power levels together with their expanded uncertainties for these two data sets, it shows clearly that the difference between the results is not within the uncertainty limits of either one of the data sets (Fig. 6.3.5b). The same holds true when the mean sound power levels of the five data sets are plotted in one-third octave bands (Fig. 6.3.5c). Hence, systematic differences between the resulting mean sound power levels exist.

Table 6.3.1: Comparison of mean sound power levels for 1/3rd octave bands - Monte Carlo simulation with number of runs denoted by M and number of points remaining after filtration by X.

f **(Hz)**	**509 points, no filter,** $M = 1000$ **(dB)**	**509 points, SNR= 35 dB,** $M = 200$**,** $X = 435$ **pts. (dB)**	**509 points, SNR= 40 dB,** $M = 1000$**,** $X = 223$ **pts. (dB)**	**1425 points, meas. 1, SNR= 40 dB,** $M = 200$**,** $X = 764$ **pts. (dB)**	**1425 points, meas. 2, freq. filter,** $M = 212$**,** $X = 805$ **pts. (dB)**
25	26.7	27.6	27.6	27.6	28.1
31.5	35.5	36.4	36.4	36.8	37.1
40	39.2	40.2	40.2	40.6	40.9
50	42.0	42.9	42.9	43.4	43.7
63	46.7	47.6	47.6	48.3	48.6
80	49.1	50.1	50.1	50.7	51.1
100	50.3	51.3	51.2	51.7	52.2
125	51.6	52.5	52.5	53.1	53.5
160	51.6	52.6	52.6	53.3	53.6
200	51.5	52.4	52.4	53.1	53.5
250	51.8	52.7	52.7	53.3	53.8
315	52.4	53.4	53.4	54.1	54.3
400	52.3	53.3	53.3	53.8	54.2
500	53.0	54.0	54.0	54.5	54.8
630	54.5	55.4	55.4	55.9	56.3
800	54.9	55.9	55.9	56.4	56.9
1000	55.5	56.5	56.5	57.2	57.3
1250	56.9	57.9	58.0	58.7	58.7
1600	57.6	58.6	58.7	59.4	59.4
2000	59.0	60.0	60.3	61.0	60.5
2500	60.7	61.8	61.9	63.1	62.6
3150	59.0	59.9	59.3	59.8	61.3
4000	59.4	60.4	60.2	60.9	61.4
5000	59.7	60.7	60.4	61.1	61.8
6300	60.7	61.7	61.7	62.6	62.6
8000	64.3	65.3	65.2	66.0	65.9
10000	67.2	68.1	68.0	68.8	69.9
12500	57.0	57.8	57.9	60.4	59.4
16000	54.8	55.4	55.8	60.4	57.3
20000	60.0	61.1	61.0	63.3	61.9

Table 6.3.2: Comparison of expanded uncertainties ($k = 2$) of sound power levels for 1/3rd octave bands - Monte Carlo simulation with number of runs denoted by M and number of points remaining after filtration by X.

f **(Hz)**	**509 points, no filter,** $M = 1000$ **(dB)**	**509 points, SNR= 35 dB,** $M = 200$**,** $X = 435$ **pts. (dB)**	**509 points, SNR= 40 dB,** $M = 1000$**,** $X = 223$ **pts. (dB)**	**1425 points, meas. 1, SNR= 40 dB,** $M = 200$**,** $X = 764$ **pts. (dB)**	**1425 points, meas. 2, freq. filter,** $M = 212$**,** $X = 805$ **pts. (dB)**
25	0.3	0.1	0.1	0.1	0.1
31.5	0.3	0.1	0.1	0.1	0.1
40	0.3	0.1	0.1	0.1	0.1
50	0.3	0.1	0.1	0.1	0.1
63	0.3	0.1	0.1	0.1	0.1
80	0.3	0.1	0.1	0.1	0.1
100	0.3	0.1	0.1	0.1	0.1
125	0.3	0.1	0.1	0.1	0.1
160	0.3	0.1	0.1	0.1	0.1
200	0.3	0.1	0.1	0.1	0.1
250	0.3	0.1	0.1	0.1	0.1
315	0.3	0.1	0.1	0.1	0.1
400	0.3	0.1	0.1	0.1	0.1
500	0.3	0.1	0.1	0.1	0.1
630	0.3	0.1	0.1	0.1	0.1
800	0.3	0.1	0.1	0.1	0.1
1000	0.3	0.1	0.1	0.1	0.1
1250	0.3	0.1	0.1	0.1	0.1
1600	0.3	0.1	0.1	0.1	0.1
2000	0.3	0.1	0.1	0.1	0.1
2500	0.4	0.1	0.1	0.1	0.1
3150	0.4	0.1	0.1	0.1	0.1
4000	0.3	0.1	0.1	0.1	0.1
5000	0.4	0.1	0.1	0.1	0.1
6300	0.4	0.1	0.1	0.1	0.1
8000	0.4	0.1	0.1	0.1	0.1
10000	0.4	0.1	0.1	0.1	0.1
12500	0.4	0.1	0.1	0.1	0.1
16000	0.7	0.1	0.1	0.1	0.1
20000	0.5	0.1	0.1	0.1	0.1

Table 6.3.3: Piston only: Comparison of mean sound power levels for 1/3rd octave bands - Monte Carlo simulation with number of runs denoted by M and number of points remaining after filtration by X.

f **(Hz)**	**509 points, no filter,** $M = 1000$**,** $X = 137$ **pts. (dB)**	**509 points, SNR = 40 dB,** $M = 1000$**,** $X = 117$ **pts. (dB)**	**1425 points, meas. 1, SNR = 40 dB,** $M = 1000$**,** $X = 42$ **pts. (dB)**	**1425 points, meas. 2, freq. filter,** $M = 1000$**,** $X = 56$ **pts. (dB)**
25	27.5	27.6	27.2	27.5
31.5	36.2	36.3	35.9	36.2
40	40.0	40.1	39.7	40.0
50	42.7	42.8	42.4	42.8
63	47.4	47.5	47.1	47.5
80	49.9	49.9	49.7	50.2
100	51.1	51.2	51.1	51.6
125	52.3	52.4	52.5	52.9
160	52.4	52.5	52.6	53.1
200	52.3	52.4	52.4	52.9
250	52.6	52.6	52.7	53.2
315	53.2	53.3	53.5	53.8
400	53.1	53.2	53.2	53.7
500	53.8	53.9	53.9	54.4
630	55.2	55.3	55.3	55.7
800	55.7	55.8	55.8	56.3
1000	56.3	56.4	56.5	56.9
1250	57.7	57.9	58.0	58.3
1600	58.4	58.6	58.6	58.9
2000	59.8	60.2	60.0	60.2
2500	61.6	61.9	61.7	62.3
3150	59.7	59.3	59.7	60.5
4000	60.1	60.1	60.6	60.7
5000	60.4	60.4	61.0	61.1
6300	61.4	61.7	62.6	62.0
8000	65.0	65.2	66.0	65.1
10000	67.9	68.0	68.7	69
12500	57.8	57.8	60.3	58.6
16000	55.6	55.6	60.2	56.1
20000	61.0	60.9	62.7	60.9

Table 6.3.4: Piston only: Comparison of expanded uncertainties ($k = 2$) of sound power levels for 1/3rd octave bands - Monte Carlo simulation with number of runs denoted by M and number of points remaining after filtration by X.

f **(Hz)**	**509 points, no filter,** M **= 1000,** X **= 137 pts. (dB)**	**509 points, SNR = 40 dB,** M **= 1000,** X **= 117 pts. (dB)**	**1425 points, meas. 1, SNR = 40 dB,** M **= 1000,** X **= 42 pts. (dB)**	**1425 points, meas. 2, freq. filter,** M **= 1000,** X **= 56 pts. (dB)**
25	0.2	0.1	0.1	0.1
31.5	0.2	0.1	0.1	0.1
40	0.2	0.1	0.1	0.1
50	0.2	0.1	0.1	0.1
63	0.2	0.1	0.1	0.1
80	0.2	0.1	0.1	0.1
100	0.2	0.1	0.1	0.1
125	0.2	0.1	0.1	0.1
160	0.2	0.1	0.1	0.1
200	0.2	0.1	0.1	0.1
250	0.2	0.1	0.1	0.1
315	0.2	0.1	0.1	0.1
400	0.2	0.1	0.1	0.1
500	0.2	0.1	0.1	0.1
630	0.2	0.1	0.1	0.1
800	0.2	0.1	0.1	0.1
1000	0.2	0.1	0.1	0.1
1250	0.2	0.1	0.1	0.1
1600	0.2	0.1	0.1	0.1
2000	0.2	0.1	0.1	0.1
2500	0.2	0.1	0.1	0.1
3150	0.2	0.1	0.1	0.1
4000	0.2	0.1	0.1	0.1
5000	0.2	0.1	0.1	0.1
6300	0.2	0.1	0.1	0.1
8000	0.2	0.1	0.1	0.1
10000	0.2	0.1	0.1	0.1
12500	0.2	0.1	0.1	0.1
16000	0.2	0.1	0.1	0.1
20000	0.3	0.2	0.1	0.2

This unsatisfactory result requires explanations. One of them is that the filters have an uneven impact on the data sets. On the one hand, the filters removed different numbers of data points. For instance, in the 509 point data set the SNR = 40 dB filter removed 286 data points (56% of the original set). The SNR = 35 dB filter naturally removed fewer points - namely only 74 (15% of the original set). Without filtration, of course, no data points were removed. While the area of the removed data points was distributed over the remaining points, the different cleansing of the original measurement set impacted resulting mean sound power levels more than expected.

One could conclude that the filtration itself should have been omitted. However, the expanded uncertainties of the mean sound power levels were reduced significantly due to the filtration (Tbl. 6.3.2). Furthermore, the frequency responses of the resulting mean sound power levels - especially for the 1425 point grids - were drastically improved in quality by the filtration. This is most apparent when comparing the FFT mean sound power levels of the first and second 1425 point measurement (Fig. 6.3.5a - green and orange line, respectively). While the frequency response of the first 1425 point measurement succumbs to noise past 10 kHz, the response of the second 1425 point measurement continues to provide good results.

This is relevant as the SNR filter used on the first 1425 point measurement resulted in a less precise separation of signal versus noise measurements than the individualised filter used on the second 1425 point measurement (Fig. 6.2.3b vs. Fig. 6.2.4d). Hence, the filtered data from the first measurement still include a notable number of noisy points, which results in the noisiness of the mean sound power levels obtained from the Monte Carlo simulations. The filtered data from the second measurement provide the cleanest data of all five sets and show reliable mean sound power levels for the entire frequency range measured.

For the 509 point data set, the data cleansing effect was reduced because the distribution of the originally measured sound velocity levels was much cleaner than for the 1425 point measurements (Fig. 6.2.2a). Nonetheless, the filtered data sets of the 509 point measurement show an increase in mean sound power levels of approximately 1 dB. Most importantly though, they result in mean sound power levels that are within each other's coverage intervals for almost the entire frequency range (Fig. 6.3.5a - pink and

blue curve, Tbls. 6.3.1 - 6.3.2). Thus, filtration was needed.

The 509 point grid and 1425 point grids covered different surface areas. While the 509 point grid scanned a circular area with a radius of just under 6 cm (Fig. 6.2.2c), the 1425 point grids covered circular areas of radius 15 cm (Fig. 6.2.3c). Meanwhile, the radius of the piston remained constant of course. As, generally, the mean sound power levels of same sized grids are closer to each other than they are to mean sound power levels of the differently sized grids (Fig. 6.3.5), it was assumed that the variation in surface area measured was another contributor to differences in mean sound power levels. To confirm this, the same analyses were carried out for the piston surface only as this was the constant variable throughout measurements (Figs. 6.3.1 - 6.3.4, Tbls. 6.3.3 - 6.3.4). To do so, all data points that were located on the baffle, were removed. After this, the same filtration operations as previously were applied to the remaining points. For clarity, this analysis was omitted for the 509 point measurement with the SNR = 35 dB filter as its previous results were practically identical to those of the SNR = 40 dB filter (Tbl. 6.3.1).

In general, points on the piston surface were selected by comparing their distance to the grid's origin (as defined by the laser-scanning vibrometer reference grid) with the radius of the piston. If the radial distance was smaller than the piston radius, the point was assigned as on the piston surface. It is notable that while for some grids this identification of points on the piston surface worked very well (Fig. 6.3.1c), for others points on the edge of the piston were not identified correctly in all cases (Figs. 6.3.2b, 6.3.3b). The random factors that were used in the uncertainty modelling of the grid coordinates led to points being identified as on the piston surface even though they were not and vice versa. Furthermore, while the piston centre was positioned such that it coincided with the origin of the laser-scanning vibrometer reference grid, this placement was done manually and introduced a slight offset.

The only case for which a very clear distinction between piston and baffle points could be made, was the second 1425 point measurement. The individualised filter used on this data set created two distinct families of velocity level curves (Fig. 6.3.4c). Hence, for this grid a different strategy was used to define points on the piston surface. This definition was that the velocity level graphs of points on the piston surface had to belong to

the upper family of curves (Fig. 6.3.4d). The grid of the thusly defined piston surface confirmed that this method provided an accurate description (Fig. 6.3.4b).

Most notably however, the filtered first and second 1425 point measurements only scanned 42 and 56 points on the piston surface, respectively. The 509 point measurement included more than 100 such points. Thus, the increase in data points and surface area covered for the 1425 point grid actually corresponded to a lesser discretisation of the piston surface. This was not ideal.

For the unfiltered 509 point data set then, the piston only sound power level is slightly larger over the entire frequency range than the sound power output of the piston and baffle together (Fig. 6.3.1d). This is surprising as the opposite would have been expected. The result was corrected by filtering the measurement data with the SNR = 40 dB filter. After this, sound power levels for piston only and piston plus baffle union coincide (Fig. 6.3.2f). Considering the similarity of these two data sets after the implementation of the 200 Hz cut off frequency, this is the expected result (Figs. 6.3.2d - 6.3.2e).

For both 1425 point data sets, sound power levels for the piston only are smaller than those for the piston plus baffle union (Fig. 6.3.3f, 6.3.4e). While this conforms to the expectation that the baffle is a contributor to overall sound power levels, this result has to be regarded with caution as the ratio of measured points on the baffle versus on the piston was not favourable.

Looking at the one-third octave band mean sound power levels after the normalisation to piston surface, shows an improved degree of coincidence (Tbl. 6.3.3). Up to approximately 5 kHz, the one-third octave band mean sound power levels are now within approximately 0.6 dB of each other. Again, the expanded uncertainties for the filtered data sets are 0.1 dB except for two exceptions (Tbl. 6.3.4). For the unfiltered 509 point data set, the expanded uncertainties are slightly larger with a maximum of 0.3 dB.

Displaying the results graphically shows that the piston only FFT mean sound power levels are within each other's coverage intervals for large parts

of the frequency range (Fig. 6.3.6a). The only exception is the second 1425 point measurement which continues to result in slightly larger mean sound power levels than the other sets. However, the differences are significantly smaller than for the complete area comparison and within the coverage interval of the unfiltered 509 point measurement for selected frequency ranges (Fig. 6.3.6b).

In conclusion, this section showed that resulting sound power levels depend on the filtration. Different filtration strategies lead to statistically different results. This is not ideal but due to the quality of the measurement data.

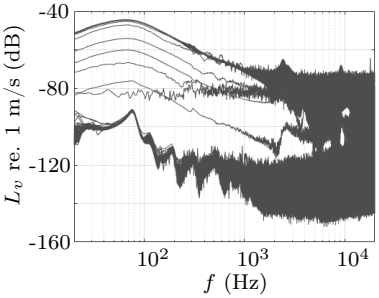

(a) Measured velocity levels for original grid.

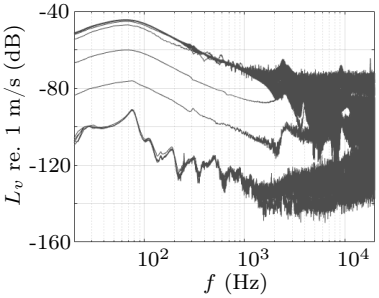

(b) Filtered velocity levels - piston only points.

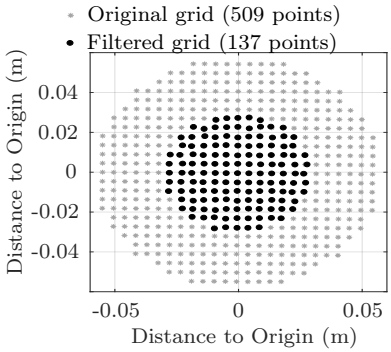

(c) Comparison of grids.

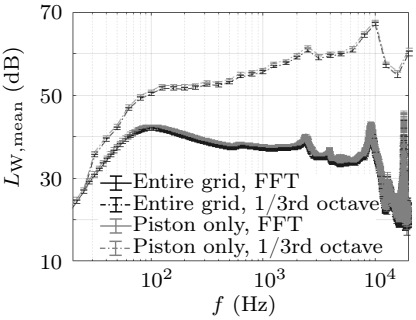

(d) Mean sound power levels.

Figure 6.3.1: 509 point measurement data without SNR filter. Comparison of mean sound power levels using either the entire grid or only points on the piston surface for its determination. $M = 1000$ for both cases.

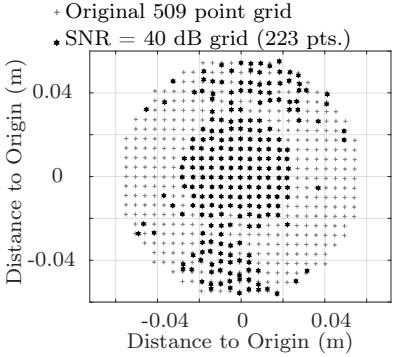

(a) Comparison of grids - original to SNR = 40 dB.

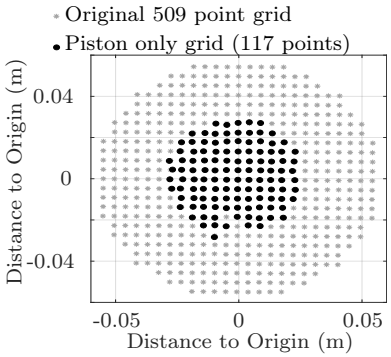

(b) Comparison of grids - original to piston only.

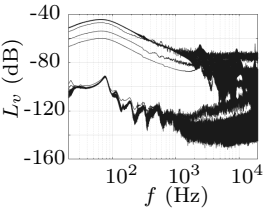

(c) Velocity levels under SNR = 40 dB filter.

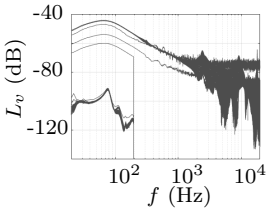

(d) SNR = 40 dB filtered velocity levels with cut off at 200 Hz.

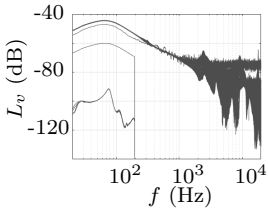

(e) Piston point velocity levels with cut off at 200 Hz.

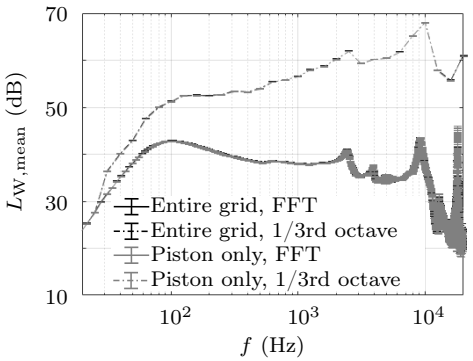

(f) Mean sound power levels.

Figure 6.3.2: 509 point measurement data with SNR = 40 dB filter. Comparison of mean sound power levels using either the entire grid (from Fig. 6.3.2d) or only points on the piston surface for its determination. M = 1000 for both cases. Velocity levels smaller than -60 dB at 200 Hz were cut off in order to provide cleaner results.

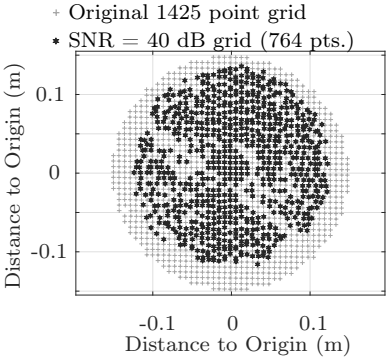

(a) Comparison of grids - original to SNR = 40 dB.

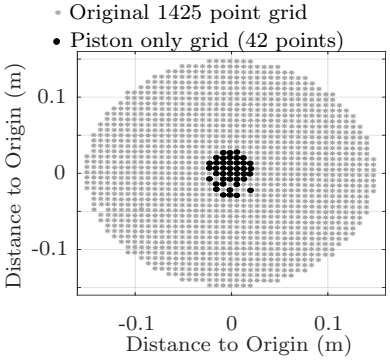

(b) Comparison of grids - original to piston only.

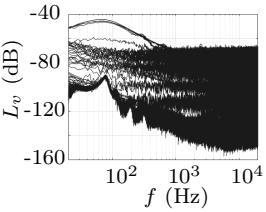

(c) Velocity levels under SNR = 40 dB filter.

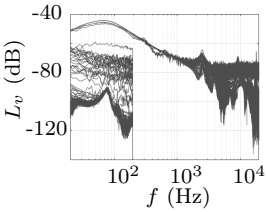

(d) SNR = 40 dB filtered velocity levels with cut off at 200 Hz.

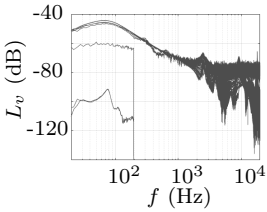

(e) Piston point velocity levels with cut off at 200 Hz.

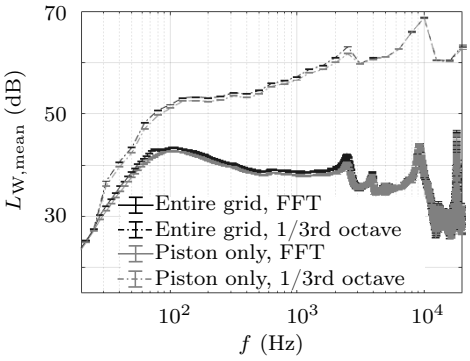

(f) Mean sound power levels.

Figure 6.3.3: 1425 point data from measurement 1 with SNR = 40 dB filter. Comparison of mean sound power levels using either the entire grid (from Fig. 6.3.3d) or only points on the piston surface for its determination. $M = 200$ for the entire grid and $M = 1000$ for the piston only analysis. Velocity levels smaller than -60 dB at 200 Hz were cut off.

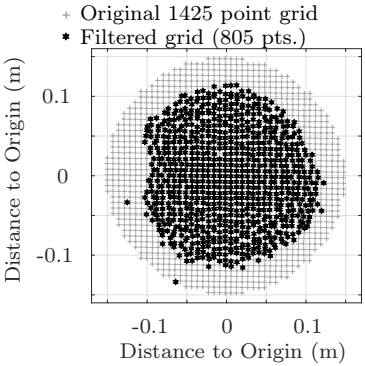

(a) Comparison of grids - original to frequency filtered one.

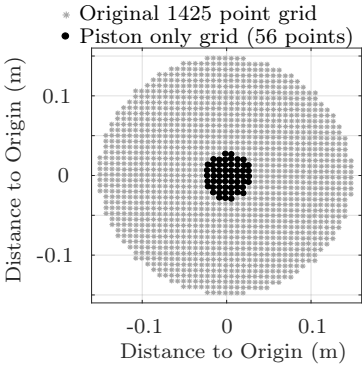

(b) Comparison of grids - original to piston only.

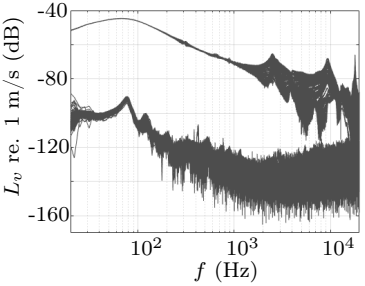

(c) Velocity levels after filtration.

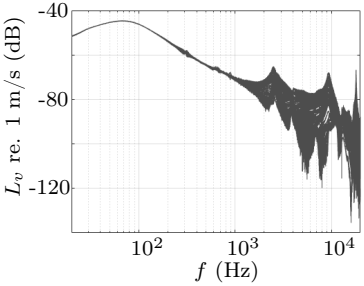

(d) Piston point velocity levels.

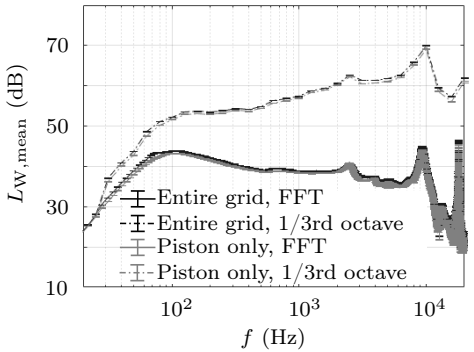

(e) Mean sound power levels.

Figure 6.3.4: 1425 point data from measurement 2 filtered at $f = 100$ Hz and $f = 1.5$ kHz. Comparison of mean sound power levels using either the entire grid or only points on the piston surface for its determination. $M = 212$ for the entire grid and $M = 1000$ for the piston only analysis.

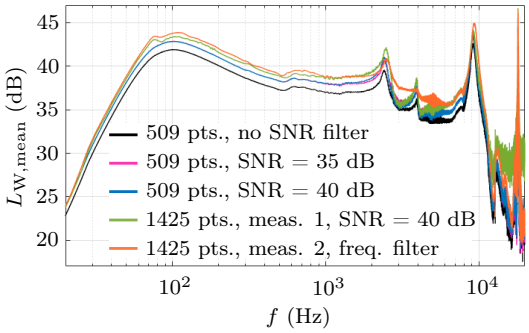

(a) Mean sound power levels of all grids in FFT.

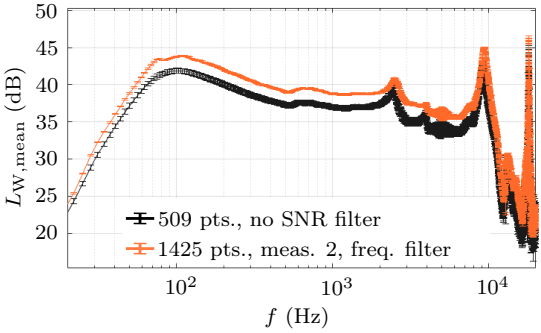

(b) Mean sound power levels with exp. uncertainties for grids with minimal and maximal values in the mid-frequency range.

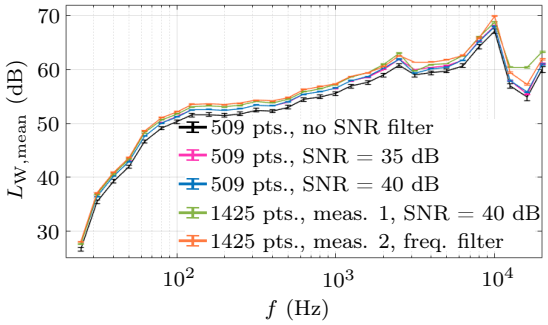

(c) Mean sound power levels incl. expanded uncertainties in 1/3rd octave bands.

Figure 6.3.5: Comparison of complete grid mean sound power levels in FFT and 1/3rd octave bands.

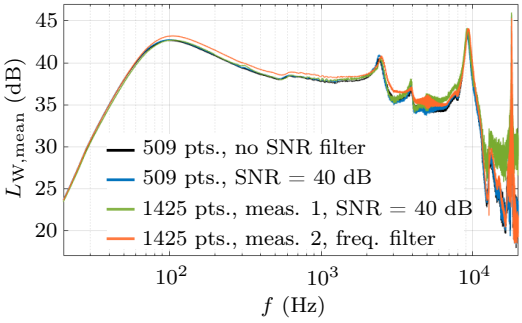

(a) Piston only mean sound power levels of all grids in FFT.

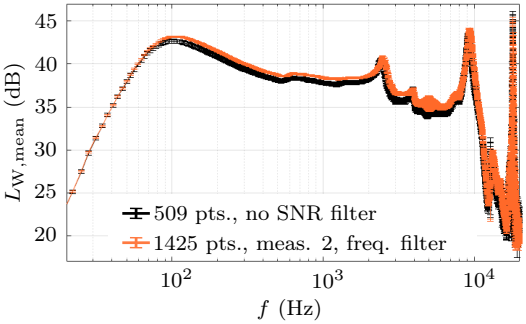

(b) Piston only mean sound power levels with exp. uncertainties for grids with minimal and maximal values in the mid-frequency range.

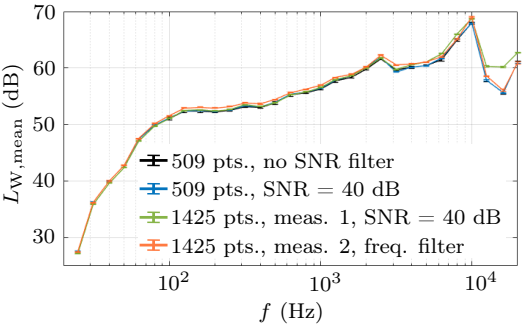

(c) Piston only mean sound power levels incl. expanded uncertainties in 1/3rd octave bands.

Figure 6.3.6: Comparison of piston only mean sound power levels in FFT and 1/3rd octave bands.

6.3.2 6V input voltage - comparison of results

From the results of the 5V input voltage measurements, it was concluded that sound power levels calculated by the discretised Rayleigh integral for each specific data set are very stable. This is especially true for data sets where noise measurements are excluded. However, systematic differences in mean sound power levels between the different data sets exist. At this point, it was not clear which mean sound power levels provided the most accurate representation of the emitted sound power. Ideally, the filter quality should correspond to correctness of obtained sound power levels. A comparison of the sound power levels from the current analysis with those obtained from standardised sound pressure and intensity measurements could provide further insight into this question and determine whether a realisation of the unit Watt with an uncertainty level of maximally 0.5 dB would be feasible.

Measurements in the sound field mainly used an input voltage of 6V for the shaker. As noted previously, laser vibrometer measurements were mainly carried out using an input voltage of 5V. For this reason, the previous discussion was based on these data. However, two measurements - one with 509 and one with 1425 data points - were carried out with the laser vibrometer and an input voltage of 6V. These will be the basis for the comparison with the standardised pressure and intensity measurements in the next chapter. Evidently, these measurement data were affected by the same sources of error as the 5V measurement. For this reason, analogous analysis routines including Monte Carlos simulations were applied to them in order to provide the best data possible for comparison (as described in Sec. 6.2.1). What remains to be shown here are results and filtration paradigms.

The unfiltered velocity level spectrogram of the 509 point measurement already provided a good basis for sound power determination as it showed a clear distinction between piston and baffle points (Fig. 6.3.7c). To further improve these base data, a SNR = 40 dB filter was used (see Sec. 6.2.1.1 for details) to cleanse the velocity spectrogram (Fig. 6.3.7d). The third sound power level calculation was then based on points on the piston surface only. Piston points were determined from the geometry data of the measurement, i.e. by defining points on the piston surface to be those points whose radial distance from the reference grid origin was less than the radius of the piston. It can be seen that the corresponding velocity level spectrogram also contains members from the lower family of curves

(Fig. 6.3.7e). These supposedly stem from baffle measurements, though. Their occurrence in the piston only analysis is likely due to points that are very close to the baffle - piston edge. As the reference grid was determined by the user of the laser-scanning vibrometer, its origin and the piston centre did not coincide perfectly. For this reason, the piston definition by grid coordinates was faulty for some edge points.

Comparing the resulting sound power levels in FFT (Fig. 6.3.7f) and one-third octave bands (Fig. 6.3.7g) shows that notable differences only exists at frequencies close to 3 kHz. The sound power levels from the filtered grids (Figs. 6.3.7a - 6.3.7b) are slightly lower at those frequencies than those from the unfiltered grid. The same is true in the frequency range between 100 Hz and 1 kHz. However, the sound power levels from the unfiltered grid are within the uncertainty limits of the filtered data sets for this frequency range.

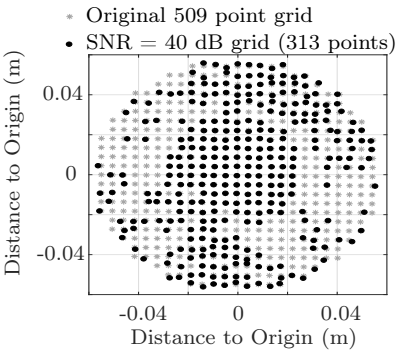

(a) Comparison of grids - original to SNR = 40 dB.

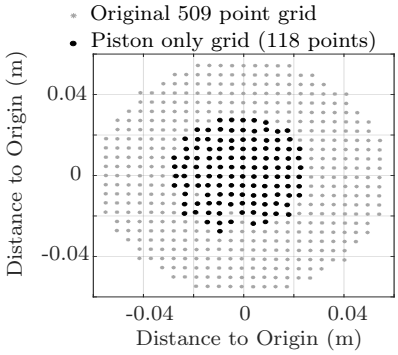

(b) Comparison of grids - original to piston only.

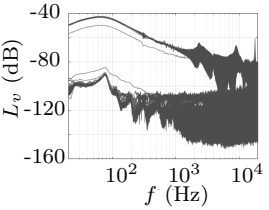

(c) Velocity levels without filter.

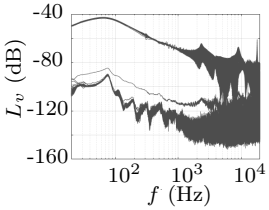

(d) SNR = 40 dB filtered velocity levels.

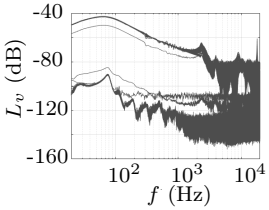

(e) Piston point velocity levels.

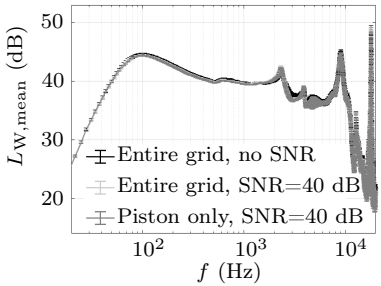

(f) Mean sound power levels in FFT.

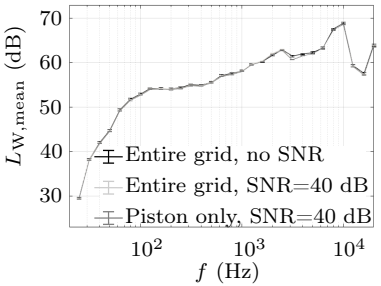

(g) Mean sound power levels in 1/3rd octave bands.

Figure 6.3.7: 509 point measurement data obtained with 6V input voltage using a SNR = 40 dB filter. Comparison of mean sound power levels using either the entire grid or only points on the piston surface for its determination. $M = 200$ for the entire grid and $M = 500$ for the piston only analysis.

The velocity level spectrogram of the 1425 point measurement clearly indicates a need for filtration as an abundance of noisy data points obscures the true data shape (Fig. 6.3.8). For the first data set, to obtain meaningful sound power levels without filtration, the same cut off frequency of 200 Hz as in the 5V analysis was used (Fig. 6.3.9c). This meant that velocity levels below -60 dB at 200 Hz, were artificially set to -500 dB from 200 Hz on. This avoided the removal of data points and retained measurement information up to 200 Hz.

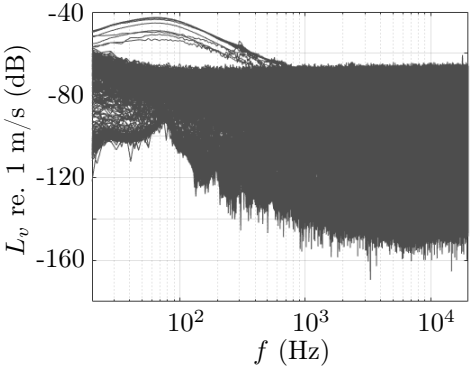

Figure 6.3.8: Measured velocity levels for 1425 point grid at 6V input voltage.

Considering the similarity to the 1425 point measurement at 5V input voltage, signal to noise filtration was achieved using the same individualised filter as for the second 1425 point measurement at 5V. This filter only allowed those points, i, to pass which fulfilled the following requirements:

$$L_{v,i} > \text{-50 dB at } f_1 = 100 \text{ Hz}$$
$$\textit{or}$$
$$L_{v,i} < \text{-125 dB at } f_2 = 1500 \text{ Hz}$$

As before, this individualised filter provided a very clean velocity level spectrogram and removed a minimal number of data points (Figs. 6.3.9a and 6.3.9d). The remaining data could then be used to calculate the second set of sound power levels.

The third and last data cleansing operation applied a further reduction in addition to the individualised filter. Only those data points with velocity levels curves belonging to the upper family of graphs were evaluated (Fig. 6.3.9e). These correspond to the piston surface, as expected (Fig. 6.3.9b). Defining the piston surface in this way - rather than the previously used geometric approach - provided a better distinction.

Looking at the corresponding sound power levels in FFT (Fig. 6.3.9f) and one-third octave bands (Fig. 6.3.9g) shows that results from all three sets coincide in the frequency range from 3 - 10 kHz. Below 3 kHz, sound power levels from the second data set - using the individualised filter - are larger than those based on the other data sets. At frequencies higher than 10 kHz, the piston only sound power levels are lowest while the sound power levels from the first data set (using only a cut off frequency) are highest.

Overall, the data quality in terms of velocity levels is best for the second data set, which used the individualised filter (Fig. 6.3.9d). However, it likely overestimates the emitted sound power as the area covered by removed data points was distributed over the remaining points. This artificially increased the sound emitting surface area. Omitting filtration and solely using a cut off frequency does not provide a good representation of true velocity levels either, though (Fig. 6.3.9c). Lastly, the third data set only contains information about piston points and, thus, lacks data about sound power contribution from the baffle (Fig. 6.3.9e). Hence, the three data sets cover a range of possible data enhancements without showing one clear ideal option.

In summary, the results from the measurements at 6V input voltage are congruent with those of the 5V input voltage. The uncertainty levels - based on Monte Carlo simulations - are small for all data sets. However, depending on the filtration used and size of surface area sampled, there are systematic differences in resulting sound power levels. These deviations are larger than the uncertainties associated with calculated sound power levels and it remains unclear which sound power levels represent the true ones most accurately.

Choosing one of the three data sets individually for comparison with data from sound pressure and intensity measurements could be considered

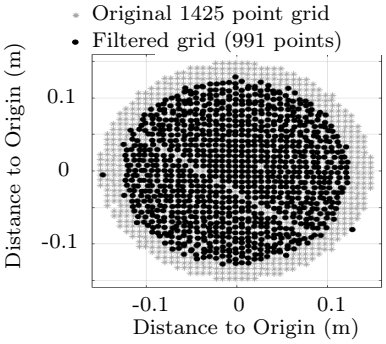

(a) Comparison of grids - original to filtered grid.

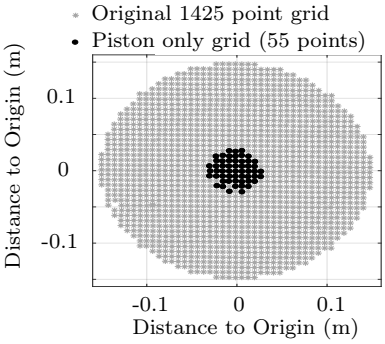

(b) Comparison of grids - original to piston only.

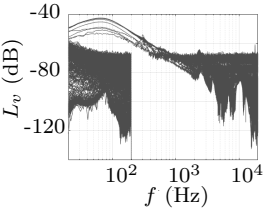

(c) Unfiltered velocity levels with cut off at 200 Hz.

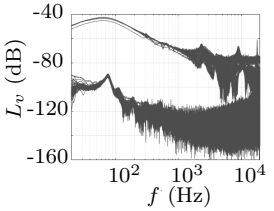

(d) Filtered velocity levels using an individualized filter.

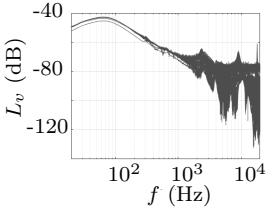

(e) Piston point velocity levels.

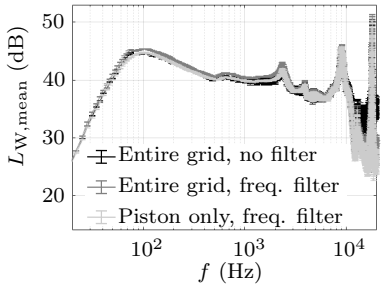

(f) Mean sound power levels in FFT.

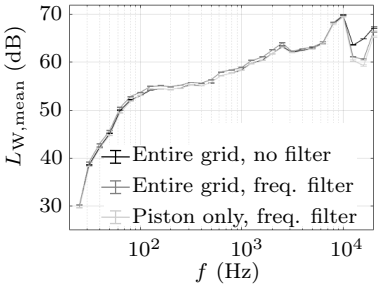

(g) Mean sound power levels in 1/3rd octave bands.

Figure 6.3.9: 1425 point measurement data with 6V input voltage and individualised signal to noise filter. Comparison of mean sound power levels using either the entire grid or only points on the piston surface for its determination. $M = 200$ for the entire grid and $M = 500$ for the piston only analysis.

random. Thus, the mean expected sound power level for the 1425 point measurement was calculated as mean of the sound power levels obtained from the three discussed data sets. To determine the associated uncertainty, minimal and maximal values of sound power levels were calculated for each frequency band and individual data set by adding or subtracting their associated expanded uncertainties. For each frequency band, the global minima and maxima of the three data sets defined a minimally and maximally expected sound power. The largest absolute difference between these minimal/maximal values to the expected mean sound power level was set to be its associated uncertainty. In this manner, both systematic differences as well as expanded uncertainties were taken into account.

The same procedure was applied to the 509 point measurement to obtain mean expected sound power levels as well as associated uncertainties in FFT and one-third octave bands (Fig. 6.3.10). These results, based on the discretised Rayleigh integral, could then be compared to sound power levels determined using standardised measurement procedures for sound pressure and intensity. The following chapter is devoted to this topic.

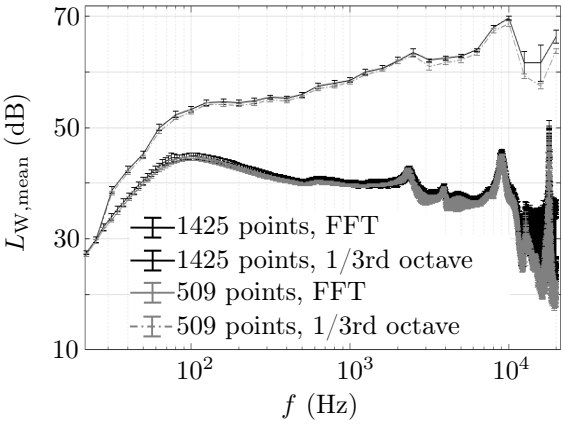

Figure 6.3.10: Combined discretised Rayleigh integral sound power levels of the two reference sets that will be used for comparison with those from sound pressure and intensity data. Depicted uncertainties include systematic differences due to filtration as well as expanded uncertainties.

7 | Comparison of Results from Rayleigh Integral, Sound Pressure and Sound Intensity Measurements

Reference measurements using standardised in-sound-field methods were performed both in the hemi-anechoic as well as in the reverberation room (see Sec. 3.1 for room descriptions). In the hemi-anechoic room, sound pressure and intensity measurements could be realised. The corresponding experimental set-ups were described previously (Sec. 3.2). For a thorough documentation, the reader is referred to the literature [5]. The hemi-anechoic room results for sound power levels from intensity and pressure measurements throughout this chapter were taken from this publication.

In the reverberation room, only sound pressure measurements were performed. These used six microphones and were carried out according to ISO 6926 [23]. They used the same multi-sine excitation signal as all other measurements with an input voltage of either 5V or 6V for the shaker. The surface area of the room including the diffuser measured 247 m^2.

7.1 Hemi-Anechoic Room

Measurements in the sound field used an input voltage of 6V exclusively. Hence, comparisons to laser-scanning vibrometer results are only possible for that input voltage. The derivation of the corresponding sound power levels using the discretised Rayleigh integral was shown in the previous chapter (Sec. 6.3.2). Thus, a comparison of results can be shown without further ado (Fig. 7.1.1).

Both, comparisons in FFT (Fig. 7.1.1a) as well as one-third octave bands (Fig. 7.1.1b), are shown. Sound power levels are displayed as mean values with corresponding uncertainty levels. For the in-sound-field results, these uncertainties were obtained from a dissemination analysis. The corresponding documentation can be found in [5]. The uncertainties displayed for the 1425 and 509 point grids from the discretised Rayleigh integral

computation were derived in detail previously (Sec. 6.3.2).

There are two aspects that are immediately apparent: the first one is that the uncertainties associated with the in-sound-field measurements of pressure and intensity are much larger than those of the Rayleigh integral analysis. This should be expected as one of the main advantages in the use of the discretised Rayleigh integral method is the avoidance of measurements in the sound field. Thus, this method is much less prone to errors which are due to distortions caused by imperfect sound fields or the presence of measurement equipment in the sound field.

The second conclusion that can be drawn from the sound power level comparison is that the mean sound power levels do not agree. While the mean sound power levels of the Rayleigh integral analysis are within the uncertainty limits of the corresponding in-sound-field levels, the reverse is not true. In fact, the mean sound power levels from the Rayleigh integral data are larger than the mean in-sound-field levels for almost the entire frequency range.

The closest agreement in sound power levels from the two approaches can be found by comparing those from the 509 point laser-vibrometer experiment with those from the sound pressure measurements. Conversely, the largest difference in sound power levels is given by comparing the data from the 1425 point laser-vibrometer measurement with those from the sound intensity measurement. These minimal and maximal differences were plotted for the one-third octave band analysis (Fig. 7.1.1c). Differences below 100 Hz can be attributed to the hemi-anechoic room, which does not provide a free field for these frequencies (see Sec. 3.1). The difference of one to two decibel in the frequency range from 100 Hz to 2 kHz is a systematic deviation, which cannot be explained by room characteristics, though.

In the 2.5 kHz one-third octave band, the Rayleigh integral sound power levels show a resonance which is displayed as anti-resonance by the in-sound-field data. The most likely explanation is an acoustic short-circuit between front and backside of the piston due to an air leakage at the piston edge. This would explain why the laser-scanning vibrometer detects larger piston movements, whereas the in-sound-field measurements are affected by an inversely phased source. More recent sources do not show these

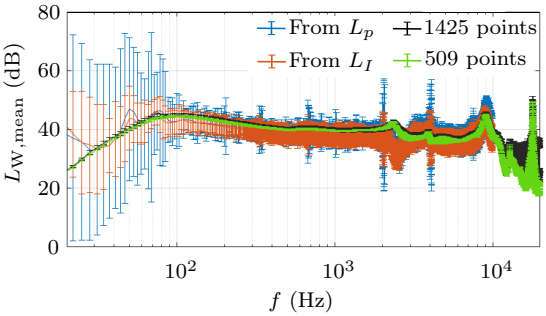

(a) Comparison of sound power levels in FFT.

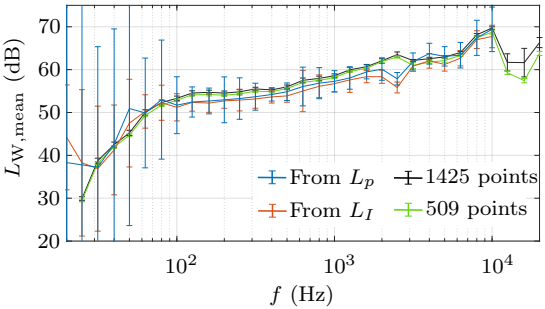

(b) Comparison of sound power levels in one-third octave bands.

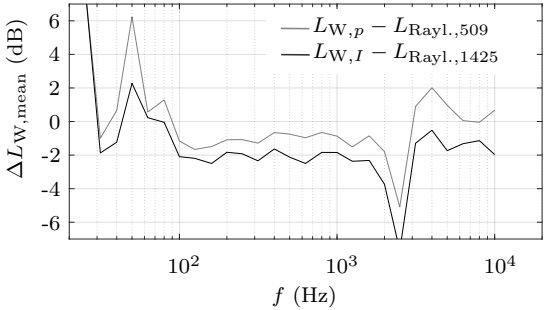

(c) Minimal and maximal difference between one-third octave band Rayleigh and in-sound-field power levels.

Figure 7.1.1: Comparison of sound power levels for Source 8 measured at 6V using in-sound-field or laser-vibrometer methods in the hemi-anechoic room. L_p refers to measured sound pressure levels, L_I to sound intensity levels. $L_{W,p}$ and $L_{W,I}$ denote the corresponding sound power levels. The uncertainties shown for the in-sound-field data stem from a dissemination analysis [5]. Numerical annotations in legend entries refer to grid sizes used for the Rayleigh integral analysis.

deviations, which strengthens this claim [32]. Beyond 3 kHz, the mean sound power levels resulting from all measurements show a much better level of agreement. Thus, it is mainly the frequency range from 100 Hz to 2 kHz which is a cause of concern.

7.2 Reverberation Room

In the reverberation room, measurements were performed at 5V as well as 6V input voltage. Within the sound field, only pressure measurements were performed. From the six distinct microphone positions that were used, sound power levels were determined according to ISO 6926 [23]. For all measurements, the same multi-sine excitation signal was used.

7.2.1 Comparison at 5V input voltage

Two distinct measurements with the laser-scanning vibrometer were performed at 5V input voltage. They both used 509 point grids. The data analysis was carried out in an analogous manner as previously (Sec. 6.3). Considering that the measured velocity levels provided a good distinction between baffle and piston points without significant influence of noise, no signal to noise filtration was utilised (Figs. 7.2.1c, 7.2.1e). For each one of the two measurements, sound power levels were calculated for both the individual 509 point data sets as well as for the piston only data sets. The corresponding grids as well as velocity level spectrograms are shown (Fig. 7.2.1).

Points on the piston surface were defined by their distance to the reference grid's centre. Those points, whose radial distance to the grid origin was smaller than the piston radius, were defined to be located on the piston surface. This distinction worked very well for the first measurement (Fig. 7.2.1d). For the second measurement, this selection method included two points whose velocity level spectrograms suggest that they, in fact, were located on the baffle (Fig. 7.2.1f). An offset between piston centre and origin of laser-scanning vibrometer reference grid is the most likely cause. Considering that this concerned two out of 182 points, no further action was taken as the influence of the two erroneous data points was assumed to be negligible.

Sound power levels were calculated using the discretised Rayleigh integral for each one of the four data sets - two measurements, piston only as well as complete grid for each case. To do so, Monte Carlo simulations were performed with $M = 200$ runs for 509 point data sets and $M = 500$ runs for piston only data sets. The same procedures for uncertainty determinations as explained previously were used for the Monte Carlo simulations (Sec. 6.2). The resulting mean sound power levels with corresponding expanded uncertainties ($k = 2$) were compared to the sound power levels that were determined from the sound pressure measurements using ISO 6926 (Fig. 7.2.2).

Overall, the same observations as for the hemi-anechoic room comparison were made (Sec. 7.1). Below 100 Hz, the reverberation chamber is not qualified for sound power determinations using pressure methods (see Sec. 3.1). Thus, differences in that frequency range can be attributed to the measurement environment. Between 100 Hz and 2 kHz, the same offset of one to two decibel, that was noted previously in the hemi-anechoic room, is also visible in the reverberation room data. This, again, shows a systematic difference which needs to be investigated in more detail. Furthermore, in the 2.5 kHz one-third octave band, the possible acoustic short-circuit that was seen in the hemi-anechoic room data can also be observed in the reverberation room results. This confirms that the inverse display of the resonance is a source and not room characteristic.

Between 3 and 10 kHz, the sound power levels from the in and out-of-sound-field measurements show a reasonable agreement. Beyond 10 kHz, mean velocity levels on the piston surface become very small and increasingly difficult to distinguish from noise. This makes accurate sound power determinations difficult. For this reason, differences in sound power levels beyond 10 kHz were not of primary concern at this point. Instead, the characteristic sound power level difference between vibrometer and pressure measurements in the frequency range from 100 Hz to 2 kHz was the main focus.

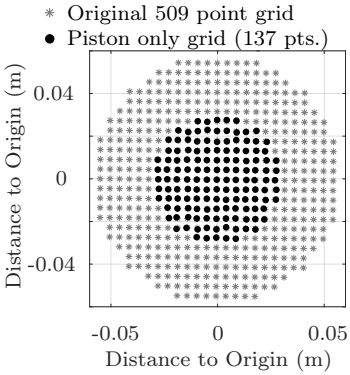

(a) Grids for first 509 point measurement.

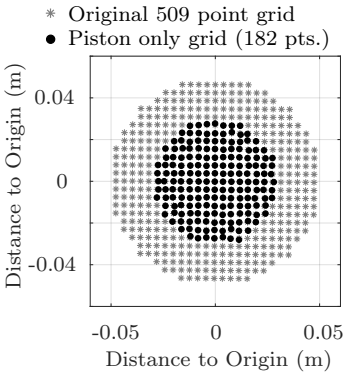

(b) Grids for second 509 point measurement.

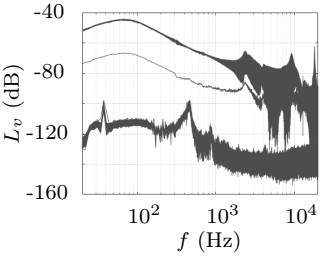

(c) Measured velocity levels for first 509 point set.

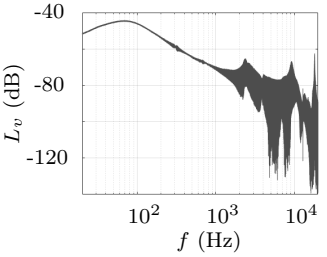

(d) Piston only velocity levels for first data set (137 points).

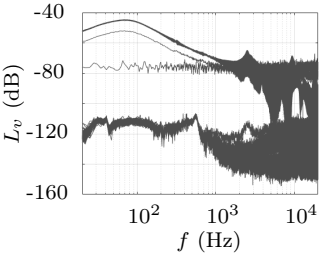

(e) Measured velocity levels for second 509 point set.

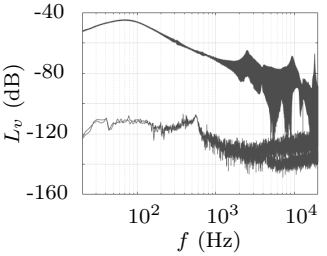

(f) Piston only velocity levels for second data set (182 points).

Figure 7.2.1: Overview over measurement data obtained from two 509 point data sets for Source 8 at 5V input voltage in the reverberation room.

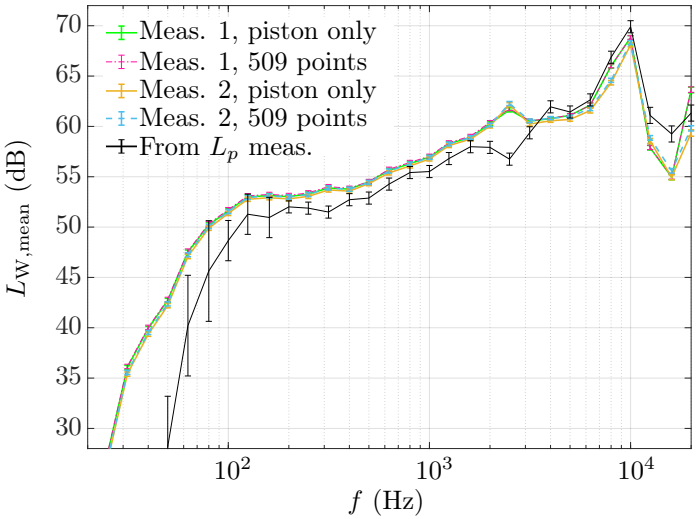

Figure 7.2.2: Sound power levels determined for Source 8 at 5V input voltage in the reverberation room.

7.2.2 Comparison at 6V input voltage

The same grid as was used for the second measurement at 5V, was also used for a measurement at 6V input voltage. The measured velocity levels are shown graphically (Fig. 7.2.3b). Analogous to the previous procedures, Monte Carlo simulations were performed for both the entire 509 point grid as well as for the piston surface only (Fig. 7.2.3a - 7.2.3c). The Monte Carlo simulations used the same boundary conditions as before (see Sec. 6.3) and numbers of runs of $M = 200$ for the entire grid as well as $M = 500$ for the piston only analysis. No signal to noise filtration was utilised.

In order to obtain one single set of mean sound power levels with associated uncertainties to represent the 6V reverberation room measurement (comparable to Fig. 6.3.10), the same procedure as previously was applied (Sec. 6.3.2). Thus, the mean sound power level was defined as average of the mean sound power levels from the individual analyses of the entire and piston only data sets. To determine the overall uncertainty, the upper and lower limits of the individual 509 point and piston only data sets were determined. The largest absolute difference of these boundaries to

the overall mean sound power level determined the overall uncertainty associated with the mean sound power level. In this way, the individual expanded uncertainties ($k = 2$) of the 509 point and piston only analysis were completely covered by the denoted uncertainty. Determination of the uncertainty in this way is a conservative approach as it can be expected to cover an interval corresponding to $k > 2$. However, as the uncertainty levels continued to be very small, no further insight would have been gained by a refinement of the uncertainty determination.

The resulting mean sound power levels with corresponding uncertainties were calculated for FFT and one-third octave bands (Fig. 7.2.3d). These could be compared to sound power levels calculated from sound pressure measurements according to ISO 6926 based on the same six microphone positions as were used for the 5V measurements (Fig. 7.2.4).

As expected, the results are comparable to those from the measurement at 5V. Again, the characteristic level difference of one to two decibel between 100 Hz and 2 kHz is visible. At 2.5 kHz, the inversely shaped resonance is also apparent. Beyond 3 kHz, there is, as before, a better agreement between sound power levels with those from the in-sound-field method over-shooting those from the out-of-sound-field measurement.

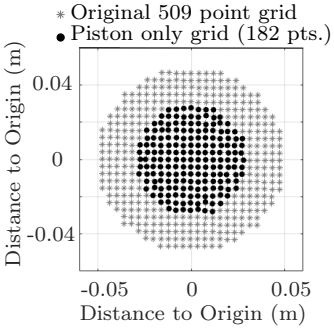

(a) Comparison of complete 509 point and piston only grid.

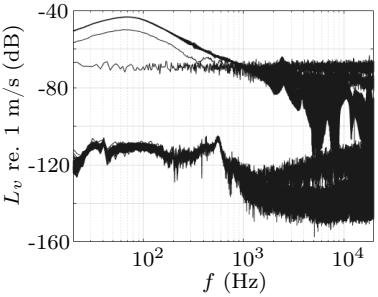

(b) Measured velocity levels for 509 point grid.

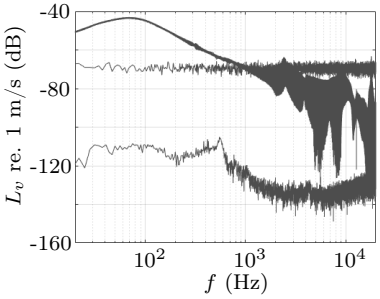

(c) Velocity levels of piston points only (182 points).

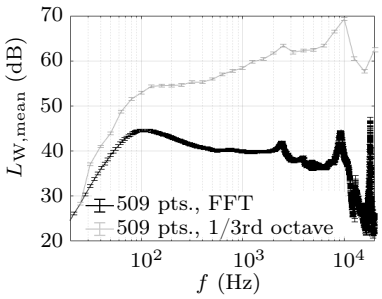

(d) Mean sound power levels with associated uncertainties from Monte Carlo simulations in FFT and 1/3rd octave bands.

Figure 7.2.3: Determination of sound power levels for Source 8 at 6V input voltage in the reverberation room using the discretised Rayleigh integral.

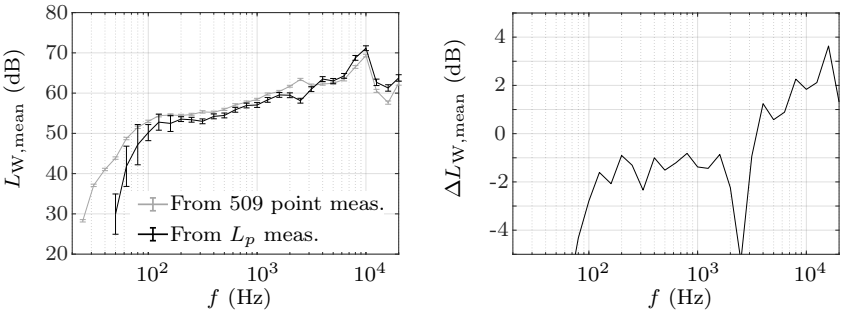

(a) Mean sound power levels with associated uncertainties.

(b) Sound power level from pressure measurements referenced to that from laser-vibrometer scans.

Figure 7.2.4: Comparison of sound power levels for Source 8 measured at 6V using in-sound field or laser-vibrometer methods in the reverberation room.

7.3 Inter-Room Comparison

For a comprehensive overview over the results from in and out-of-sound-field methods in the hemi-anechoic and reverberation room, all results from the respective 6V measurements were plotted (Fig. 7.3.1). One could say that the in and out-of-sound-field results form two distinct cohorts. Generally, mean sound power levels determined by use of the same method (pressure measurement or laser-scanning vibrometer measurement) agree. This also holds true for the two distinct environments - hemi-anechoic and reverberation room. These methods are, thus, stable. As intensity measurements were performed only in the hemi-anechoic room, no conclusion for stability can be made for its results.

The in-sound-field methods using pressure or intensity measurements show an anti-resonance in the 2.5 kHz one-third octave band, whereas the newly proposed out-of-sound-field method using laser-scanning vibrometry shows a resonance peak in that frequency band. As discussed previously, this inverse sound power level behaviour is most likely attributable to an acoustic short-circuit at the piston-baffle border (Sec. 7.1). This affects in-sound-field measurements as occurrence of an inversely phased sound source, while out-of-sound-field measurements detect stronger surface motion. As

such, the sound power level behaviour in the 2.5 kHz one-third octave band is characteristic for in and out-of-sound-field methods.

Below 100 Hz, the measurement environments are not qualified for sound power level determinations. Hence, no conclusions can be drawn and uncertainties associated with the in-sound-field methods are extraordinarily large. This is a main advantage of the out-of-sound-field measurement as, in theory, it has no lower frequency limit for its usability and validity. Beyond 3 kHz then, sound power levels from the in-sound-field measurements over-shoot those from the out-of-sound-field data. The best agreement in results can be seen in the frequency range from 3 to 10 kHz. Past 10 kHz, the wavelength of the emitted sound waves starts to become smaller than the piston radius of Source 8 - which was used to derived these results. At the same time, the surface motion of the piston becomes increasingly non-uniform with smaller displacements and movement velocities but larger gradients. This is a challenge for laser-vibrometer measurements and places an emphasis on sufficient discretisation as well as signal to noise ratios. It is possible that in the future a need to use two different primary sound sources to cover the frequency range from 20 Hz to 20 kHz will be defined.

Remaining then is the frequency range from 100 Hz to 2 kHz. In this range, a difference of one to two decibel can be seen between the in and out-of-sound-field methods. This is an undesired outcome as it speaks of a systematic difference between results. While the differences in sound power levels in the other frequency ranges could be attributed to a lack of perfection of the current primary source prototype, the systematic differences in sound power levels between 100 Hz and 2 kHz indicate a more fundamental error.

Moreover, it makes a sound power level determination with an uncertainty level of within 0.5 dB impossible. Decreasing associated uncertainties of determined sound power levels as well as designing a method to measure them below 100 Hz were the main goals in the development of a primary standard. Seeing that the general shapes of the sound power level spectrograms agree for all methods and environments is, thus, a strong result. It indicates that the newly proposed method using laser-scanning vibrometry has the potential to eliminate in-sound-field measurements. However, it is indispensable to detect the source of the 1-2 dB sound power level

difference for the 100 Hz to 2 kHz frequency range to reach that goal. For this reason, two possible explanations will be elaborated in the remainder of this chapter.

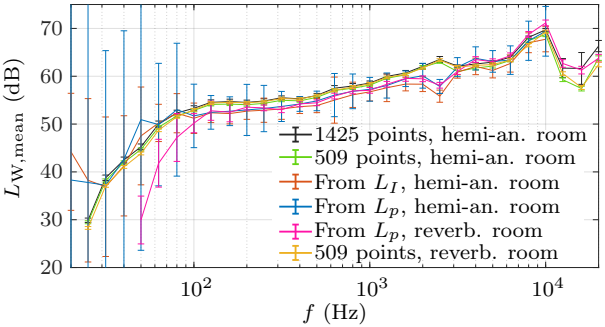

(a) Mean sound power levels for 20 Hz $\leq f \leq$ 20 kHz.

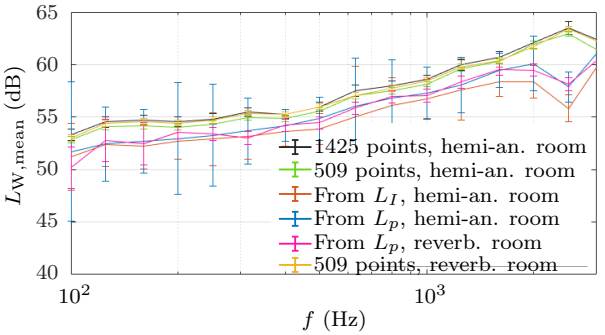

(b) Focused view on 100 Hz $\leq f \leq$ 3 kHz.

Figure 7.3.1: Sound power levels determined for Source 8 at 6V input voltage in varying rooms and with different methods.

7.4 Possible Explanations for Differences in Sound Power Levels

7.4.1 Tilting movement of piston

During measurements the observation was made that in some cases the piston does not move straight up and down but rather moves in a tilted fashion (see Fig. 5.2.16b). To evaluate the significance of this behaviour, it was assumed that, aside from the tilt, the piston moves as a rigid piston. The level of tilt was prescribed by adjustments on the velocity levels (Fig. 7.4.1a). Namely, a maximum level difference, ΔL_v, in velocity across the piston surface was prescribed and the according velocity level calculated for each point on the piston surface. Sound power levels were then calculated using the discretised Rayleigh integral for different cases corresponding to $kr = 0.1$, $kr = 1$ and $kr = 10$. Here, the angular wave number, k, is a measure for the number of waves per unit of measure. In the same medium small values of kr correspond to low frequencies or small pistons and large values of kr to large frequencies or large pistons.

The results show that for small kr, a tilting motion of the piston does not alter sound power levels significantly (Fig. 7.4.1b). In this comparison, significant differences in sound power levels of up to 1 dB can be observed only for $kr = 10$. For Source 8 with its radius of $r = 0.03$ m, however, $kr = 10$ corresponds to a frequency of $f \approx 18$ kHz. Hence, the tilting motion of the piston cannot explain the differences in sound power levels between the in and out-of-sound-field methods between 100 Hz and 2 kHz.

Generally, it should be noted that - for set-ups that are similar to the one utilised here - emitted sound power levels are calculated correctly by the Rayleigh integral also for tilting pistons. Special care on avoiding tilting motion of the piston is only necessary if an inadequate number of sampling points is used or much larger pistons or higher frequencies are of interest.

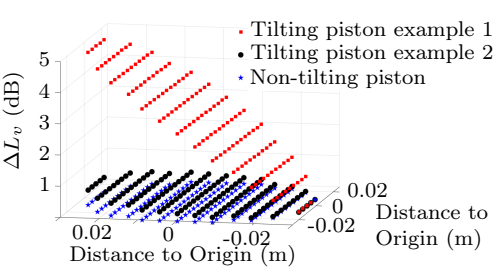

(a) Schematic of pistons moving in a tilted fashion.

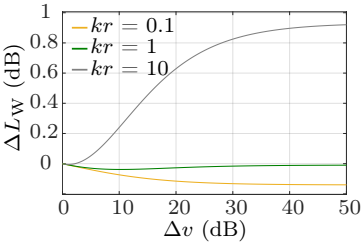

(b) Sound power level of tilting pistons referenced to a non-tilting one.

Figure 7.4.1: Analysis on influence of tilting piston movement.

7.4.2 Deviation from planar radiator assumption

One of the main assumptions of the discretised Rayleigh integral is that the radiator and baffle surface form a perfectly planar surface. This is true while the piston is at rest. However, as soon as the piston is excited, its motion creates a ledge between piston edge and baffle. While the baffle surface remains in the base horizontal plane, the piston surface undergoes motions in vertical direction. This creates an offset between the surfaces. For points on the piston edge this is especially critical. To represent this ledge-effect graphically, the maximal vertical displacement of points whose radial distance to the piston centre was just smaller (black) or just larger (grey) than the piston radius were plotted (Fig. 7.4.2). Points that were falsely identified as on or off the baffle are due to a slight offset of the piston centre from the coordinate axis origin.

In principle, the assumption was that the size of this ledge is so small that it does not impact sound power levels. However, more recent sources, which avoid the occurrence of an abrupt offset in the vertical direction by keeping the piston edge in plane with the baffle surface, show an agreement in sound power levels especially for the desired frequency range (100 Hz - 2 kHz) [32]. Hence, it is at least possible that the ledge effect is larger than expected.

If this really were the case, then points on the piston edge could be thought of as effectively emitting sound into three-quarter of a spherical volume,

whereas points that are on the baffle edge, conversely, would emit sound into only one-quarter of a spherical volume. In the discretised Rayleigh integral, sound emission into a hemisphere is characterised by the use of $\Omega_0 = 2\pi$ in the denominator of the pre-factor. To remind the reader of the complete discretised Rayleigh integral formulation, it is repeated below (Eq. 2.3.1). Consequently, sound emission into three- and one-quarter spheres could be modelled by using values of $\Omega_0 = 3\pi$ and $\Omega_0 = 1\pi$, respectively.

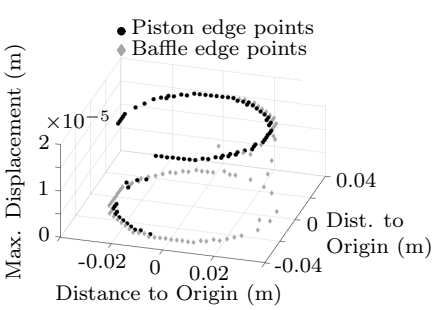

(a) $f = 50$ Hz.

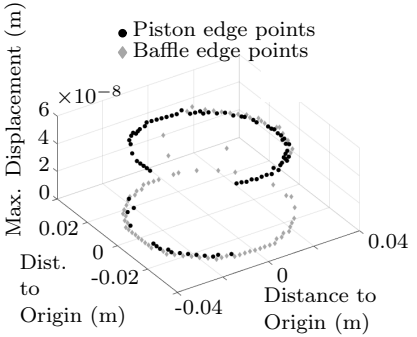

(b) $f = 1$ kHz.

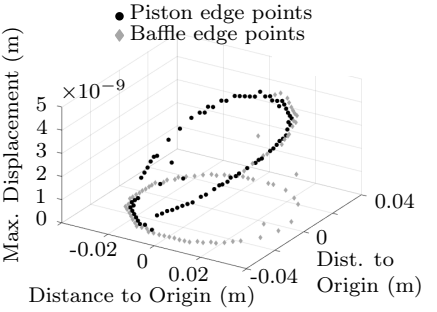

(c) $f = 10$ kHz.

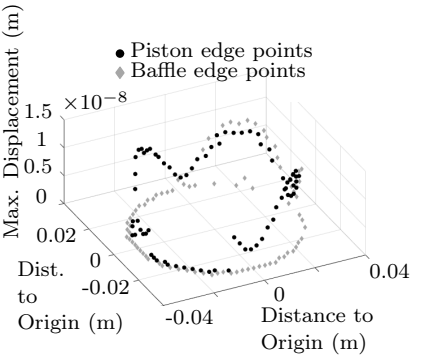

(d) $f = 18$ kHz.

Figure 7.4.2: Displacement of points along piston-baffle border at selected frequencies.

$$P_{\text{Rayleigh}} = \sum_{i=1}^{N} \frac{\rho_0 c}{2\pi} k^2 \tilde{v_i}^2 S_i^2 + \\ + 2 \sum_{i=1}^{N} \sum_{j=i+1}^{N} \frac{\rho_0 c}{2\pi} k^2 \tilde{v_i} \tilde{v_j} S_i S_j \frac{\sin(kd_{ij})}{kd_{ij}} \cos(\phi_i - \phi_j) \tag{2.3.1 revisited}$$

This would effectively require splitting up the sound power calculation into three parts in order to implement the double summation:

- points, that are neither baffle nor piston edge points: $\Omega_0 = 2\pi$
- points on the piston edge: $\Omega_0 = 3\pi$
- points on the baffle edge: $\Omega_0 = 1\pi$

Such a procedure would require establishment as well as detailed investigations on its scientific validity. As these would exceed the scope of this work, they are omitted here. However, the deviation from one of the fundamental assumptions, which the discretised Rayleigh integral is based on - even if ever so slight - could be an explanation for the sound power level differences observed. As such, it should be further investigated in the future using appropriate methods (numerical or experimental).

8 | Summary and Future Prospects

Looking at all of the results of this work, a realisation of the unit Watt in airborne sound is realistic. Even more so, this statement is true for frequencies smaller than 100 Hz, with no obvious physical limitation determining a lower frequency limit. All current international standards rely on in-sound-field measurements and, thus, are limited by measurement room characteristics. For the rooms used in this work, the physical limit was imposed at approximately 100 Hz. Establishing the possibility to develop a standardised method also for the low frequency range, with its growing importance especially in urban planning, is a major improvement over the current state of the art.

Unfortunately, the primary standards that were used for this work lack the desired accuracy (Chp. 7). However, differences in sound power levels between those obtained from the discretised Rayleigh integral method and those obtained from standardised methods are constant values for large parts of the frequency range considered. These level differences are in the range of up to 2 dB. Both of these aspects together indicate that, fundamentally, the method works. They also indicate that a design or measurement flaw exists, which has yet to be uncovered and validated.

Nonetheless, the utilised measurement method using laser-scanning vibrometry and post calculation of sound power levels by means of the discretised Rayleigh integral shows very good results in terms of precision (Chp. 6). The uncertainties associated with sound power levels obtained from this method are very small, especially if compared to those that result from the use of standardised methods. This is a crucial result, making the establishment of a primary standard for sound power with an uncertainty level of 0.5 dB feasible. These small uncertainties are connected to the convergence of the discretised Rayleigh integral. Demonstrating this convergence for the ideal case of a rigid piston as well as for the first three Eigenmodes is another result of this work. Most importantly, guidelines for the choice of adequate discretisations have been defined (Chp. 5).

Considering all of these aspects as a whole gives rise to the claim that the methodology proposed here is suitable for the development of a primary standard for sound power. The lack of accuracy of the physical realisations

of primary standards investigated in this work then shows the direction for future work. One aspect to be considered is the radius of the piston used. The primary sources documented here featured piston radii of $r \leq 0.05$ m. When excited at frequencies larger than 10 kHz, the increasingly subdivided motion on the piston surface led to large displacement gradients for these fairly small sized pistons. In theory, the resolution of any surface shape should be possible under consideration of appropriate minimal discretisations as discussed in this work (Chp. 5). For the experimental case practical considerations such as the diameter of the laser beam are relevant. More recent work does indicate that larger sized pistons with smaller surface velocity gradients show increased levels of accuracy [32] .

Extending the discussion on piston radii, a consideration could be to use two different pistons to cover the frequency range from 20 Hz to 20 kHz. From their emission characteristics, it would be advisable to use larger sized pistons for the lower frequencies and smaller sized pistons for the higher frequencies (Chp. 4). However, from the previous discussion on surface velocity gradients, the opposite would be true. Attempting to strike this balance for a more narrow frequency range rather than the entire 20 Hz - 20 kHz spectrum could be another approach for the future.

One main aspect in the discussion about the uncertainty of the calculated sound power levels was that of data quality (Chp. 6). This is certainly a major factor for future measurements. While the results shown in this work suggest that increases in data quality do not improve accuracy to the same extent, they do allow for easier data analysis and increased precision. Ideally, the lengthy discussion on signal to noise filtration that was presented in this work would be without necessity in the future. To improve data quality, the approach that immediately follows from this work is to re-think the distribution of measurement points on the piston surface versus on the baffle surface. While the main approach in this work was to use uniformly distributed data points, it would be worth consideration to retain the uniform distribution per material surface but to choose different point densities. A suggestion would be to use a high density uniform distribution on the piston surface while using a lower density distribution on the baffle surface. This would increase refinement on the piston surface while maintaining a balance between points on the piston versus points on the baffle.

Naturally, site specific improvements, for instance on the excitation signal (as reported in [32]) or positioning of the laser-scanning vibrometer could be thought of. However, they are also to be considered as factors increasing precision. There is no indication that these could solve the underlying accuracy problem. To gain a deeper understanding of the inaccuracy, the suggestions following directly from this work would be to investigate the ledge effect in more detail (Sec. 7.4.2). The effect that the deviation from the in-plane assumption of baffle and piston has is without numerical value at this point. A frequency-wise discussion seems worthwhile. This investigation could be an excellent example for numerical modelling; an aspect which has been held very basic in this work. In fact, extensive numerical modelling using finite or boundary elements would be strongly encouraged to validate results.

Lastly, a round robin experimental series at different institutes could be conducted. This would ideally include more than one physical realisation of the primary standard. This project was embedded into a joint European research project. As such, further primary standards have been developed at partner institutes [27]. However, each of these primary standards was only tested at the institute where it was developed. Thus, it would be a very insightful task to test as many of these standards as possible in different measurement environments. This would have the very real potential to provide the missing link to the open inaccuracy question.

If the accuracy question can be solved, which seems realistic, a both precise and accurate primary standard for sound power will exist. The proof of principle for its measurement method has been given in this work. While there are, as could be expected, still open questions, this work provides a first link for a scientifically valid traceability chain for the measurand sound power, which - when connected - will give validation to the major quantity in acoustic regulations.

Bibliography

[1] Andersson, H., Wittstock, V. 'Traceable sound power measurements in essentially diffuse or free fields'. In: *Proceedings of InterNoise*. Hamburg, Germany, 2016.

[2] Arendt, I., Kurtz, P. 'Reasons justifying a revision of the existing sound power measurement standards'. In: *Proceedings of InterNoise*. Hamburg, Germany, 2016.

[3] Arina, R., Völkel, K. 'Numerical Modelling of the Primary Source in a Hemi-Anechoic Room'. In: *Proceedings of InterNoise*. Hamburg, Germany, 2016.

[4] Bietz, H., Wittstock, V., Brezas, S. 'Investigation on the Suitability of an electroacoustic Sound Source as secondary Sound Power Standard'. In: *Proceedings of InterNoise*. Hamburg, Germany, 2016.

[5] Brezas, S. 'Investigation on the dissemination of the unit watt in airborne sound and applications'. Doctoral Thesis. RWTH Aachen University, Institut für Technische Akustik, 2019.

[6] Brezas, S., Cellard, P., Andersson, H., Guglielmone, C., Kirbas, C. 'Dissemination of the unit Watt in airborne sound: aerodynamic reference sound sources as transfer standards'. In: *Proceedings of InterNoise*. Hamburg, Germany, 2016.

[7] Cellard, P., Andersson, H., Brezas, S., Wittstock, V. 'Automatic sound field sampling mechanisms to disseminate the unit watt in airborne sound'. In: *Proceedings of InterNoise*. Hamburg, Germany, 2016.

[8] Deutsche Gesellschaft für Akustik e.V. 'DEGA-Empfehlung 101 Akustische Wellen und Felder'. Berlin, Germany: Deutsche Gesellschaft für Akustik e.V., Mar. 2006.

[9] Fabris, C. 'New Noise Sources in Urban Areas'. In: *Proceedings of Internoise*. New York City, USA, Aug. 2012.

[10] Fasold, W., Kraak, W., Schirmer, W. *Taschenbuch Akustik*. .1. VEB Verlag Technik Berlin, Germany, 1984.

[11] Feizelmeier, I. 'Körperschallquelle mit einstellbarer mechanischer Quellimpedanz'. Diploma Thesis. Physikalisch Technische Bundesanstalt, 2007.

[12] Gerlach, A. 'Ein Beitrag zur Erweiterung und Anwendung der Direkten Finiten Elemente Methode zur Bestimmung der abgestrahlten Luftschalleistung dreidimensional ausgedehnter Körperschallquellen'. Doctoral Thesis. Universität Stuttgart, Institut für Thermische Strömungsmaschinen und Maschinenlaboratorium, 2000.

[13] Guglielmone, C., Wittstock, V., Kirbas, C., Andersson, H. 'Main achievements of the EMRP sound power project and future prospects'. In: *Proceedings of InterNoise*. Hamburg, Germany, 2016.

[14] Hoffmeyer, D., Jakobsen, J. 'Sound insulation of dwellings at low frequencies'. In: *Journal of low frequency noise, vibration and active control* 29.1 (2010), pp. 15–23.

[15] Hopkins, C. *Sound Insulation*. 1st ed. Elsevier Ltd., 2007, pp. 42–43.

[16] Hübner, G. 'Eine Betrachtung zur Physik der Schallabstrahlung'. In: *Acustica* 75 (1991), pp. 130–144.

[17] Hübner, G. 'Maschinenakustik A Grundlagen / Schallabstrahlung'. Script. Universität Stuttgart, Institut für Thermische Strömungsmaschinen und Maschinenlaboratorium, Germany, 2000.

[18] Hübner, G., Gerlach, A. 'Zusammenhang der DFEM-Schallleistungsbeschreibung mit der Rayleighschen Schallfelddarstellung ebener Strahler'. In: *Proceedings of DAGA 1998*. Zürich. 1998.

[19] Hübner, G., Hupfeld, J., Kandelaki, D., Baena, R., Rodrigues, M., Staschke, J., Weinig, S. *Spezielle Probleme bei der Geräuschemissionsmessung von Maschinen. Forschung Projekt F 1989*. Tech. rep. Bundesanstalt für Arbeitsschutz und Arbeitsmedizin, 2008.

[20] Hübner, G., Kienzle, B., Wittstock, V., Gerlach, A. 'DFEM-Schallleistungsbestimmung an frei schwingenden Streifenstrahlern'. In: *Proceedings of DAGA 2001*. Hamburg, Germany, 2001.

[21] ISO 3740:2000. 'Determination of sound power levels of noise sources - Guidelines for the use of basic standards'. Standard. 2000.

[22] ISO 3745:2012. 'Determination of sound power levels and sound energy levels of noise sources using sound pressure - precision methods for anechoic and hemi-anechoic rooms'. Standard. 2012.

[23] ISO 6926:1999. 'Acoustics - Requirements for the performance and calibration of reference sound sources used for the determination of sound power levels'. Standard. 2001.

[24] JCGM 100:2008. ‘Evaluation of measurement data — Guide to the expression of uncertainty in measurement’. Joint Committee for Guides in Metrology (JCGM). BIPM, 2008.

[25] JCGM 101:2008. ‘Evaluation of measurement data — Supplement 1 to the "Guide to the expression of uncertainty in measurement" — Propagation of distributions using a Monte Carlo method’. Joint Committee for Guides in Metrology (JCGM). BIPM, 2008.

[26] JCGM 200:2012. ‘International vocabulary of metrology – Basic and general concepts and associated terms (VIM)’. 3rd ed. Joint Committee for Guides in Metrology (JCGM). BIPM. 2012.

[27] Kirbas, C., Andersson, H., Guglielmone, C., Wittstock, V., Bilgic, E. ‘Primary sound power sources for the realisation of the unit watt in airborne sound’. In: *Proceedings of InterNoise*. Hamburg, Germany, 2016.

[28] Kraus, M. ‘Ein Beitrag zur Bestimmung der von dreidimensionalen Körperschallquellen abgestrahlten Luftschallleistung mit der Direkten Finiten Elemente Methode’. Doctoral Thesis. Universität Stuttgart, Fakultät Maschinenbau, 2007.

[29] Lenk, A., Pfeifer, G., Werthschützky, R. *Elektromechanische Systeme*. 1st ed. Springer, 2001, pp. 284–287.

[30] Lerch, R., Sessler, G., Wolf, D. *Technische Akustik: Grundlagen und Anwendungen*. Springer-Verlag Berlin Heidelberg, 2009, pp. 400–402.

[31] Moller, H., Sejer Pedersen, C. ‘Low-frequency noise from large wind turbines’. In: *Journal of the Acoustical Society of America* 129.6 (2011), pp. 377–3744.

[32] Picker, K., Wittstock, V. ‘Zum aktuellen Stand der Entwicklung primärer Schallleistungsquellen an der PTB’. In: *Proceedings of DAGA 2019*. Rostock, Germany, 2019.

[33] Rieger, W. ‘Entwicklung eines Meßverfahrens zur Bestimmung der abgestrahlten Luftschalleistung ebener Strahler auf Grundlage der DFEM’. Doctoral Thesis. Universität Stuttgart, Institut für Thermische Strömungsmaschinen und Maschinenlaboratorium, 1997.

[34] Schirmer, W., ed. *Technischer Laermschutz*. Springer-Verlag Berlin Heidelberg, 2006, pp. 35–47.

[35] TIRA Maschinenbau GmbH. ‘Technische Dokumentation Schwingerreger TIRAvib S502’. Manual. Schalkau, Germany, 2002.

[36] Völkel, K., Bethke, C., Brezas, S., Wittstock, V. 'First results in the realization of the unit Watt in airborne sound'. In: *Proceedings of Internoise 2014*. CDROM. Melbourne, Australia, 2014.

[37] Völkel, K., Schmelzer, M., Guglielmone, C., Arina, R., Wittstock, V. 'Analytical study on the sound field generated by a baffled vibrating structure'. EMRP JRP SIB56 SoundPwr Deliverable 1.1 (unpublished). 2013.

[38] Völkel, K., Schmelzer, M., Wittstock, V. 'Analytical and Numerical Investigation of the Sound Power Emission of a Vibrating Baffled Piston Into a Hemi-Anechoic Room'. In: *Proceedings of DAGA 2014*. CDROM. 2014.

[39] Völkel, K., Wittstock, V. 'Influence of Directvity and Spectral Shape on the Measured Sound Power Level'. In: *Proceedings of InterNoise*. Hamburg, Germany, 2016.

[40] Wittstock, V. 'Uncertainty determination of sound emission measures by round robins'. In: *Proceedings of InterNoise 2010*. CDROM. June 2010.

[41] Wittstock, V. 'A new approach in sound power metrology'. In: *OIML Bulletin* LV.2/3 (2014). Ed. by Organisation Internationale de Metrologie Legale, pp. 9–13.

[42] Wittstock, V., Guglielmone, C. 'Introducing the concept of traceability into sound power measurements'. In: *Proceedings of InterNoise*. Hamburg, Germany, 2016.

[43] Wittstock, V., Schmelzer, M., Bethke, C. 'Establishing traceability for the quantity sound power'. In: *Proceedings of InterNoise 2013*. CDROM. Sept. 2013.

[44] Wöhle, W. *Technische Akustik 1. Lehrbrief*. Zentralstelle für Lehr- und Organisationsmittel des Ministeriums für Hoch- und Fachschulwesen, Zwickau, Germany, 1987, p. 69.

[45] World Health Organization Regional Office for Europe. 'Burden of disease from environmental noise. Quantification of healthy life years lost in Europe'. Report. 2011. URL: `http://www.euro.who.int/__data/assets/pdf_file/0008/136466/e94888.pdf` (visited on 06/2018).

[46] World Meteorological Organization Commission for Instruments and Methods of Observation. *Metrological Traceability for Meteorology*. URL: https://www.wmo.int/pages/prog/www/IMOP/publications/Flyers/Traceability_flyer.pdf (visited on 06/2018).

A | Calculation of Eigenmode Frequencies

In order to determine the Eigenmode frequencies, f_E, for a specific piston, the variable κ_E has to be calculated. Detailed derivations of all equations used in this section can be found in the literature (for example [37]). In fact, the variable κ_E has to be determined numerically and represents values for which the determinant of a defined homogeneous system of equations vanishes (Eq. A.0.1 with functions A.0.2 and A.0.3). Data shown here were obtained for a piston made of PMMA, which corresponds to the piston of Source 1 (Fig. 3.3.1a). Poisson's ratio of $\nu = 0.34$ was used (analogous to [37]) and the first ten values of κ_E^2 calculated. These values correspond to the first ten Eigenmodes, whose Eigenmode frequencies for two exemplary piston radii of $r = 0.03$ m and $r = 0.05$ m were determined as well (Eq. A.0.4 and Tbl. A.0.1).

The relevant variables are:

- κ_E - solution to Eq. A.0.1, corresponding to Eigenmodes
- J_γ - Bessel function of the first kind of order γ
- ν - Poisson's ratio
- B - bending stiffness of the piston material used
- ρ_P - density of piston material
- d_P - thickness of piston (complete height, not half height)
- r - radius of the piston
- $\hat{w}_E$ - amplitude constant of Eigenmode oscillation
- x_r - variable describing the radial distance from the piston centre ($x_r \leq r$)
- β - polar angle
- f_E - Eigenfrequency
- E - Eigenmode number

$$0 = g_1(\kappa)g_2(i\kappa) - g_1(i\kappa)g_2(\kappa) \tag{A.0.1}$$

$$g_1(\kappa) = \frac{1}{2}\kappa^2 \left[J_0(\kappa) - J_2(\kappa)\right] + \nu\kappa J_1(\kappa) \tag{A.0.2}$$

$$g_2(\kappa) = \frac{1}{4}\kappa^3 \left[3J_1(\kappa) - J_3(\kappa)\right] - \frac{1}{2}\kappa^2 \left[J_0(\kappa) - J_2(\kappa)\right] + \kappa J_1(\kappa) \tag{A.0.3}$$

$$f_E = \frac{{\kappa_E}^2}{2\pi r^2}\sqrt{\frac{B}{\rho_\mathrm{P} d_\mathrm{P}}} \tag{A.0.4}$$

Table A.0.1: Values of κ_E^2 for the first ten Eigenmodes. For a PMMA pistons of $r_1 = 3$ cm and $r_2 = 5$ cm radius selected corresponding Eigenmode frequencies, f_E, are shown ($\rho_\mathrm{P} = 1.182{\cdot}10^3$ kg/m^3, $d_\mathrm{P} = 0.012$ m, $\nu = 0.34$, $B = 814$ Nm - from [37]).

E	${\kappa_E}^2$	$f_{E,1}$ **for** $r_1 =$ **0.03 m (Hz)**	$f_{E,2}$ **for** $r_2 =$ **0.05 m (Hz)**
1	9.0905	12 200	4380
2	38.528	51 600	18 600
3	87.833	118 000	42 400
4	156.90		75 700
5	245.72		119 000
6	354.27		
7	482.57		
8	630.61		
9	798.39		
10	985.91		

Similar to the Eigenmode frequencies, the corresponding oscillations can be described mathematically (Eq. A.0.5) [37]. If real measurements were to be matched, the amplitude constant $\hat{w}_E$ would have to be determined from initial value conditions.

$$w_E(x_r, \beta, t) = \hat{w}_E \left[g_1(i\kappa_E) J_0\left(\kappa_E \frac{x_r}{r}\right) - g_1(\kappa_E) J_0\left(i\kappa_E \frac{x_r}{r}\right)\right] e^{i2\pi f_E t} \tag{A.0.5}$$

B | Simplifying Assumption on Surface Area Covered by Measurement Points

Unless noted otherwise, in the calculation of sound power levels from the discretised Rayleigh integral, the assumption was made that each measurement point covered the same amount of surface area (Eq. B.0.1). Considering that in all measurements uniformly distributed grids were used, this seemed an apparent assumption to reduce computation time.

$$S_i = S_j \qquad \forall i, j \tag{B.0.1}$$

To validate the claim, two sound power calculations with data from a 509 point measurement grid (Fig. B.0.1a) were performed. The first assigned the same amount of surface area to each point. The second calculated the exact amount of area for each measurement point as the square of the distance to the closest neighbour of each point. Finally, the total area for both cases was adjusted to a common value.

Comparing the obtained sound power levels shows that the difference is negligible (Fig. B.0.1b). As the chosen 509 point grid did not possess any case specific traits, the result was generalised to all measurements relevant to this work. It should be noted that this equal area assumption (Eq. B.0.1) fails to hold, if measurement grids with non-uniformly distributed points are to be used.

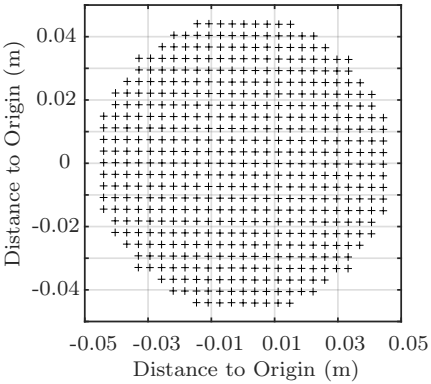

(a) Example of a 509 point measurement grid showing the uniform distribution of sampling points.

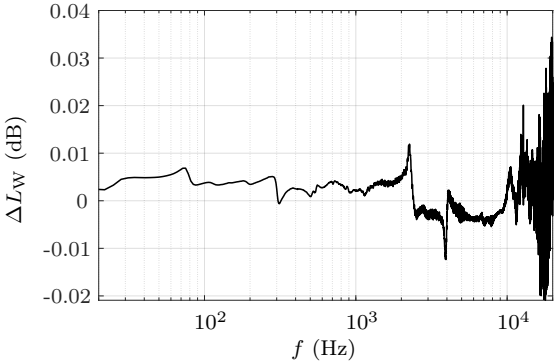

(b) Resulting difference in sound power level. Reference value given by the one obtained using exact areas for each data point.

Figure B.0.1: Comparison of calculated sound power levels based on an exemplary 509 point measurement set evaluating the assignment of exact vs. equal area to each data point.

C | Number of Measurement Points on the Baffle versus Piston Surface

In measurements, excitation of the baffle surface surrounding the piston was observed (see Chp. 6 for examples). The question of interest thus was, how much of the baffle area should be measured. Not measuring any points on the baffle would underestimate the emitted sound power, while measuring too many points on the baffle would introduce significant amounts of noise and could overestimate the emitted sound power. Throughout this discussion, it was assumed that the sampling procedure used the same point density on the piston and baffle surface.

Firstly, calculations were performed analytically. The underlying assumption was that all points on the piston surface moved at some velocity v_{piston} and all points on the baffle moved at some velocity v_{baffle}. Their relation was assumed to be given by $v_{\text{baffle}} = v_{\text{piston}} - X$, for some $X \geq 0$ [m/s].

Furthermore, it was assumed that the observer is positioned in the far field of the source such that the sound pressure, p, is proportional to the square of the velocity, v^2, and the phase difference between all points not significant. The total number of measurement points was then denoted as M and the number of measurement points on the piston as M_{p}. The ratio of these two values was given by $x = M/M_{\text{p}}$ and the corresponding difference in sound power level calculated (Eq. C.0.1).

$$\begin{aligned} \Delta L_{\text{W}} &= 10 \log_{10} \left(\frac{P_{\text{total}}}{P_{\text{piston}}} \right) \\ &= 10 \log_{10}(1 + (x-1)^2 X^2 + 4X(x-1)) \quad [\text{dB}] \end{aligned} \tag{C.0.1}$$

The results show that the number of measured points on the baffle should not be significantly larger than the number of points on the piston (Fig. C.0.1). This is, of course, especially true if the difference in sound velocity levels between piston and baffle are small.

This analytical calculation was a gross oversimplification of the actual measurement observations. For instance, attenuation of velocity levels with

increasing distance from the piston was not considered. This is evidently a major factor. Hence, a similar analysis was carried out using actual measurement data from the 509 and 1425 point data sets. To do so, the parameter kr was used. The values chosen were kr equalling 0.1, 1 and 9. The measurement data on the piston surface were left unchanged. The motion of the baffle was simulated by averaging the velocity levels on the piston surface and subtracting a signal to noise difference between 5 dB and 45 dB. This value was prescribed as maximum velocity level, $\Delta L_{v,\max}$, on the baffle. For each data point, a value was drawn from a uniform distribution with the maximal value defined by $\Delta L_{v,\max}$. For each kr, 10^4 runs were performed as part of a Monte-Carlo simulation.

The results show that, for small kr, noise on the baffle should be avoided (Fig. C.0.2). For $kr = 9$, even small signal to noise ratios provide acceptable results. Small kr and small signal to noise ratios yield significant differences in resulting sound power levels, though. This is especially true for grids where the number of points on the baffle exceeds the number of points on the piston significantly. This was the case for 1425 point grids used in this work. The large efforts needed in data cleansing for the analyses of measurements using these 1425 point grids (Chp. 6) confirm the results of this section.

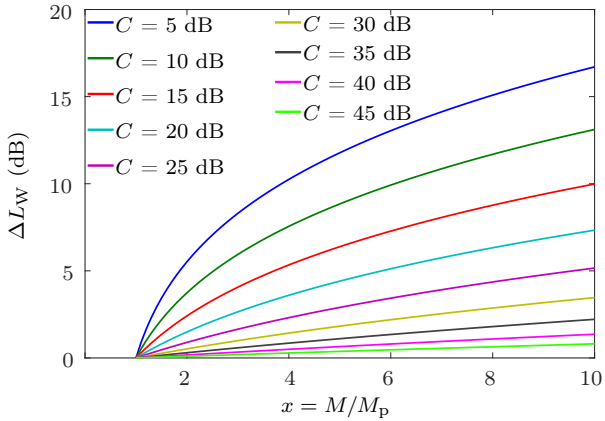

Figure C.0.1: Analytical calculation of difference in sound power level due to noise on the baffle. C denotes the difference in velocity levels between piston and baffle in [dB] as calculated from X.

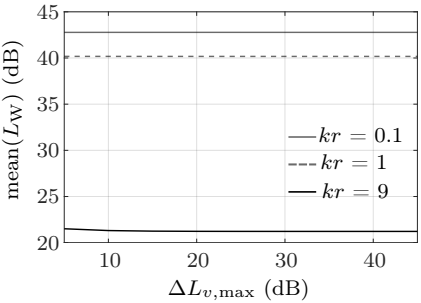

(a) Mean sound power level for 509 point grid.

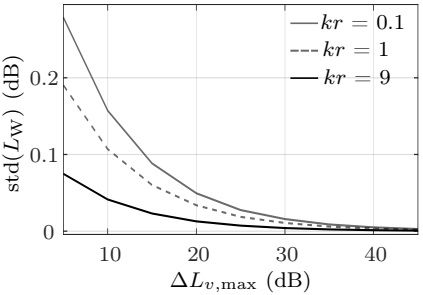

(b) Standard deviation for 509 point grid.

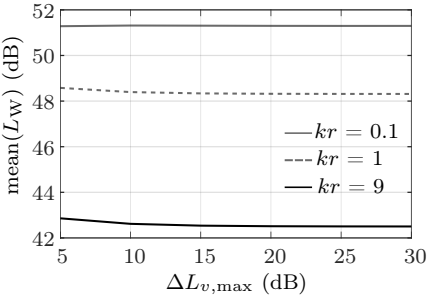

(c) Mean sound power level for 1425 point grid.

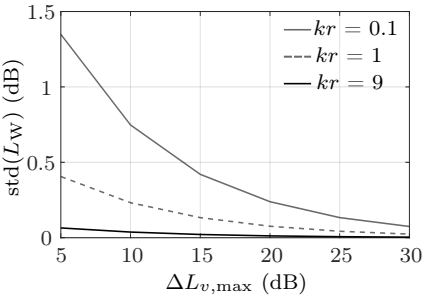

(d) Standard deviation for 1425 point grid.

Figure C.0.2: Monte Carlo simulation results considering effects of sound transmission to the baffle.